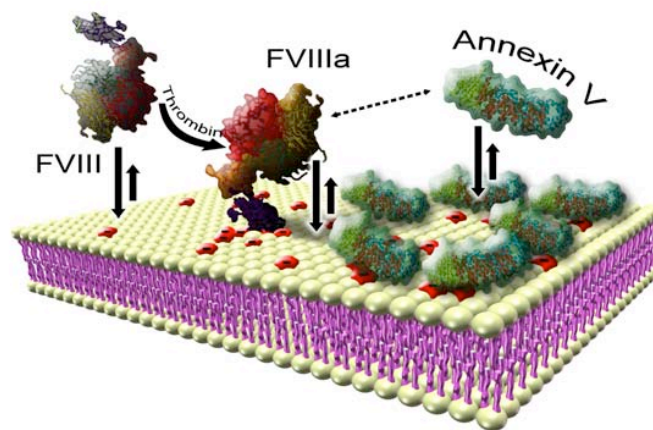

Coagulation protein FVIII binding to phospholipid membranes investigated by Fluorescence Correlation Spectroscopy

Hanna C. Engelke



München 2010

Coagulation protein FVIII binding to phospholipid membranes investigated by Fluorescence Correlation Spectroscopy



Dissertation
an der Fakultät für Physik der
Ludwig-Maximilians-Universität München

vorgelegt von
Hanna C. Engelke
aus Würzburg

Erstgutachter: Prof. Dr. Joachim Rädler
Zweitgutachter: Prof. Dr. Roland Netz
Tag der mündlichen Prüfung: 11. März 2010

Contents

1	Summary	1
2	Zusammenfassung	3
3	Introduction	5
4	Fluorescence Correlation Spectroscopy	9
4.1	Principle	9
4.2	Binding experiments	11
4.3	Quantitative analysis of absolute values	12
4.4	Cross-correlation	14
4.5	Instrumentation	15
5	Analysis of binding isotherms	17
5.1	Equilibrium binding constants	17
5.2	Association and dissociation rates	22
5.3	Mechanisms of and influences on protein-membrane binding	23
6	Diffusion measurements in crowded, scattering media	25
6.1	Complex media	25
6.2	Scattering effects	27
6.3	Hydrodynamic slowdown	29
6.4	Consequences for applications	30
6.4.1	Calibration	30
6.4.2	Binding experiments	31
6.4.3	Blood plasma	32
6.4.4	Cell experiments	33
7	Membrane-binding of Factor VIII within blood coagulation	35
7.1	FVIII binding to membranes	35
7.1.1	Hemostasis	35
7.1.2	Structure, activation and catabolism of FVIII	35
7.1.3	Labeling of FVIII via antibodies	37
7.1.4	FVIII interaction with phospholipid membranes	39
7.2	Activated FVIII interaction with phospholipid membranes	41

7.3	Regulation of activated FVIII binding to phospholipid membranes by annexin V	43
7.3.1	Annexin V binding to phospholipid membranes	43
7.3.2	Annexin V regulates FVIII binding to phospholipid membranes	46
7.4	Experiments in blood plasma	50
8	Binding of coagulation proteins to PEGylated vesicles	53
8.1	PEGylated vesicles as drug delivery systems	53
8.2	Equilibrium binding constants	54
8.3	Effect of PEGylation regime on binding	55
8.4	Binding kinetics	55
9	Lipid-coated mesoporous nanoparticles as drug delivery system	57
9.1	Nanoparticles as drug delivery systems	57
9.2	Lipid-coating of the nanoparticles	58
9.3	Characterization of the lipid coated nanoparticles	59
9.4	In-vitro release experiments	62
9.5	In-vivo delivery and release experiments	62
9.6	Future investigations and further applications of the lipid-coated nanoparticles	66
10	Probing the viscosity in Dictyostelium discoideum cells	69
10.1	Probing the viscosity in living cells with Fluorescence Correlation Spectroscopy	69
10.2	Viscosity in the cytoplasm of dictyostelium cells	71
10.3	Viscosity in the actin cortex of dictyostelium cells	73
10.4	Influence of jasplakinolide	73
10.5	Latrunculin induced actin waves	74
11	Two-photon Fluorescence Correlation Spectroscopy	77
11.1	Comparison of conventional one-photon- and two-photon microscopy	77
11.2	Setup of the two-photon microscope	78
11.3	First results of auto- and cross-correlation experiments	79
12	Electrostatically coupled diffusion of short ds-oligonucleotides on cationic lipid membranes	83
12.1	Fluorescence Correlation Spectroscopy in two dimensions	83
12.2	DNA diffusion on supported lipid bilayers	85
12.3	Cross-correlation-experiments on DNA diffusion on supported lipid membranes	87
12.4	Electrophoresis	88
13	Outlook	91

14 Danksagung	104
15 Lebenslauf	107

1 Summary

Fluorescence Correlation Spectroscopy (FCS) allows one to measure protein-membrane binding, self-assembly and other molecular reactions and parameters quantitatively in buffer as well as in complex media. Subject of this thesis was to investigate protein-membrane interactions within blood coagulation in buffer as well as in their biological environment with FCS.

Binding of Factor VIII (FVIII) to phosphatidylserine (PS)-expressing platelets is a key process in the intravascular pathway of the blood coagulation cascade. Representing a complex component of the highly regulated network of the coagulation cascade, this protein-membrane interaction is influenced by many cofactors, such as annexin, which binds to PS-containing membranes as well. Since defects in coagulation, particularly in FVIII binding to membranes lead to severe bleeding disorders, a better understanding of the underlying biophysical and biochemical mechanisms and regulatory influences of this interaction could boost diagnosis and therapy of such diseases, especially when used in combination with an improved systems biology description of the cascade.

This thesis investigates the mechanism of FVIII binding to PS-containing model membranes and its regulation by annexin using FCS. Activated FVIII, in contrast to inactivated FVIII, was found to exhibit a striking binding anomaly, consisting in a sharply peaked dependence of the binding constant $K(\text{PS})$ as a function of the PS content. It exceeds the binding of inactivated FVIII in a regime around 12% PS, including physiological concentrations. Furthermore, the regulatory influence of annexin, which can both, increase as well as decrease the binding of activated FVIII, was explained based on this binding anomaly. A quantitative model of this regulatory mechanism assuming efficient shielding of charges by annexin was developed, which allows for the reconstruction of the full three-dimensional phase diagram of FVIII binding to membranes as a function of their PS-content and the concentration of annexin. In order to prove the relevance of these results for coagulation, the experiments were repeated in plasma.

Since plasma is a scattering medium, which is crowded by macromolecules and hence strongly affects FCS experiments, a procedure to analyze measurements performed in such complex media was developed. To this end, the influences of scattering and crowding on FCS were investigated using a model system of GFP in highly concentrated vesicle solutions. Scattering was found to enhance and distort the focal volume, whereas crowding slows down diffusion. Taking both effects into account, corrections could be applied, which were demonstrated to allow for artifact-free analysis of binding measurements in complex soft matter systems. To further improve the performance of FCS in complex media and, particularly, in cells, a two-photon FCS microscope was set up.

Based on the results of the investigations on scattering and crowding, FCS experiments on living cells were performed. The effective viscosity in *dictyostelium discoideum* cells was probed and compared to values obtained in lysate. The enhancement of viscosity in the cytoplasm was found to be due to crowding by polydisperse macromolecules, whereas the viscosity of the actin cortex was determined by actin polymerization. Drug treatment allowed for regulation of the polymerization level in the cytoplasm and for detection and determination of the viscosity of actin waves.

A project in close collaboration with the groups of Prof. Bein and Prof. Bräuchle succeeded in the design, characterization and testing of a drug delivery system employing colloidal mesoporous silica nanoparticles efficiently coated by lipids with a solvent exchange method. Using cross-correlation spectroscopy the lipids were shown to form a close and dense bilayer around the nanoparticles. In-vitro drug delivery experiments gave evidence of the capping-mechanism of the lipids and in-vivo studies proved the efficient delivery and release of drugs by the lipid-coated nanoparticles.

2 Zusammenfassung

Mit Fluoreszenz-Korrelations-Spektroskopie (FCS) können Protein-Membran-Bindungen und andere molekulare Reaktionen und Parameter quantitativ auch in komplexen Medien gemessen werden. Inhalt dieser Arbeit war die Untersuchung von Protein-Membran-Wechselwirkungen bei der Blutgerinnung in Puffer wie auch in biologischer Umgebung mit Hilfe von FCS.

Die Bindung von Faktor VIII (FVIII) an Blutplättchen, die Phosphatidylserin (PS) exprimieren, ist ein wichtiger Bestandteil des intravaskulären Systems der Blutgerinnungskaskade. Diese Protein-Membran-Wechselwirkung ist eine komplexe Komponente des hochregulierten Netzwerks der Blutgerinnungskaskade und ist von vielen Kofaktoren beeinflusst, wie zum Beispiel von Annexin, das wie FVIII auch an PS-haltige Membranen bindet. Da Störungen der Gerinnung, insbesondere der FVIII-Bindung an Membranen zu schweren Blutungskrankheiten führen, könnte ein besseres Verständnis der zugrundeliegenden biophysikalischen und biochemischen Mechanismen und regulatorischen Einflüsse dieser Wechselwirkung die Diagnose und Therapie solcher Krankheiten wesentlich verbessern, besonders in Kombination mit einer dadurch verbesserten system-biologischen Beschreibung der Gerinnungskaskade.

Diese Arbeit untersucht mit Hilfe von FCS den Mechanismus der FVIII-Bindung an PS-haltige Modellmembranen und ihre Regulation durch Annexin. Im Gegensatz zu inaktiviertem FVIII, zeigt aktivierter FVIII eine starke Bindungsanomalie, die sich in einem scharfen Maximum der PS-Abhängigkeit der Bindungskonstante äussert. Die Bindungsstärke übersteigt die von inaktiviertem FVIII in einem Bereich um 12% PS-Gehalt, der auch die physiologischen Konzentrationen beinhaltet. Darüberhinaus wurde der regulatorische Einfluss von Annexin, das die Bindung von aktiviertem FVIII sowohl erhöhen als auch vermindern kann, mit dieser Bindungsanomalie erklärt. Es wurde ein quantitatives Modell dieses Regulationsmechanismus entwickelt, das davon ausgeht, dass Annexin die PS-Ladungen effizient abschirmt. Dieses Modell ermöglichte die Rekonstruktion des vollen dreidimensionalen Phasendiagramms der FVIII-Bindung an Membranen als Funktion ihres PS-Gehalts und der Annexinkonzentration. Um die Relevanz der Ergebnisse für die Blutgerinnung zu demonstrieren, wurden die Experimente in Plasma wiederholt.

Da Plasma eine stark streuende Substanz und angefüllt mit Makromolekülen ist, beeinflusst es FCS-Experimente stark. Deswegen wurde im Rahmen dieser Arbeit eine Technik entwickelt, die FCS-Messungen in solch komplexen Substanzen erlaubt. Dazu wurden die Einflüsse von Streuung und von hohen Makromolekülkonzentrationen auf FCS anhand eines Modellsystems bestehend aus GFP in hochkonzentrierten Vesikellö-

sungen untersucht. Es wurde gezeigt, dass Streuung den Fokus vergrößert und verzerrt, während hohe Makromolekülkonzentrationen die Diffusion verlangsamen. Unter Berücksichtigung beider Effekte konnten Korrekturen erarbeitet werden, die artefaktfreie Analyse von Bindungsmessungen in komplexen Lösungen erlauben. Um FCS-Messungen in solchen Medien und insbesondere in Zellen weiter zu verbessern, wurde zudem ein Zwei-Photonen FCS-Mikroskop aufgebaut.

Auf dem Hintergrund dieser Ergebnisse wurden FCS-Experimente an lebenden Zellen durchgeführt. Die effektive Viskosität in *Dictyostelium discoideum* Zellen wurde gemessen und mit Werten aus deren Lysat verglichen. Die Erhöhung der Viskosität im Zytoplasma konnte den hohen Konzentrationen an polydispersen Makromolekülen zugeschrieben werden, während die Viskosität im Aktinkortex vom polymerisierten Aktinnetzwerk bestimmt wird. Durch Zugabe von polymerisationsregulierenden Substanzen wurde der Polymerisationsgrad im Zytoplasma erhöht. Zudem wurden dadurch Aktinwellen erzeugt, detektiert und ihre Viskosität gemessen.

Ein Projekt in enger Zusammenarbeit mit den Gruppen von Prof. Bein und Prof. Bräuchle konnte ein Wirkstoffträgersystem erfolgreich entwickeln, charakterisieren und testen. Dabei werden mesoporöse Nanopartikel als Träger benutzt, die durch Lösungsmittelaustausch mit Lipiden ummantelt werden. Dabei wurde mit FCS und Spektrometern gemessen, dass die Lipide eine dichte Hülle um die Nanopartikel bilden. In-vivo-Studien konnten schließlich die effektive Funktionalität der lipidummantelten Nanopartikel beweisen.

3 Introduction

Protein-membrane interactions are of pivotal importance to biology. Since cells are encapsulated by membranes, all forms of communication of the cell with its environment have to pass the membrane. Sensing and signalling processes often involve protein-membrane interactions. Many signalling pathways for instance are triggered by binding of certain proteins to the cellular membrane. Such protein-membrane interactions transfer external signals to the interior of cells and initiate responses such as the activation of regulatory networks leading to the expression of certain genes or other cellular processes. A prominent example is the initiation of mitosis by EGF binding to EGF-receptors of the cellular membrane [1]. Next to the sensing of external signals, the cell uses the membrane to send signals to its environment, such as by expression of phosphatidylserine upon apoptosis, which leads to binding of the protein annexin [2]. An other key function of protein-membrane interactions in nature is the local confinement of processes, which involve proteins. Blood coagulation for instance is confined to the region of the injury, where the membranes express phosphatidylserine. Phosphatidylserine mediates binding of FVIII and other coagulation proteins to the membranes and hence, it is on the surface of the platelet membrane, that activated FVIII (FVIIIa) subsequently forms the tenase complex with FIXa, which induces further downstream events leading to coagulation [3]. Here, the crucial role of protein-membrane binding is to concentrate the tenase complexes, limit the interactions to two dimensions and to provide optimal mutual orientation of the tenase components. Severe diseases, such as cancer or bleeding disorders in the case of coagulation, are caused by dysfunctions of certain protein-membrane interactions. Considering these consequences of possible malfunctions and the importance of protein-membrane interactions for life, it is very desirable to understand the underlying biophysical and biological mechanisms.

A quantitative understanding of protein-membrane interactions is of importance to systemic modeling of processes involving such interactions. Systems biology aims to describe and simulate complex biological networks. A description by means of systems biology of e.g. the coagulation cascade or other biological processes of similar importance and complexity has the potential to boost medical and pharmaceutical research and hence could drastically improve diagnostics and therapy of many diseases. Yet, the complexity of biochemical networks represents a formidable challenge. Prerequisite for reliable modeling is the knowledge of all binding constants, reaction rates and possibly their dependence on various system states. To this end, lipid membrane related reactions impose an even more complex description. In particular, membrane binding can be strongly cooperative and be affected by the local as well as global composition of the

membrane. The binding of EGF to membranes e.g. comes along with sequestering of the charges of the PIP moiety in the membrane [4,5]. Hence, the lipid membrane composition plays a regulatory role, which is not fully captured in the present day simulation tools.

This work focusses on protein-membrane interactions within the coagulation cascade, particularly, the binding of FVIII to membranes. Investigations on PS-vesicles as model systems for platelets showed that binding of inactivated FVIII to membranes is strongly associated with electrostatic interactions and therefore increases with the concentration of charge (i.e. phosphatidylserine) in the membrane [6]. For activated FVIII however, binding and particularly, its dependence on the PS-content, has not yet been investigated. Likewise, there is not yet quantitative support for regulatory processes such as the scenario of competitive binding of FVIII and annexin as depicted in the coverfigure.

Fluorescence Correlation Spectroscopy is a powerful tool for the investigation of protein-membrane interactions. It measures diffusion times and can discriminate freely diffusing proteins from proteins bound to vesicles as model membranes based on the size-dependence of the diffusion time [7, 8]. Hence, binding isotherms can be obtained from consecutive titration experiments. Compared to other conventional techniques used for binding experiments, such as ELISA, which all rely on one component bound to a surface, an advantage of Fluorescence Correlation Spectroscopy is that it allows for measurements in solution. However, if desired, experiments can be performed on supported lipid bilayers as described in chapter 12. In this thesis protein-membrane binding within coagulation was investigated with FCS using both, experiments in solution as well as on supported membranes.

To elucidate the protein-membrane interaction of FVIII and FVIIIa as well as the mechanism behind the influence of annexin on FVIIIa binding to membranes, the binding characteristics of FVIII and FVIIIa are studied with Fluorescence Correlation Spectroscopy as a function of the PS-content of the membrane. Furthermore, the regulatory role of annexin V on FVIIIa binding is investigated and is found to be based on the strong PS-dependence of FVIII. The results of these studies are presented in chapter 7. All of these experiments are performed in dilute buffer solutions, where Fluorescence Correlation Spectroscopy is a well established technique. Since the natural environment of coagulation processes is blood, it is desirable to measure in a more physiological solution compared to buffer. Blood and other biological fluids however, represent complex media, which are scattering and crowded and hence strongly influence Fluorescence Correlation Spectroscopy experiments. To overcome this challenge, a technique to measure in complex soft matter systems was developed, which is described in chapter 6 and allows for measurements of FVIIIa binding to membranes in plasma. Furthermore, it provides a basis to measure in living cells and emphasizes the importance of viscosity measurements. With this in the background the viscosity in living *dictyostelium discoideum* cells is probed using Fluorescence Correlation Spectroscopy, as described in chapter 10. To further improve the performance of in-vivo experiments by a reduction of scattering, a two-photon microscope was set up (chapter 11).

All investigations layed out above are related to membranes and their biological func-

tion. However, membranes are also of great importance to biotechnology, e.g. as drug delivery systems. A project of this thesis, presented in chapter 9, was the design, characterization and test of a drug delivery system consisting of membrane-coated colloidal mesoporous silica nanoparticles. Since liposomal drug delivery often employs PEGylated vesicles, chapter 8 studies the influence of PEGylation on protein binding to liposomes.

4 Fluorescence Correlation Spectroscopy

4.1 Principle

Fluorescence correlation spectroscopy (FCS) measures the intensity time trace of fluorescent particles in the optical focus and gains information out of the intensity fluctuations. Measurements are usually performed with a confocal setup where two pinholes are used to guarantee for a very small, well defined focus of about 0.2 fl. Combined with a sample concentration in the nanomolar regime this enables one to have on average only a few particles in the focus and hence it allows for a sensitive detection of small intensity fluctuations [9]. To extract information on the fluorescent particles out of the intensity fluctuations, FCS employs the autocorrelation of the intensity traces with respect to time (Fig. 4.1). The normalized autocorrelation function $G(\tau)$ is defined as:

$$G(\tau) = \frac{\langle I(t) \cdot I(t + \tau) \rangle}{\langle I(t) \rangle^2} \quad (4.1)$$

where averaging of the intensities is usually done over 30-600 s depending on the sample. The experimental autocorrelation function $G(\tau)$ incorporates intensity fluctuations from various sources, which include among others photophysical effects as well as rotation or diffusion dynamics with each appearing at a characteristic timescale [9, 10]. For the timescales and systems, which are investigated in this thesis, the autocorrelation functions are composed of a photophysical contribution due to triplet kinetics and a contribution from the diffusion dynamics of the fluorescent particles:

$$G(\tau) = 1 + G_{trip} \cdot G_{diff} \quad (4.2)$$

The triplet contribution reveals the photophysical characteristics of the fluorescent dye and its interaction with the surrounding solution. It is usually described by an exponential decay [10]:

$$G_{trip}(\tau) = \left(1 + \frac{f_{trip}}{1 - f_{trip}}\right) e^{-\frac{\tau}{\tau_{trip}}} \quad (4.3)$$

with the triplet decay time τ_{trip} and the fraction of molecules in the triplet state f_{trip} . Triplet kinetics was not subject of this work and G_{trip} was only included into the fitting

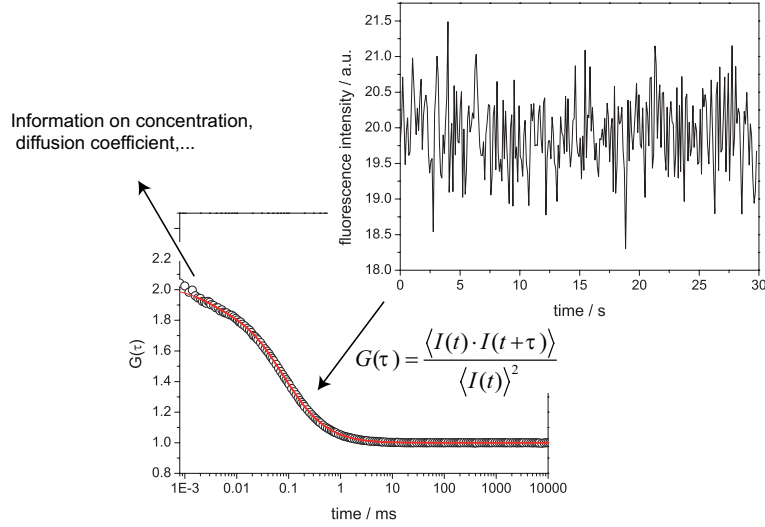


Figure 4.1: *Principle of Fluorescence Correlation Spectroscopy: Information on fluorescent particles is extracted from their intensity time trace via the autocorrelation function*

procedure to obtain reliable results for G_{diff} . For simplicity G_{trip} is therefore neglected in the following explanations.

The contribution to the autocorrelation originating from intensity fluctuations due to Brownian diffusion of the fluorescent particles can be analytically derived assuming a Gaussian-shaped focus of waist ω_x in-plane and ω_z along the focal axis. In the case of particles showing three-dimensional Brownian diffusion in a solution, this yields [9]:

$$G_{diff} = \frac{1}{N} \cdot \frac{1}{1 + \frac{\tau}{\tau_D}} \cdot \frac{1}{\sqrt{1 + \frac{\tau}{S^2 \cdot \tau_D}}} \quad (4.4)$$

where N denotes the average number of particles in the focus and S the structure parameter, which is the ratio between the focus radius in z- and in x-y direction, being defined by $S = \omega_z/\omega_x$. The diffusion time τ_D provides a measure for the average time required by a particle to cross the focal width and is given by:

$$\tau_D = \frac{\omega_x^2}{4D} \quad (4.5)$$

with D being the diffusion coefficient of the fluorescent particles. The average number of particles in the focus, N , is related to the concentration, c , of the particles in the sample solution via the confocal Volume V :

$$N = c \cdot V \quad (4.6)$$

The structure parameter depends only on the optical properties of the setup and the sample solution. Therefore, most frequently it is determined from a measurement of a

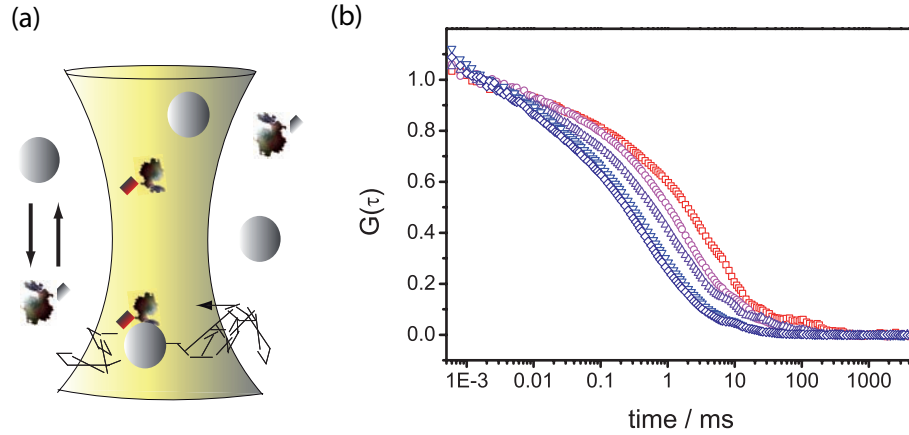


Figure 4.2: Illustration of binding experiments with FCS on the example of activated FVIII binding to PS-vesicles. (a) Focus with fluorescently labeled, fast diffusing, small proteins, which are slowed down when bound to the large unlabeled vesicles. (b) Autocorrelation functions of activated FVIII binding to PS-vesicles. From blue to red they are shifted towards longer times due to an increased lipid concentration leading to an increased amount of bound proteins.

well known sample and then kept as a fix parameter unless the optical properties of the sample solution are changed, e.g. by a change of buffer. Equation 4.4 can then be used to analyze FCS experiments with the particle number N and the diffusion time τ_D as free fit parameters. This allows for a very accurate determination of the relative size of the concentration, the diffusion coefficient [11] and related parameters such as viscosity, η , and hydrodynamic radius [12], R , which can be deduced from the diffusion coefficient employing the Stokes-Einstein relation:

$$D = \frac{kT}{6\pi\eta R} \quad (4.7)$$

To obtain absolute values, the confocal volume V has to be known. Measurement of absolute quantities and determination of the confocal volume V will be described in chapter 4.3. In this thesis the high accuracy of relative measurements was employed to study for instance the effective viscosity within *dictyostelium discoideum* cells compared to the viscosity in cell lysate upon drug treatment and in different parts of the cell.

4.2 Binding experiments

Another important application of the ability of FCS to measure relative diffusion coefficients and their changes with high accuracy is the performance of binding experiments [7, 13–15]. The analysis of such binding experiments with FCS is based on the fact that diffusion of particles depends on their size as described by equation 4.7. Fig.

4.2(a) shows small fluorescent particles in the focal volume, which are diffusing freely in solution and consequently exhibit an autocorrelation function with a fairly short diffusion time. As soon as they bind to larger particles, their diffusion will be slowed down leading to an increase of the diffusion time. The autocorrelation of a solution of bound and unbound molecules consists of contributions from both, each weighted by their relative concentration in the solution. Hence, the decay of the autocorrelation of such a solution is shifted towards longer times with increasing fraction of bound molecules. An example for this change of the autocorrelation upon binding is displayed in Fig. 4.2(b), which results from an increasing amount of labeled Factor VIIIa binding to unlabeled vesicles.

In a system composed of multiple distinct species, the autocorrelation function can be generalized:

$$G(\tau) = \frac{\sum q_i^2 N_i g_i(\tau)}{(\sum q_i N_i)^2} = N \frac{\sum q_i^2 f_i g_i(\tau)}{(\sum q_i N_i)^2} \quad (4.8)$$

with the mean particle number N_i and the brightness q_i of component i . f_i is the fraction of component i and g_i represents its time-dependent autocorrelation function. This form of the autocorrelation function allows for the analysis and discrimination of species of different diffusion characteristics and can be applied to quantitatively determine the binding of small fluorescent particles to particles of larger size as described above qualitatively. Evaluation of the relative fraction of bound and unbound particles resulting from a two-component fit to the autocorrelation functions obtained in a titration experiment yields the binding isotherm [7]. In the case of equal brightness of bound and unbound particles, equation 4.8 can be written as:

$$G(\tau) = 1 + \frac{1}{N} \sum f_i g_i(\tau) \quad (4.9)$$

with the particle number N . When particles are used, which change brightness upon binding, e.g. due to quenching effects, this has to be considered by corrections to equation 4.9 or analysis with the general equation 4.8 [16]. The fluorescent molecules investigated in this thesis did not show any change in brightness upon binding. Thus, equation 4.9 was used to analyse binding experiments.

To reduce artifacts from the fitting routine, the autocorrelation of each component, g_i , was determined separately and then kept as fixed parameter leaving the number of particles and the fractions of bound and unbound particles as the only free fit parameters.

4.3 Quantitative analysis of absolute values

FCS is a very accurate technique to determine the relative size of concentrations and diffusion coefficients with important applications, such as the evaluation of binding experiments explained above. Additionally, it provides a means to determine the absolute

values of concentration and diffusion coefficient. The parameters τ_D and N depend on the optical volume. From these, the characteristic parameters of the measured sample, namely the diffusion coefficient and the concentration, which are independent of the optical setup, can be derived with equation 4.5 and 4.6. To this end, a precise knowledge of the size of the confocal volume and hence an exact calibration is crucial [17].

In order to test the performance of absolute concentration measurements and to find a reliable calibration method, experiments on dye solutions of known concentration were carried out. The concentration of a 26 nM solution of Rhodamine 6G was verified photometrically. The relative concentrations of a titration experiment were successfully measured with FCS. To extract absolute values, the common calibration procedure is to determine the size of the confocal volume via equation 4.5 using the diffusion time from a fit to an autocorrelation function of a reference experiment on Rhodamine solution and the diffusion coefficient for Rhodamine of $280\mu\text{m}^2\text{s}^{-1}$ as reported by Magde et al. [18]. The obtained size of the confocal volume can then be used to calculate the concentration according to equation 4.6. However, this method did not yield the right concentrations. Therefore, as an alternative method, the volume was calculated via equation 4.6 with the known concentration and the particle number revealed by the fit. The calculated volume was then used to determine the diffusion coefficient yielding a value of $408\mu\text{m}^2\text{s}^{-1}$. The same experiment was done using a fluorescein calibration standard at a well defined concentration of 50 nM. Again, the common calibration with the diffusion coefficient of Rhodamine failed to reveal the right concentration. The diffusion coefficient of fluorescein in water deduced from calibration via the known concentration was $430\mu\text{m}^2\text{s}^{-1}$.

The diffusion coefficients obtained with the alternative method employing the known concentrations agree very well with the values of Culbertson et al. [19], who measured diffusion coefficients of $414\mu\text{m}^2\text{s}^{-1}$ for Rhodamine and $425\mu\text{m}^2\text{s}^{-1}$ for fluorescein in water with microfluidic techniques. These values were confirmed recently by novel FCS techniques such as Scanning FCS [20] and double focus FCS [21], which employ intrinsic well-defined length scales, i.e. the scanning speed and the distance of the two foci, respectively, for calibration. From these findings, one can conclude, that the diffusion coefficient reported by Magde et al. [18](with a reported error of 35%) was not accurate enough and hence the commonly used calibration procedure led to wrong results whenever this value was used.

Even with the recently determined values, calibration via the diffusion coefficient bears some reservations and has to be applied with great care. Calibration measurements should always be done under the same conditions as the experiments regarding solvent and temperature to name just the most important factors. A change of buffer for example might change the refractive index of the sample and this can have a strong influence on size and shape of the confocal volume [22, 23]. Chapter 6 deals with the influences of the surrounding medium on the performance of FCS in more detail. The diffusion coefficients found in literature, which could be used as reference for calibration, however, are usually determined in water under standard conditions. Since diffusion

coefficients are strongly dependent on solvent and temperature, they can not be used for calibration in solvents or under conditions different from the reference experiment. This restriction can be circumvented by the calibration method via the concentration. The concentration is a very well-defined parameter, independent of temperature and solvent. It can be determined separately with independent techniques under standard conditions or standard calibration solutions with well known concentrations can be used. The solution can then be diluted in well-defined steps with the buffer used for the experiments and calibration can be performed under the same conditions as the sample measurements. Hence, determination of the size of the confocal volume via the concentration allows for calibration adaptable to a huge variety of non-standard experimental conditions and leads to reliable results as demonstrated by the values for the diffusion coefficients reported above.

One further issue has to be considered for all concentration measurements, no matter whether they are absolute or relative: The background intensity should be negligible compared to the signal of the sample. Otherwise the influence of the background signal has to be taken into account during analysis. In this case, the measured intensity is composed of the sum of background and sample signal:

$$I_{measured} = I_{background} + I_{sample} \quad (4.10)$$

This equation can be used to correct the autocorrelation function for the background signal and simple considerations and algebraic transformations lead to a parabolic dependence of the measured number of particles on the concentration of the sample:

$$N_{measured} = N \left(1 + \frac{I_{sample}}{I_{background}}\right)^2 = c \cdot V \left(1 + \frac{I_{sample}}{I_{background}}\right)^2 \quad (4.11)$$

This dependence is shown in Fig. 4.3 which reveals the number of GFP molecules determined experimentally as a function of the relative GFP concentration of the sample solution. The data exhibit a parabolic shape and can be described consistently by the red line which represents a fit according to equation 4.11. For concentrations which are high enough to produce a signal much brighter than the background, the number of particles increases linear with the concentration and a background correction according to equation 4.11 is not necessary. Experiments at lower concentrations, however, need to be corrected for the background influence to yield reliable results.

4.4 Cross-correlation

The explanations of FCS analysis in the sections above dealt with autocorrelation functions, correlating only one single intensity trace with itself. Another option of FCS analysis is to crosscorrelate two different intensity traces with each other, yielding a cross-correlation function $G_{cross}(\tau)$ as follows [24]:

$$G_{cross}(\tau) = \frac{\langle I_1(t) \cdot I_2(t + \tau) \rangle}{\langle I_1(t) \rangle \langle I_2(t) \rangle} \quad (4.12)$$

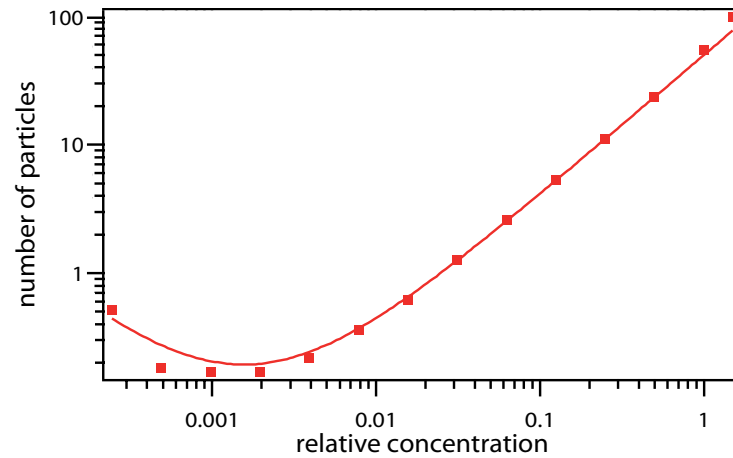


Figure 4.3: Experimentally determined number of GFP molecules in the focus as a function of the relative GFP-concentration in the solution. With decreasing concentration the influence of the background signal increases leading to a parabolic dependence.

where I_1 and I_2 are the measured intensities. Cross-correlation functions of single colour intensity traces obtained from two separate detectors during the same experiment are often used to improve the signal to noise ratio and to eliminate noise from the detector. Another very important application of cross-correlation analysis are dual colour experiments on samples containing two different species each labeled with a fluorescent dye of different colour [25, 26]. If the signals of the two colours are spectrally discriminated and detected at the same time in separate channels the autocorrelation provides information on each single species and is complemented by the cross-correlation of the two channels yielding information on the correlation of the movement of the two species, i.e. whether they are bound and move in a correlated way or whether they move independently. For independent movement of the species the cross-correlation constantly equals one, whereas colocalization of the species and hence correlated movement leads to a distinct cross-correlation function. The amplitudes of the cross-correlation and the autocorrelation functions can then be used to deduce the fraction of colocalized particles ([25, 26]).

4.5 Instrumentation

FCS measurements were performed on an Axiovert 200 microscope with a ConfoCor 2 unit (Carl Zeiss, Jena, Germany). Excitation was usually done with an Argon ion laser at 488 nm, with an average power of $15\mu W$ on the sample. Fluorescence emission was filtered from the excitation light using a 525/25 bandpass filter. The objective used was a 40x (NA = 1.2) water immersion apochromat (Carl Zeiss, Jena, Germany). Samples

were measured in eight well LabTek I chamber slides (nunc, Rochester, NY), except for in-vivo cell measurements, which were carried out on glass cover slides. For cross-correlation experiments with Alexa 647-labeled molecules, a HeNe-laser (633 nm) and a longpass 650 filter were added to the setup and the objective was replaced by a 63x (NA = 1.2) water immersion apochromat (Carl Zeiss, Jena, Germany), which collects less fluorescence light, but has a better correction for chromatic aberration. Correlation and analysis were performed using the ConfoCor 2 software. Fitting procedures employing other functions than equation 4.4 and 4.9 were carried out using Origin.

5 Analysis of binding isotherms

In this chapter the analysis of titration experiments for the investigation of protein-membrane binding is explained. FCS measurements allow for the determination of the fraction of bound protein as a function of the lipid concentration, which can then be used to extract the equilibrium binding constant. Here, the underlying definitions and theory are described for equilibrium constants as well as for association and dissociation rates, which can be accessed by time-resolved FCS experiments. Knowledge of the binding constants and particularly their dependences on certain parameters in its turn allows for the investigation of mechanisms of interaction, which can be very complex in the case of protein-membrane binding. The last section of this chapter explains some of these mechanisms and the complexity which can underlie protein-membrane binding.

5.1 Equilibrium binding constants

The reaction of a simple bimolecular binding process of a single ligand l binding to a single receptor r leading to the formation of the complex lr , is characterized by the stoichiometric equation



This process is determined by the law of mass action. The corresponding molar partition coefficient, also named (association) binding constant, is defined as:

$$K_{lr} = \frac{lr}{l_{free} \cdot r_{free}} \quad (5.2)$$

Binding measurements often reveal the fraction of bound ligands f_{boundl} , i.e. the number of bound ligands l_{bound} relative to the total amount of ligands $l_{tot} = l_{free} + l_{bound}$:

$$f_{boundl} = \frac{l_{bound}}{l_{tot}} = \frac{l_{bound}}{l_{free} + l_{bound}} \quad (5.3)$$

In this simple case of a two-body interaction, the number of bound ligands l_{bound} equals the number of complexes lr and the fraction of bound ligands can be expressed in terms of the binding constant by insertion of equation 5.12 into equation 5.3:

$$f_{boundl} = \frac{l_{bound}}{l_{free} + l_{bound}} = \frac{lr}{l_{free} + lr} = \frac{K \cdot r_{free}}{1 + K \cdot r_{free}} \quad (5.4)$$

This equation can be used to experimentally determine the binding constant of a ligand receptor interaction. A measurement of the fraction of bound ligand as a function of the concentration of free receptors yields the so-called binding isotherm, which is an S-shaped curve, when plotted on a semi-log scale, and can be used to extract the binding constant with a fit according to equation 5.4.

Measurements revealing the fraction of occupied receptors f_{occr} , i.e. the number of occupied receptors r_{occ} relative to the total amount of receptors $r_{tot} = r_{free} + r_{occ}$:

$$f_{occr} = \frac{r_{free}}{r_{tot}} = \frac{r_{occ}}{r_{free} + r_{occ}} \quad (5.5)$$

can be used to determine the binding constant from a titration of the ligand concentration in analogy to the case layed out above with the equation:

$$f_{occr} = \frac{K \cdot l_{free}}{1 + K \cdot l_{free}} \quad (5.6)$$

The considerations above were all done assuming that a single ligand binds to a single receptor. However, there are many biological reactions for which this assumption is inadequate. Often, receptors offer more than one single binding site to ligands. Sometimes, this is accompanied by a switch-like binding behaviour resulting in clear "on"- "off" signals. In this case of all-or-nothing binding either all binding sites n on a receptor are occupied by ligands or none. This can be expressed by the following reaction equation:



The number of occupied receptors $l_n r$ can be written in terms of the binding constant using equation 5.12 iteratively:

$$l_n r = K^n l^n r \quad (5.8)$$

The fraction of receptors occupied due to all-or-nothing binding to their n binding sites can be written as:

$$f_{occr} = \frac{l_n r}{r_{free} + l_n r} \quad (5.9)$$

Using equation 5.8 this can be rewritten as:

$$f_{occr} = \frac{(K \cdot l_{free})^n}{1 + (K \cdot l_{free})^n} \quad (5.10)$$

Due to the cooperative all-or-nothing behaviour, the binding isotherms resulting from this reaction are steeper compared to those of single ligand binding and this steepness allows for clear discrimination of bound and unbound states.

From a statistical point of view the fraction of bound ligands can be interpreted as the probability that a ligand is bound to a receptor. This allows for an easy expansion

of the bimolecular reaction of single ligand binding as described above to the general case of ligands binding to receptors of n binding sites. In contrast to the all-or-nothing binding, here, one up to n ligands can bind to one receptor. Assuming that the binding constant, K , for a ligand to a receptor is independent of the amount of occupied binding sites on that receptor, the probability p_i of a ligand binding to a receptor of n binding sites which is occupied by i ligands is the same for all $i = 0, 1, \dots, n - 1$. The probability p_{boundl} that a ligand is bound to a receptor with n possible binding sites is then given by the sum over the probabilities p_i to bind to a receptor with i occupied binding sites:

$$p_{boundl} = \sum_{i=0}^{n-1} p_i = \sum_{i=0}^{n-1} p = n \cdot p \quad (5.11)$$

Due to the independence of the binding probability on the amount of occupied binding sites, the probability p can be expressed in terms of the bimolecular reaction using equation 5.4. The fraction of bound proteins, i.e. the probability that a ligand is bound to a receptor can thus be written as:

$$f_{boundl} = p_{boundl} = n \cdot p = n \frac{K \cdot r_{free}}{1 + K \cdot r_{free}} \quad (5.12)$$

Using a statistical description of binding processes the theoretical treatment can be generalized to binding involving for instance more than one binding constant and hence it can be adapted to various situations [27]. However, in the following binding constants were always assumed to be equal.

In this thesis, protein-membrane binding was investigated with a membrane realized by large unilamellar vesicles of 100 nm diameter. They act as receptor which can be occupied by up to n proteins, i.e. ligands. Hence, the fraction of bound proteins f_{bound} can be expressed in terms of free vesicles V_{free} using equation 5.12:

$$f_{bound} = n \frac{K \cdot V_{free}}{1 + K \cdot V_{free}} \quad (5.13)$$

However, the binding constant described here strongly depends on the size of vesicles. In order to obtain a general form, which is independent of the vesicles, the binding constant is usually defined in terms of lipid concentration instead of vesicle concentration. The binding can be treated as bimolecular reaction of protein and lipid with a binding constant as given by equation 5.12:

$$K = \frac{PL}{L_{free} \cdot P_{free}} \quad (5.14)$$

where PL is the number of bound proteins, L_{free} , the number of free lipids and P_{free} the number of free proteins. The fraction of bound proteins can be directly deduced from equation 5.4:

$$f_{bound} = \frac{K \cdot L_{free}}{1 + K \cdot L_{free}} \quad (5.15)$$

Since large unilamellar vesicles consist of a lipid bilayer, only half of the lipids are exposed to the surface and accessible for binding. This is sometimes considered by defining the binding constant in terms of accessible lipid, which differs from the total amount of lipid by a factor of two [28].

Another way to describe binding of proteins to lipids, which is often used in literature about protein-membrane interactions within hemostasis, assumes that i lipids form one binding site [6, 29]. Consistently the resulting binding constant K_{iL} is related to the binding constant in terms of lipids, K_L , by:

$$K_{iL} = i \frac{PL_i}{P_{free} \cdot L_{free}} = i \cdot K_L \quad (5.16)$$

However, the number of lipids bound per protein, i , is not experimentally accessible in most cases. Hence, in order to obtain general results and to enhance fitting accuracy by minimization of the number of free fit parameters, the binding constant in terms of total lipid concentration as given by equation 5.14 is used in this thesis.

In the case that the smaller proteins are fluorescently labeled, FCS measures the fraction of bound proteins with respect to the total amount of protein in the sample. Thus, FCS measurements can be used for the determination of the fraction of bound proteins as a function of the lipid concentration resulting in binding isotherms as described above. From these, the binding constant K can be determined with a fit according to equation 5.15. The concentration of unbound lipids, however, is not known and has to be replaced by the total concentration of lipids L , consisting of the unbound and bound lipids. This yields a quadratic equation, which is solved by:

$$f_{bound} = \frac{K^{-1} + P_{total} + L - \sqrt{(K^{-1} + P_{total} + L)^2 - 4L \cdot P_{total}}}{2P_{total}} \quad (5.17)$$

In the case of excess lipids (i.e. $L \gg PL$), the concentration of free lipids L_{free} can be replaced by their total concentration, leading to an equation, which is much simpler as compared to the general case [7]:

$$f_{bound} = \frac{K \cdot L}{1 + K \cdot L} \quad (5.18)$$

Since this work dealt only with binding under conditions of excess lipids, equation 5.18 was exclusively used to fit binding isotherms.

To extract the fraction of proteins bound to vesicles by FCS measurements, complicated corrections are sometimes applied to consider possible effects due to several labeled proteins binding to one vesicle, which lead to an enhanced brightness of the bound complex [7]. This is only necessary, when the number of bound complexes needs to be determined. In order to measure the binding constant with equation 5.18, however, the number of bound proteins relative to the total amount of proteins is the experimental parameter and in this case no corrections have to be performed, since any possible effects cancel out (if quenching upon binding is negligible as in this thesis):

According to equation 4.8 the autocorrelation function resulting from a binding measurement is given by:

$$G(\tau) = \frac{\sum q_i^2 N_i g_i(\tau)}{(\sum q_i N_i)^2} \quad (5.19)$$

Assuming for simplicity that only two possible species are present, free proteins and complexes of m proteins bound to one vesicle, which exhibit an m -fold enhanced brightness as compared to the free proteins, the autocorrelation resulting from an FCS measurement reads:

$$G(\tau) = \frac{\sum q_i^2 N_i g_i(\tau)}{(\sum q_i N_i)^2} = \frac{N_{free}}{(N_{free} + mN_s)^2} g_{free} + \frac{mN_s}{(N_{free} + mN_s)^2} g_s \quad (5.20)$$

where N_{free} is the number of free proteins, N_s the number of slowly diffusing complexes of m proteins bound to one vesicle and g_{free} and g_s are the characteristic autocorrelation functions of the free proteins and the complexes, respectively. The apparent number of particles N determined from this equation by a comparison with equation 4.8 is $N = N_{free} + mN_s$. The real number of particles is given by the number of free proteins plus the number of complexes $N_{free} + N_s$ and is thus overestimated by the measurement. The total number of proteins P_{tot} , however, consists of the sum of the number of free proteins N_{free} and the number of bound proteins mN_s :

$$P_{tot} = N_{free} + mN_s \quad (5.21)$$

Hence, it is exactly revealed by the apparent number of particles in the measurement. The effects due to the brightness enhancement of the complex by the factor of the number of bound proteins and the reduction of the number of detected proteins due to the binding of n proteins to one vesicle, which are then detected as one particle, cancel out. The same applies to the measured fraction of bound proteins $f_{measured}$, which is determined from a fit according to equation 5.20 to be:

$$f_{measured} = \frac{mN_s}{N_{free} + mN_s} \quad (5.22)$$

Since mN_s reveals the total amount of bound proteins and the total number of proteins P_{tot} is $N_{free} + mN_s$ as layed out above, the measured fraction of bound proteins $f_{measured}$, yields the fraction of bound proteins as used in equation 5.18 without the need of any corrections. This case, which was restricted to two species of free protein and m proteins bound to one vesicle, can be easily generalized to any number of species and hence, the measured fraction of bound protein can be directly used for the determination of binding constants with equation 5.18.

5.2 Association and dissociation rates

Time-resolved experiments allow for the determination of the evolution of free protein with time. The resulting data can be used to obtain the association and dissociation rates of the binding process. For a reversible process, according to the reaction scheme as described by equation 5.1, which is expressed in terms of protein concentration P and lipid concentration L as follows:



the association rate is given by [30]:

$$-\frac{dP}{dt} = k_{ass} \cdot P \cdot L_{free} - k_{diss}PL \quad (5.24)$$

If k_{diss} is negligible, the process can be considered as irreversible and the corresponding expression of the temporal evolution of the concentration of free protein reads:

$$-\frac{dP}{dt} = k_{ass} \cdot P \cdot L_{free} \quad (5.25)$$

In the case of excess lipid, this equation can be solved, yielding the time-dependent concentration of free protein:

$$P(t) = P_{tot} \cdot \exp(-k_{ass}Lt) \quad (5.26)$$

where P_{tot} is the concentration of free protein at time zero. This equation can be used to determine the association rate from a measurement of the concentration of free protein as a function of time starting at the time when the reaction partners are mixed together until equilibrium is reached.

In order to determine the dissociation constant of a reversible process, equilibrium has to be shifted toward the left [30]. This can be achieved either in a dilution experiment or by addition of excess unlabeled protein. The dissociation rate is then measured by the evolution of the bound complexes with time and is given by [30]:

$$-\frac{dPL}{dt} = k_{diss} \cdot PL \quad (5.27)$$

Integration yields the time-dependence of the concentration of bound complexes, which is used to determine the dissociation rate experimentally:

$$PL(t) = PL_0 \cdot \exp(-k_{diss}t) \quad (5.28)$$

The relation of equilibrium binding constant, association- and dissociation rate is easily obtained from equation 5.24 to be:

$$K = \frac{k_{ass}}{k_{diss}} \quad (5.29)$$

Hence, equation 5.18 and 5.17 can be used to determine the equilibrium constant from a titration experiment and the association and dissociation rates can be measured by time resolved experiments with FCS employing equation 5.26 and 5.28, respectively. Since the temporal resolution of FCS is too low to resolve diffusion-limited binding processes, the association rate of such processes has to be calculated with equation 5.29.

5.3 Mechanisms of and influences on protein-membrane binding

The equilibrium binding constant K as defined above is related to the binding energy ΔE by

$$\Delta E \propto \ln(K) \tag{5.30}$$

Based on this relation, the binding constant, particularly its dependence on distinguished parameters can give evidence on the properties of the binding energy and hence the underlying binding mechanisms. The mechanisms of protein-membrane binding are often complex and composed of several interactions. An important mechanism in this context is the insertion of hydrophobic protein tails into the bilayer. This is for instance observed for FVIII binding to phospholipid membranes [31]. In this case the insertion of hydrophobic parts of the protein follows a first rapid binding process mediated by electrostatic interaction, one of the most important interactions leading to protein-membrane binding [32]. Electrostatic binding to a charged membrane can be described theoretically employing the Poisson-Boltzmann equation. In the case of a homogeneous charge distribution this yields an exponential dependence of the binding energy on the relative charge content of the membrane [33]. Experimentally, this was shown for instance on MARCKS peptide binding to negatively charged phosphatidylserine containing membranes [7] and on small basic Lys peptides binding to membranes containing acidic lipids [28]. This relation holds only for homogeneous charge distributions on the membrane. The composition of membranes however often varies locally and thereby imposes an additional complexity to the binding mechanism. Binding of proteins to membranes can for example induce demixing of the membrane or lead to an accumulation of certain lipids near the binding site. These influences of the membrane composition on protein-membrane interactions play an important role for the regulation of such processes and were found in many biological systems. This kind of regulation by spatial organization is for example found for the polyvalent acidic lipid phosphatidylinositol 4,5-bisphosphate (PIP_2), which is sequestered by membrane-adsorbed basic peptides due to electrostatic interactions [4,5]. Another example is the formation of microdomains on the plasma membrane of T cells induced by membrane-bound protein-protein networks that exclude or trap signaling molecules [34].

In addition to spatial organization, coating of the membrane can have a significant influence on its interaction with proteins. Polymer coatings, for instance, are used to

create a steric barrier which acts as repulsive mechanism and thereby protects the lipid bilayer from close approach of proteins and other macromolecules [35].

These were some, but by far not all cases of the interaction of membranes and their composition with protein-membrane binding. However, not only the membrane, but also the protein conformation plays an important role for protein-membrane binding. Some proteins have to be activated to be able to bind to membranes. Annexin B12, for instance, needs to assume a membrane-competent formation before it binds to phospholipid membranes [36]. Other proteins, such as amyloid- β undergo conformational changes, which are induced by their insertion into a membrane [37].

All the parameters and scenarios layed out above influence the binding constant and might lead to remarkable binding behaviours which might be challenging to investigate.

6 Diffusion measurements in crowded, scattering media

FCS is a well established technique for measurements in dilute solutions, its performance in complex fluids remains, however, a challenge since scattering and hydrodynamic effects due to crowding strongly influence the experiments. In the context of this thesis, it was desirable to measure in plasma, the natural environment of blood coagulation, and in highly concentrated vesicle solutions, which both are complex media. The challenge is to separate the influences of the medium, which might lead to artifacts [22], from the measurement to allow for reliable data analysis. Once this is achieved, FCS experiments can be performed in any complex medium, thereby enabling measurements under biologically relevant conditions. Here, FCS is performed in highly concentrated vesicle solutions, which represent a well-defined crowded model system, to investigate the particular corrections related to scattering and hydrodynamic effects. The results show, that both, scattering as well as the decrease in diffusion constant due to crowding, can be quantitatively described consistently with theory. The corrections derived from these findings are applied to measure the binding isotherm of annexin V to PS-vesicles in a highly concentrated PEGylated vesicle solution yielding the same binding constant as in buffer and hence, verifying the corrections. Furthermore, consequences of these findings for calibration and measurements in blood plasma and in living cells are discussed. The results of this chapter are published in [38].

6.1 Complex media

In the following chapters several FCS experiments, which were performed in complex media, will be presented. To measure in the natural surrounding of blood coagulation and thereby prove the relevance of the results of FVIII binding to membranes (chapter 7), measurements were carried out in blood plasma. Blood plasma, however, is a strongly scattering, crowded fluid. Due to the low binding the experiments on annexin binding to PEGylated vesicles described in chapter 8 had to be performed at very high vesicle concentrations which lead to scattering (Fig. 6.1) and hydrodynamic effects. Likewise, the molecular environment of many other biological systems is highly concentrated and heterogeneous and thus profoundly more complex than solutions of purified components *in vitro*. Twenty to thirty percent of the intracellular space is occupied by globular protein, fibrils or lipid membranes, a fact, that is described by the term

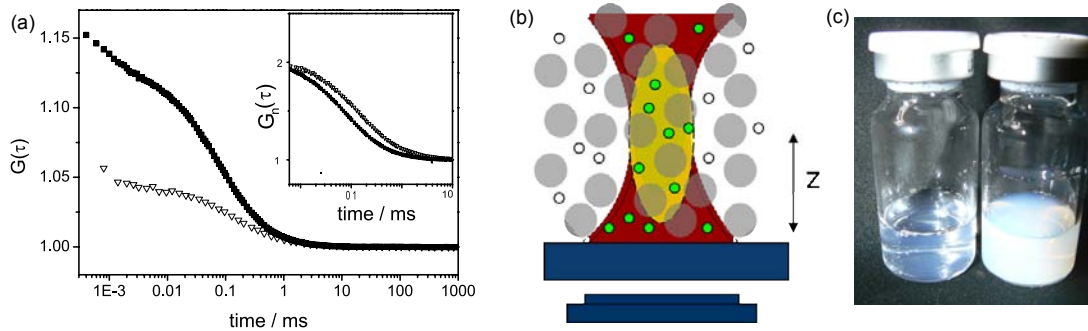


Figure 6.1: (a) Autocorrelation of eGFP in buffer (■) and in 25% volume fraction vesicles (▽). Inset: comparison of the normalized autocorrelation. (b) Illustration of the illumination profile in a concentrated vesicle solution. Solid lines represent the focus in buffer solution, while dashed lines represent the distorted focus resulting from scattering. eGFP molecules in the focal volume are excited and their intensities can be detected. Buffer and concentrated vesicle solution (25%) are shown in (c).

macromolecular crowding [39–41]. In recent years many biophysical implications of crowding have been investigated. It has become evident that the space filling properties of cellular components significantly alter the dynamic viscosity of the solution [42–44]. The reduced mobilities have an immediate consequence on reaction rates and transport properties. Moreover, excluded volume can have an immediate effect on equilibrium constants. In particular, binding can be affected solely by the surrounding colloidal solution or by some of its components, as is the case for annexin regulation of FVIIIa binding in plasma, which is shown in chapter 7 to be much more efficient as compared to buffer solution [39, 45]. Therefore, it would be desirable to measure protein binding in its natural environment, which may be the intracellular space, tissue or plasma in the case of the coagulation factors investigated in this thesis. Protein interactions are likewise of technical importance in complex fluids such as microemulsions, creams or pharmaceutical products. In all cases, complex soft matter systems with high volume fractions of material, that adopt a mesoscopic internal structure, are considered. As a consequence of these properties, these solutions are often optically turbid making analysis by optical techniques optimized for measurements in dilute buffer solutions difficult. Moving to natural solutions bears experimental challenges; for instance, cells and plasma scatter light resulting in both enhanced background and obscured signals. Consequently, caveats regarding quantitative evaluation and calibration apply and careful validation is required in each particular case.

6.2 Scattering effects

In order to investigate the influence of complex media on the measurements, FCS experiments on eGFP in buffer and in concentrated solutions of PEGylated vesicles were compared. PEGylated vesicles were chosen to form an inert, well-defined and tunable crowded medium and eGFP served as inert and bright fluorescent tracer molecule. The vesicles were obtained from Bayer Health Care and were confirmed to be monodisperse and of a radius of 45 nm. Fig. 6.1 (a) shows an autocorrelation curve of eGFP in buffer and the autocorrelation of eGFP in concentrated vesicle solution. With increasing vesicle concentration, the amplitude, $G(0)$, of the autocorrelation curve decreases, while at the same time the diffusion time increases (as seen from the insert which displays the normalized autocorrelation curves). These effects are due to scattering and hydrodynamic slowdown as will be discussed later. The amplitude $G(0)$ of the eGFP autocorrelation function and hence, the apparent size of the effective confocal volume, was noted to become unusually sensitive to the focal depth when measured in vesicle solutions. As schematically shown in Fig. 6.2(a), this is due to scattering, which distorts the focal volume with increasing length of the light path through the crowded medium. A measurement of the relative change of the focal width $\omega_x(z)/\omega_{x0}$ and height $\omega_z(z)/\omega_{z0}$ as a function of focal depth is displayed in Fig. 6.2(c). To analyse the autocorrelation functions of these measurements, equation 4.4 was rewritten using the concentration $c = N/V$, the diffusion coefficient D according to equation 4.5 and the Gaussian focal volume $V = \pi^{1.5}\omega_x^2\omega_z$:

$$G_{diff} = \frac{1}{c \cdot \pi^{1.5}\omega_x^2\omega_z} \cdot \frac{1}{1 + \frac{4D\tau}{\omega_x^2}} \cdot \frac{1}{\sqrt{1 + \frac{4D\tau}{\omega_z^2}}} \quad (6.1)$$

In this equation, the fit parameters can be separated into those dependent on the solution only and those dependent on the optical setup. Parameters, like the diffusion time or the average particle number in the focus, which link the characteristics of the solution with the optical parameters, are eliminated. In the measurements investigating the focal volume as a function of the focal depth, concentration and diffusion coefficient of the solution are constant and well known, since they are independent on the focal depth. Hence, they can be used as fixed parameters and equation 6.1 allows for the direct determination of the focal width and height, particularly, their variations in these experiments.

Comparison of the two curves in Fig. 6.2 (c) obtained from two-parameter fits according to equation 6.1 to the measured autocorrelation curves reveals a two-fold change in focal height ω_z whereas broadening in the x-direction is limited to about 10%. A control experiment in buffer did not show any dependence on the focal depth over the whole range of distances used for the experiments in vesicle solution.

To further investigate the nature of scattering in concentrated vesicle solutions, the transportation mean free path in the vesicle solutions was measured using coherent

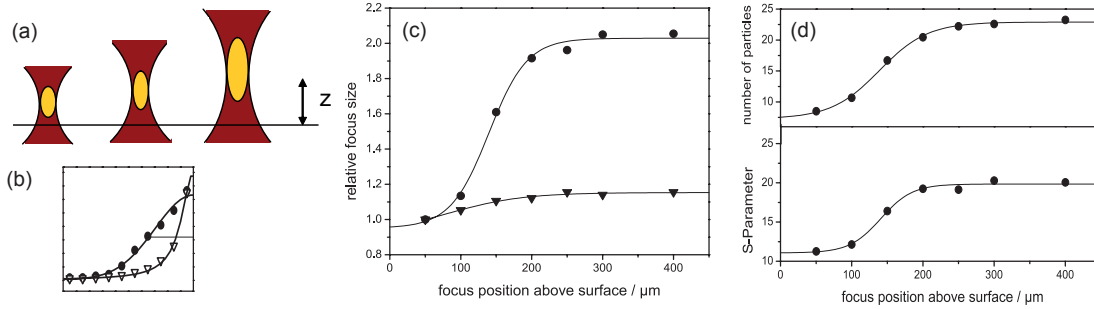


Figure 6.2: (a) Schematic diagram of the distortion of the focus as a function of the length of the light path (focal depth) through the scattering medium. (b) Broadening of the focus profile in x - (∇) and z - (\bullet) direction as obtained from simulations. (c) Width (\blacktriangledown) and height (\bullet) of the focus as a function of focal distance to the chamber surface determined from a fit according to equation 6.1. (d) Number of particles and structure parameter S increase significantly as the distance of the focus from the chamber slide surface increases.

backscattering experiments. Here, the sample was illuminated by a laser beam and the scattered intensity in the backward direction was detected. The cone of the coherently backscattered light is a measure of the transportation mean free path [46, 47]. In the vesicle solutions, the transportation mean free path was much longer ($> 5\text{mm}$) than the path of light in the sample ($\sim 200\mu\text{m}$). From that one can conclude that the scattering process is in the single scattering regime and isotropic multiple scattering can be excluded [46]. As a consequence, scattering is not necessarily isotropic. As we are dealing with spheres of 100 nm size compared to several hundred nm wavelength, most of the light is scattered in forward and backward direction [47]. Simulations written in Matlab confirm the findings from FCS analysis, that scattering from 100 nm spheres elongates the focus along the beam direction. Data obtained from these simulations are shown in Fig. 6.2(b) and provide a qualitative proof that broadening of the focus due to scattering is much stronger along beam direction than perpendicular to it. Simulations are written assuming that all photons are focussed on one spot and during their path in the scattering medium they are scattered with a probability depending on the density of vesicles. Vesicles are distributed on a grid and photons, which pass a grid point occupied by a vesicle, are scattered. The scattering angle and hence, the new propagation direction of the photon is determined from the scattering profile of spheres as described in Meller et al. [48].

As shown in Fig. 6.2(d), the anisotropic scattering leads to a drastic increase in the S-Parameter S with increasing focal depth and has to be taken into account for all measurements in scattering media. As S usually is determined once in a calibration measurement and then fixed for all following experiments, the increase in S has immediate consequences on the calibration procedure. However, due to the independence of the

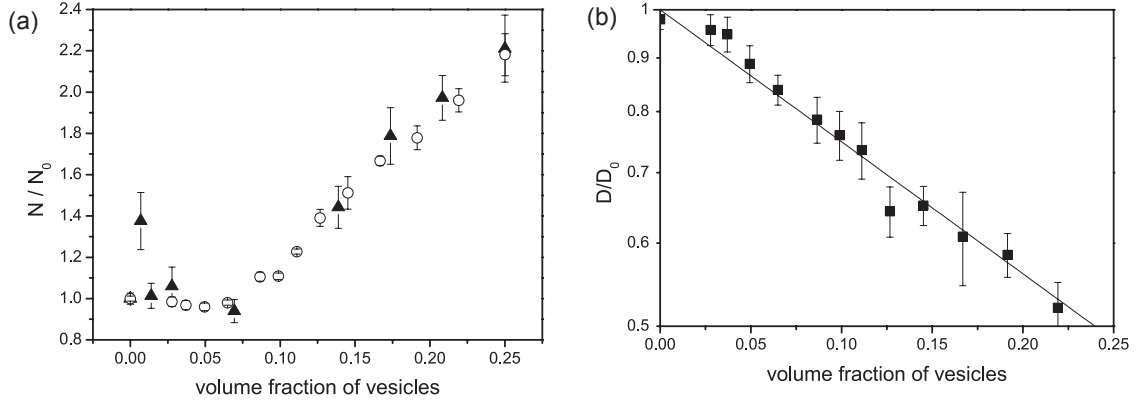


Figure 6.3: (a) Relative increase in number of particles in the confocal volume plotted against the volume fraction of vesicles for eGFP (○) and antibodies (▲). (b) Semi-log plot of the relative change of diffusion coefficient as a function of the volume fraction of vesicles. The line represents an exponential fit

scattering effects (and hence the increase of S) from the tracer molecule, calibration can be done separately in each scattering medium with a standard tracer molecule, such as eGFP. The curves in Fig. 6.2 also show, that from $250\mu m$ there is a saturation regime, where slight variations in the focus position do not influence its shape and size noticeably. In this thesis, all experiments in complex media were performed in this regime to obtain stable results.

As a next step, the evolution of the confocal volume at fixed focal depth but with increasing vesicle volume fraction was investigated. The data were obtained by fitting equation 4.4 with free fit parameters N , S , and τ_D . Due to scattering the number of particles in the focal volume increases with increasing vesicle concentration. Fig 6.3(a) shows the increase in the apparent number of chromophores in the focal volume starting at a volume fraction of about 7% and then increasing steadily with volume fraction. Data were acquired using eGFP and fluorescently labeled antibodies as tracer molecules. Both data sets exhibit the same behavior. Consequently, the apparent number effect is independent of the tracer molecule which was expected since the effect occurs from the distortion of the focal volume due to scattering.

6.3 Hydrodynamic slowdown

The diffusion coefficient, as determined from these measurements using equation 4.5, decreases significantly with increasing vesicle concentration. This remarkable slowdown is not an artifact due to focal broadening, but rather due to crowding. Fig. 6.3(b) shows the change of diffusion coefficients D relative to the value in buffer, D_0 , as a function of the vesicle concentration. The semi-log plot reveals an exponential dependence of D/D_0

on the volume concentration of vesicles:

$$D/D_0 = \exp\left(-\frac{\phi}{\phi_c}\right) \quad (6.2)$$

with the critical volume fraction ϕ_c fitted to be 0.35. This result is consistent with the exponential dependence as found in many crowded systems. The change of the effective viscosity in a colloidal suspension was first described by Einstein [49]. For crowding agent concentrations studied here, hard sphere models of diffusion employing scaled particle theory [50, 51] and Brownian dynamics simulations [52] predict exponential dependencies. The experimental results presented here, serve as an elegant confirmation of these predictions. Additionally, they agree very well with measurements in soft matter systems such as Ficoll 70 [53] and micelle solutions [54], as well as those in biological systems, such as hemoglobin in red blood cells [55]. Consequently, concentrated liposome solutions qualitatively exhibit the expected crowding behavior. Within experimental errors, the diffusion coefficients are also consistent with the rigorous theory of diffusion in hard sphere colloidal suspensions [50, 51].

For FCS experiments in crowded media, this change of the diffusion coefficient bears important consequences, since the diffusion coefficient cannot be used for calibration in the usual manner. Furthermore, when the diffusion time is used to determine interactions in a crowded medium, the hydrodynamic slowdown needs to be distinguished from specific changes of the diffusion constant due to reactions such as binding to macromolecules or vesicles.

6.4 Consequences for applications

6.4.1 Calibration

Since any scattering medium or any medium having a refractive index different from water changes the focal volume with respect to the standard volume in water, calibration is one of the major challenges when it comes to performing FCS measurements in soft matter [22, 23]. To overcome this issue, other groups have developed new FCS techniques where an additional length scale introduces a robust intrinsic calibration, as already shortly mentioned in chapter 4.3. Dual focus FCS [56], for instance, uses the distance of the two foci for calibration, while scanning FCS [57–59] is calibrated via the scanning velocity. Another option used with increasing frequency, especially for measurements in cells, is two-photon FCS, where scattering is strongly reduced due to the long excitation wavelengths [60]. The experiments described above show that even without these techniques, reliable results can be achieved by considering the fact that the distortion of the focal volume due to scattering is independent of the tracer molecule and can thus be determined separately in an appropriate calibration measurement. This allows for the introduction of reliable calibration in scattering media.

6.4.2 Binding experiments

A particular interest within the context of this thesis are binding experiments in complex media. The performance of FCS binding experiments in such media was tested with the specific binding of annexin V to PS-vesicles in a solution of 25% vol PEGylated vesicles. As discussed in chapters 7 and 8, annexin V binds specifically to PS-lipids in a calcium-dependent manner, but does not show any specific binding to POPC-vesicles. The challenge is to separate the FCS signal changes due to scattering and crowding from changes resulting from binding events. FCS experiments were performed as a function of increasing concentrations of PS vesicles in solutions with fixed amounts of Alexa-labeled annexin in both, pure citrate buffer as well as a crowded PEG-liposome solution, each with calcium added in a concentration of 50 mM. The fractions of free proteins, f_{free} , and proteins bound to PS vesicles, f_{bound} , were determined according to equation 4.9, making use of the fact that the diffusion constant of free and vesicle-bound annexin differs by about a factor of 10.

Data evaluation was done for all data sets as follows: to achieve reliable fitting results for the fraction bound in a two-component analysis, the diffusion time of free protein and the structure parameter were fixed. As described above, it is important to consider the fact that the diffusion times, as well as the structure parameter vary with the volume fraction of the vesicle medium. The corrections for the scattering effect and slowdown due to crowding could be taken directly from Fig. 6.3(a) and (b) as determined from the GFP test experiments. The structure parameter at a certain vesicle concentration can then be calculated using equation 4.6 and the value of the particle number at that vesicle concentration taken from Fig. 6.3(a). The diffusion time at a certain vesicle concentration can be determined using equation 4.5 and the corresponding diffusion constant shown in Fig. 6.3(b). However, this way of making the corrections is based on the assumptions that the change of the focal volume in x- direction due to scattering is negligible and that the investigated molecule is as inert as GFP in the crowded medium. The later is not the case for annexin V, for instance, which shows weak unspecific binding to PEGylated vesicles as described in chapter 8. Alternatively, the diffusion time and structure parameter for Alexa-labeled annexin in PEGylated vesicles can be directly measured in the crowded medium. Here, this was done by measuring annexin diffusion in a PS-free PEGylated vesicle solution. The structure parameter and diffusion time were determined from this measurement using equation 4.4 and then kept fixed for the succeeding analysis of experiments with increasing fraction of charged vesicles. Using equation 4.9, the fraction of free and bound annexin was determined. A typical two-component curve of annexin binding to PS-vesicles in highly concentrated PEGylated vesicle solution is shown in Fig. 6.4(a), and the resulting binding curve is shown in Fig. 6.4(b). Following the FCS experiment of annexin binding in highly concentrated vesicle solutions with increasing amount of PS-vesicles measurements were carried out in buffer. The binding curve determined in buffer and in concentrated PEGylated vesicle suspension match well. The use of corrected diffusion constants for FCS data in

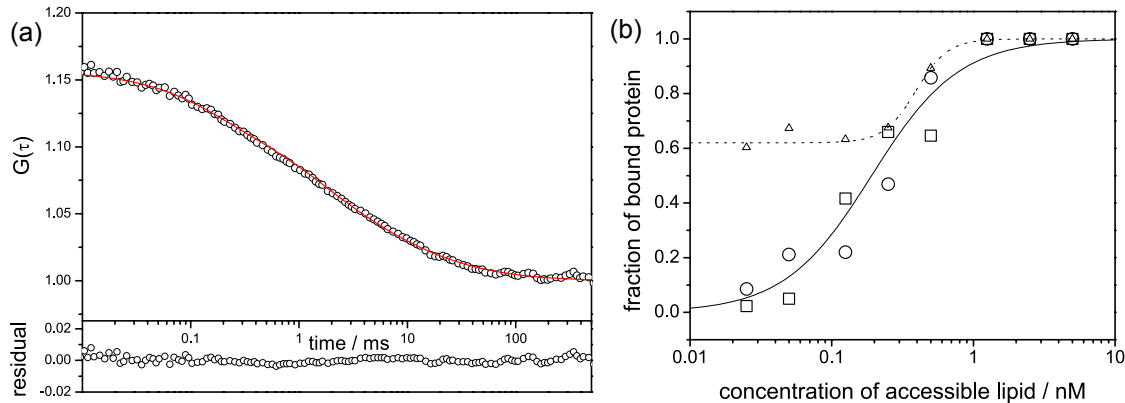


Figure 6.4: (a) Measured autocorrelation curve of annexin binding to PS-vesicles in highly concentrated PEGylated vesicle solution (\circ) and the corresponding fit curve. Residuals are shown below. (b) Fraction of annexin bound to PS-vesicles as a function of the PS-vesicle concentration measured in buffer solution (\square) and in highly-concentrated PEGylated vesicle solutions (\circ). Uncorrected data in highly-concentrated PEGylated vesicle solutions (\triangle) lead to an overestimation of binding.

crowded medium for both the free and bound annexin is critical as shown by the dashed line which indicates the outcome of the analysis without correction. Hence, binding measurements in highly concentrated vesicle solutions can be carried out if the optical, as well as hydrodynamic influences of the crowded medium, are taken into account. These findings allow for FCS measurements of dynamics and molecular interaction in turbid and crowded media. Thus, these results provide a basis for measuring and analyzing colloidal solutions used for pharmaceutical and cosmetic applications as well as in food industry.

6.4.3 Blood plasma

The results of the investigation of the FCS performance in complex media also allows for experiments in blood plasma. Plasma is a yellow, strongly scattering fluid, crowded with macromolecules such as for example coagulation factors. Using Alexa-labeled antibody as fluorescent tracer molecule, the S-parameter in plasma was measured to be enhanced by a factor of 3 as compared to buffer solution. The slowdown of diffusion due to crowding in plasma was determined for tracer molecules of different size as shown in Fig. 6.5. For all tracer molecules, diffusion was slowed down by a factor of 1.8, which is even more than the slowdown at the highest concentration of PEGylated vesicles of 0.25% vol. Hence, the corrections for binding experiments as described above for annexin are even more important. Interestingly, the slowdown does not depend on the size of the tracer molecule in this range of sizes, whereas Dix et al. [43] report a strong size dependence of the slowdown for DNA. However, this difference might be due to the

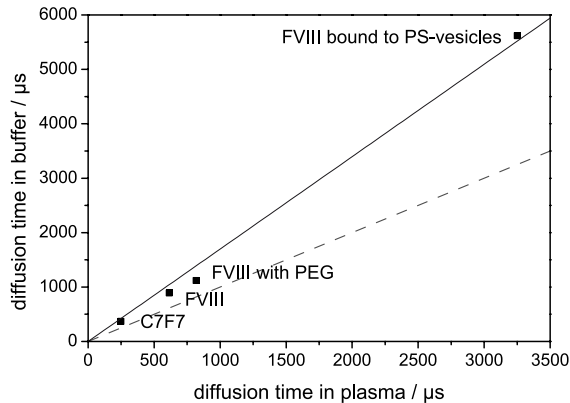


Figure 6.5: Diffusion time of several tracer molecules in buffer as a function of their diffusion time in plasma. The solid line represents a linear fit, revealing an enhancement of diffusion time in plasma by a factor of 1.8 as compared to buffer. Comparison with the dashed bisecting line shows the deviation of the values in plasma from those in buffer.

shape of DNA and the big range of sizes they investigated.

As shown in chapter 7, binding in plasma could be successfully measured with these corrections. This demonstrates that FCS is a powerful tool for performing binding assays under physiological conditions, which is a very promising feature for applications in research and diagnostics.

6.4.4 Cell experiments

Another application of FCS in scattering, crowded media, are in-vivo experiments in cells. In scattering media, a strong increase in the distortion of the focal illumination volume with increasing light path in the medium was found until saturation is reached. This allows one to conclude that experiments on the surface of the cover slip, as performed when making measurements in living cells growing on the surface of the cover slip, are less influenced by scattering than measurements in an equally-scattering soft matter system in solution, which is typically investigated at a standard focal distance of $200\mu\text{m}$ above the cover slip surface. However, measurements at the surface have to be performed at a very stable focus height, since they are more sensitive to small deviations in focus height as compared to measurements performed in saturation regime.

Eucaryotic cells are reported to be composed of up to 30% volume fraction liposomes [39–41]. Based on this value, the value of $\phi_c = 0.35$ reported above suggests that the hydrodynamic slowdown due to crowding reduces the diffusion coefficient in cells by a factor of 2. Given that the ratio of the diffusion coefficient of GFP in water to that in living eucaryotic cells has been reported to be 3-4 [40], the results which only

take into account hydrodynamic slowdown in crowded solutions of hard spheres do not explain the reduction completely. Additional effects, such as binding of GFP to cellular components or hydrodynamic slowdown due to diffusion in actin networks, which reduce diffusion much more than soluble spherical macromolecules [61], might cause this further reduction of the diffusion constant. No indication of anomalous diffusion was seen in the model liposome system. For diffusion in eucaryotic cells, however, there are controversial discussions on anomalous diffusion. While some authors report anomalous exponents between 0.8 and 0.9, others do not see anomalous behavior [43]. The results of the vesicle model system indicates that liposomal crowding alone will not account for anomalous diffusion. However, a polymerized actin network or a solution of polydisperse crowding agents could induce subdiffusive behavior.

Based on these findings, the chosen model system of concentrated vesicle solutions, which permit to distinguish between influences due to scattering and hydrodynamic effects and facilitate the control of the influence of crowding via changes in vesicle concentration, provides a good basis for studies on crowding in cells. Furthermore, the results on the influence of scattering and crowding on the performance of FCS experiments allow for reliable FCS measurements in living cells.

7 Membrane-binding of Factor VIII within blood coagulation

7.1 FVIII binding to membranes

7.1.1 Hemostasis

Hemostasis is a complex mechanism of the circulatory system that prevents the body from bleedings. The hemostatic process, which takes place upon an injury, can be split into two major steps. First, thrombocytes adhere with the glycoprotein-complex GPIb/IX acting as a receptor to subendothelial collagen in a reaction mediated by van Willebrand Factor. In a second step, this thrombocyte matrix is stabilized by a dense fibrin network. The establishment of this fibrin network is product of a complex system of interactions of coagulation factors and is called blood coagulation cascade (Fig. 7.1) [62]. This cascade consists of two pathways, an extravascular and an intravascular pathway, which both lead to the activation of the proenzyme Factor X. In its turn, Factor X together with FVa builds an enzyme-complex leading to the conversion of prothrombin into thrombin. Thrombin, which is the key enzyme of the coagulation cascade, activates fibrinogen and thereby enables it to build a stable polymer network. Activation of Factor X via the extravascular pathway is done by a complex of membrane-activated Factor VII, membrane-bound tissue factor and calcium. The intravascular pathway involves activated FVIII (FVIIIa) and FIX building the membrane-bound tenase-complex, which then activates factor X. In this step, the formation of the tenase complex confines blood coagulation to the surface of the membrane, which is of great importance, since it concentrates the tenase complexes, provides optimal mutual orientation of the tenase components and limits coagulation to the injured tissue. The intravascular pathway works 50-fold more efficiently than the extravascular pathway. Consequently, a dysfunction within the intravascular pathway leads to severe bleeding disorders. Hemophilia A, probably well known through its occurrence in the British Royal family, is one example of such diseases [63]. In this case, deficiency of Factor VIII blocks the intravascular pathway and hence severe bleedings can not be stopped.

7.1.2 Structure, activation and catabolism of FVIII

As described in the previous paragraph, FVIII is a key protein of the coagulation cascade and its deficiency leads to severe bleeding disorders. Being a 330 kDa glycoprotein of 2332

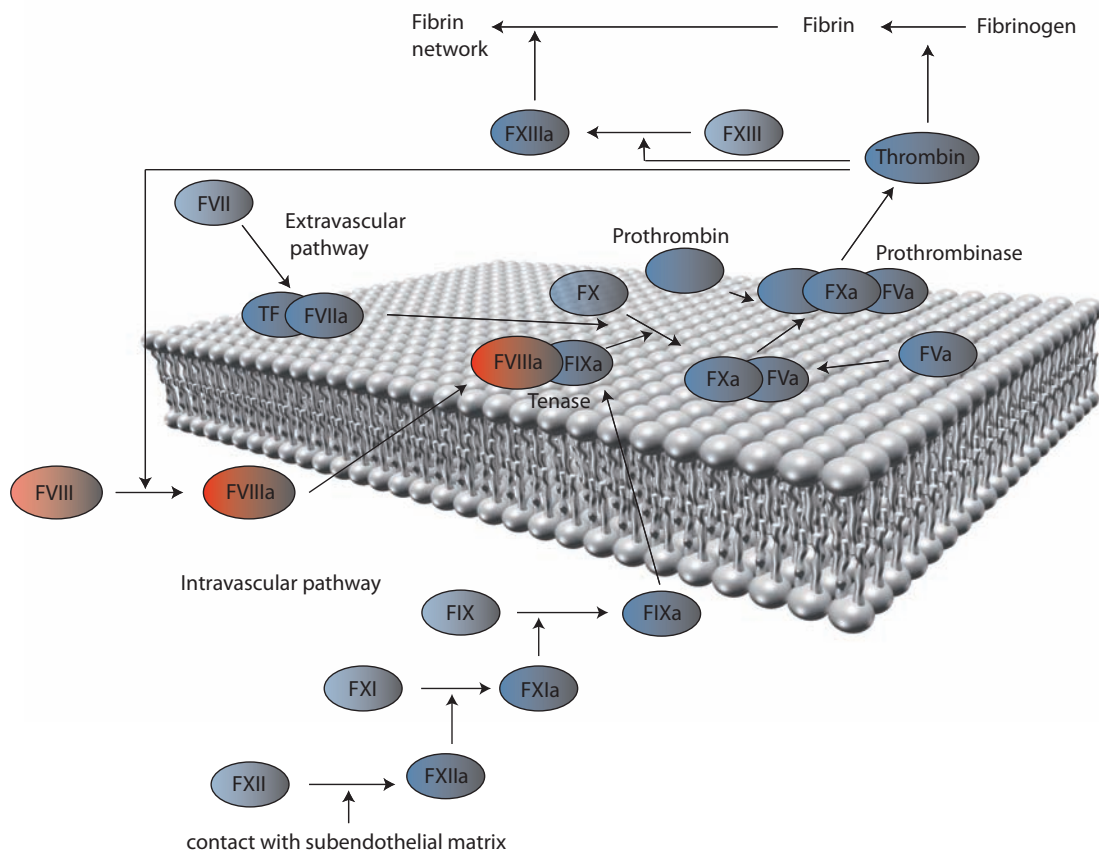


Figure 7.1: Schematic drawing of the reaction network of the coagulation cascade.

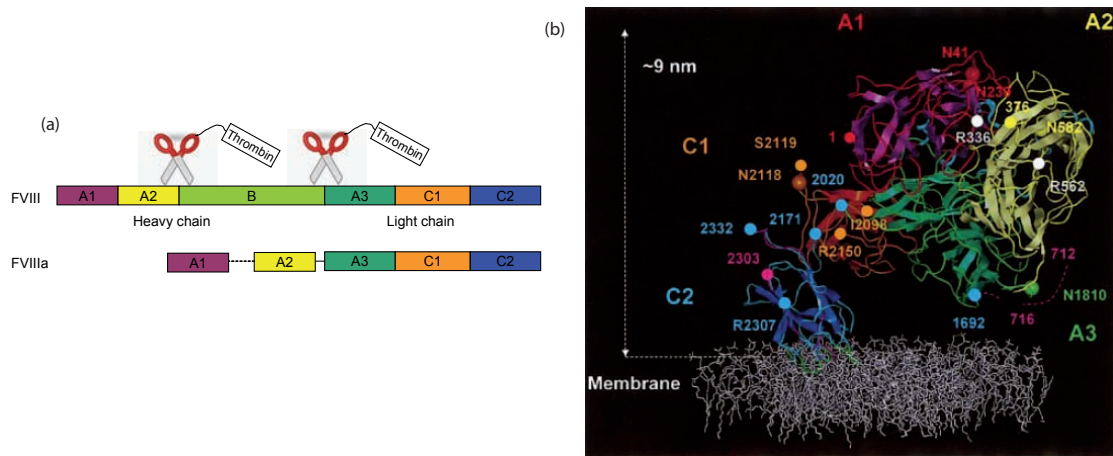


Figure 7.2: Molecular structure of FVIII. (a) Domains of FVIII. The protein is activated through cleavage by thrombin, which removes the B-domain. (b) Structure of membrane-bound FVIII as reconstructed from electron crystallography data [31].

amino acid residues, FVIII consists of three homologous A-domains, two homologous C-domains and one B-domain, which are ordered as follows: A1-A2-B-A3-C1-C2 (Fig. 7.2) [3]. Released into the circulatory system, FVIII immediately forms a complex with von Willebrand factor. This tight binding to von Willebrand factor prevents FVIII from building the tenase-complex with Factor IX and protects FVIII from inactivation by protein C, FIXa and FXa. The von Willebrand factor binding sites on FVIII are located at the C1, C2 and the A3 domain (at its part next to the B-domain) [64]. Activation of FVIII is done mainly by thrombin through cleavage of the B-domain (Fig. 7.2), which coincides with a conformational change of the C2-domain [65]. This cleavage removes the protecting von Willebrand factor and hence allows activated FVIII (FVIIIa) to interact with FIXa and thereby leads to the formation of the tenase-complex. The catabolism of FVIII has been found to be mediated by low-density lipoprotein receptor-related protein (LPR) and heparan sulphate proteoglycans (HSPGs), one of the major glycoprotein components of the extracellular matrix. According to the model suggested for the FVIII catabolism, initial binding of the FVIII/von Willebrand factor complex to the cell membrane occurs mainly via interaction with HSPGs. Bound to the cell surface, FVIII is either taken up by LPR mediated endocytosis or by LPR independent endocytosis, which is possibly mediated directly by the HSPGs, whereas von Willebrand Factor does not enter the endocytotic pathway [65].

7.1.3 Labeling of FVIII via antibodies

Binding measurements using FCS as presented in this and the following chapters provide a great potential for applications in research, diagnostics and quality control of e.g. pharmaceutical, cosmetical or food products. For all these applications a quick, easy

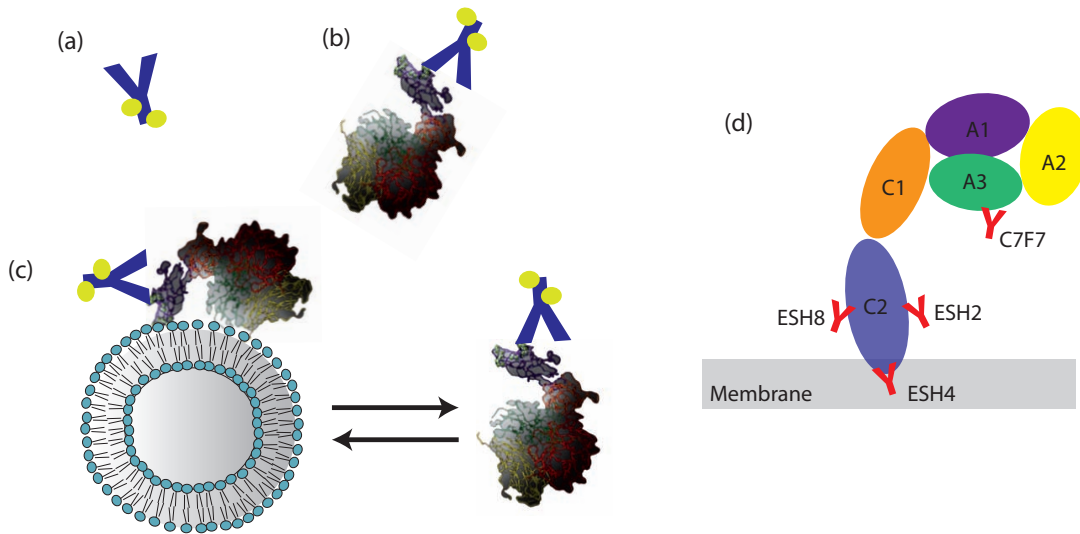


Figure 7.3: *Fluorescent labeling via antibodies: fluorescently labeled antibodies (a) bind to the protein (b) and can be used to investigate binding of the protein to unlabeled vesicles (c) with FCS. (d) Schematic drawing of FVIII binding to a phospholipid membrane and the antibodies used for labeling in this study attached to it.*

method, which avoids direct chemical modifications, is desirable. Elaborate extraction of the proteins and resuspension after labeling could strongly influence the sample and change its binding behaviour. Furthermore, directly labeled proteins tend to aggregate and hence disturb the performance of FCS experiments. To use a labeling method, which meets the criteria listed above, FVIII was labeled via fluorescently labeled antibodies. Antibodies are fluorescently labeled and added to a solution containing FVIII. They bind to FVIII and thereby fluorescently label the protein (Fig. 7.3). This method reduced aggregation of FVIII and allowed for indirect, easy labeling. Moreover, possible functional sites of the protein, which are involved in binding, can be explored by antibody mapping, which employs different antibodies that each bind specifically to one sequence of a certain domain of the protein. Antibodies, which inhibit binding, bind to possible candidates of the binding site of the protein.

Antibodies were fluorescently labeled with Alexa 488 using an antibody-labeling kit (Invitrogen). After labeling, the antibody-solution contained a huge amount of free dye molecules and a non-negligible number of aggregates. Aggregates were filtered out with a membrane-spin column (Vivaspin 500, Sartorius). Free dye was eliminated by centrifugation in a Bio-spin column (Bio-Spin 30, Bio-Rad). After this purification process, a control experiment with FCS was performed to check whether any free dye or aggregates were left. In the case of the detection of any impurities in the sample, purification with the respective columns was repeated. After successful labeling, antibodies were used at a concentration of approximately 10 nM as fluorescent markers for FVIII. Various

antibodies binding to different sites of the FVIII molecule were tested (Fig. 7.3(d)) and for each experiment the most appropriate one was chosen. ESH4, for example inhibits binding of FVIII to PS-membranes, since it binds to the membrane binding site of FVIII. Hence, it could not be applied for measurements on this binding.

7.1.4 FVIII interaction with phospholipid membranes

Formation of the tenase-complex can only occur when activated FVIII is bound to the phospholipid membrane of platelets. Consequently, binding of (activated) FVIII to phospholipid membranes is a key process of blood coagulation. Studies employing resonance energy transfer techniques have shown that negatively charged phosphatidylserine (PS) is required for binding with a minimum amount of three PS-molecules per bound FVIII molecule [6]. For the binding mechanism of inactivated FVIII a two-step process was suggested consisting of a first rapid binding process, which is mediated by electrostatic interaction and represents the main regulatory step of FVIII binding, and a second slower binding step, the mechanism of which was suggested to be insertion of hydrophobic protein domains into the membrane [32]. These findings were confirmed by electron crystallography studies on the 3D-structure of membrane-bound FVIII, which is shown in Fig. 7.2(b) [31]. According to these studies the height of the protein above the membrane is 9.5 nm. Part of the C2-domain is buried into the lipid bilayer (up to 1 nm in depth) and the overall C2 binding area covers 7 -10 nm^2 . The C2-domain exhibits 4 hydrophobic loops inserted into the membrane and 3 lysine residues, which are close enough to the membrane for electrostatic interaction with the charged PS-lipids. Hence, the first step of binding could be mediated via electrostatic interaction of the lysine residues and the charged lipids and the second step via insertion of the hydrophobic loops. In this thesis FCS was used to further elucidate the protein-membrane interaction of FVIII and to investigate the binding of FVIII to PS-containing vesicles as model membranes. FVIII was labeled via fluorescent ESH2 antibodies, which bind to the C2-domain of FVIII without obstructing its capability to bind to PS-containing membranes [66], as described in the previous paragraph. Likewise ESH8 and C7F7 could be used, which bind to the C2- and A3-domain, respectively and were tested to yield the same results. Since the large unilamellar vesicles (100 nm in size) used were sufficiently large to allow for discrimination of the diffusion times of bound and unbound FVIII, binding was measured with FCS employing the method layed out in chapter 4.2. The fraction of bound proteins was extracted from the measured correlation function with appropriate fits as described in chapter 4.2. Titration experiments yielded the fraction of bound protein as a function of the lipid concentration (see Fig. 7.4). These isotherms were recorded for lipid compositions with varying amount of PS. In each case S-shaped binding isotherms were found, which were described by equation 5.18 with a PS-dependent molar partition coefficient $K(PS)$:

$$f_{bound} = \frac{K(PS) \cdot L}{1 + K(PS) \cdot L} \quad (7.1)$$

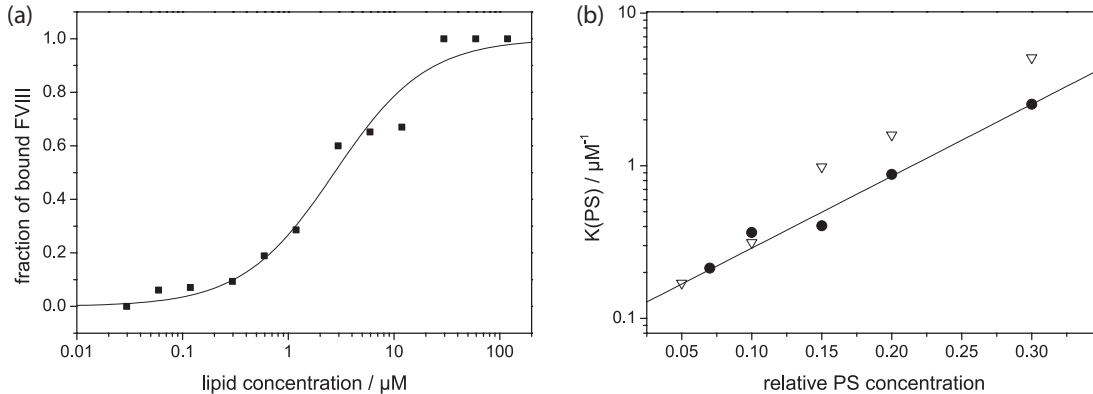


Figure 7.4: *FVIII binding to PS-containing membranes. (a) Binding isotherm obtained from a titration experiment on FVIII binding to vesicles of 10% PS-content. (b) Molar partition coefficient of FVIII binding to vesicles as a function of their PS-content. The measured data (●) are in excellent agreement with the data of Gilbert et al. (▽) [6]. The line represents an exponential fit.*

where L is the molar lipid concentration in solution. The molar partition coefficient $K(\text{PS})$ describes the distribution of free and bound FVIII and hence its binding affinity or binding constant to the lipid membrane. Naturally $K(\text{PS})$ is a function of the relative PS-content of the membrane. The dependence of FVIII binding to membranes on their PS-content is plotted on a semi-log scale in Fig. 7.4. The molar partition coefficient increases with increasing strength of binding, showing that FVIII binding increases continuously with increasing PS-content of the membrane. The line represents a fit indicating an exponential increase within the range of PS-contents studied. This exponential increase of FVIII binding to membranes with increasing PS-content (i.e. charge of the membrane) can be explained in terms of electrostatic interaction. In a first simplified model one can assume that electrostatic binding energy is proportional to charge and the binding energy is proportional to the logarithm of the molar partition coefficient. Thus the molar partition coefficient should increase exponentially with charge. More elaborate theoretical models on electrostatic membrane interactions involving Poisson-Boltzmann theory, also predict an exponential dependence of electrostatic binding on the charge of the membrane [28, 67]. Hence, these findings confirm the assumption of a binding mechanism based on electrostatic interaction of FVIII and PS-containing membranes, as suggested from the experiments by Bardelle et al. [32] and Stoylova-McPhie et al. [31]. Comparison of the results with molar partition coefficients calculated from the data of Gilbert et al. shows very good agreement (Fig. 7.4) [6]. This consistency also serves as a proof for the excellent ability of FCS to measure binding of such systems. Furthermore, the data for membranes with a physiological PS-content of about 10% compare very well with data obtained for binding to platelets [68], which shows that the PS-membranes are good model systems for platelets.

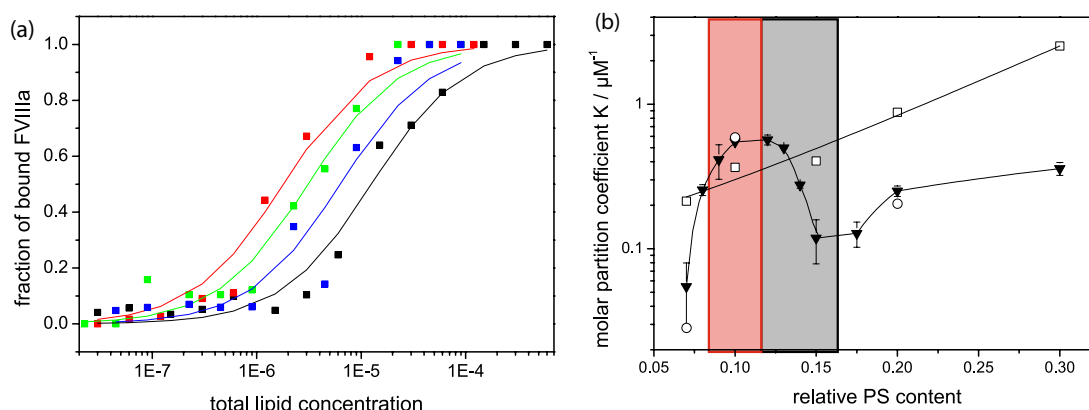


Figure 7.5: Binding isotherms of FVIIIa binding to vesicles at different PS-content (black 7%, red 10%, blue 15%, green 30%). The best binding can be observed at 10%. (b) The molar partition coefficient of activated FVIII binding to membranes (\blacktriangledown) peaks at around 12% relative PS-content and is very sensitive to the PS-content around the physiological PS-content of about 10% PS (marked in red) and at PS-concentrations between 12 and 15% (marked in grey). In contrast, the molar partition coefficient of inactivated FVIII (\square) increases continuously with increasing membrane PS-content. The anomaly in FVIIIa binding is measured using ESH2 (\blacktriangledown) as well as ESH8 (\circ) as label

7.2 Activated FVIII interaction with phospholipid membranes

So far, studies on the binding of FVIII to membranes were focussed on inactivated FVIII. Little is known on the mechanism of activated FVIII binding to membranes. However, in blood coagulation, binding of activated FVIII to membranes is crucial for the formation of the tenase-complex, since inactivated FVIII is not able to react with FIX and to trigger further downstream events in the cascade. Therefore, FVIII was activated by incubation with human thrombin at 37 °C for 30 min prior to the experiments and its binding to membranes was investigated here. To gain further insight into the binding mechanism of FVIIIa to membranes, the molar partition coefficient was measured as a function of the relative PS-content of the membrane yielding for the first time the full PS-dependence of FVIIIa binding to phospholipid membranes. Binding experiments were carried out using the FCS-method, which proved to yield reliable results for inactivated FVIII binding to membranes. Again, S-shaped binding isotherms were obtained from titration measurements (Fig. 7.5(a)), which were described by equation 7.1. The measured molar partition coefficient $K(\text{PS})$ as a function of the PS-concentration is shown in Fig. 7.5(b). Whereas binding of inactivated FVIII to membranes increases continuously with increasing PS-content of the membrane, binding of activated FVIII deviates remarkably from this behaviour. Fig. 7.5(b) shows a strongly peaked dependence of

FVIIIa binding on the PS-content of the membrane. The binding sharply increases up to $K(\text{PS})=0.6\mu\text{M}^{-1}$ at a relative PS-concentration of 12%, which exceeds the binding of non-activated FVIII by 100%. Surprisingly, beyond this point, the binding constant of activated FVIII decreases again and reaches a minimum at about 17% PS-content. This behaviour must be considered anomalous, since the general understanding requires at least the electrostatic interaction to increase with PS-content. To exclude any influences of the antibody labeling, which could induce conformational changes of the protein or change its binding behaviour via other interaction pathways and thereby lead to such an anomalous binding behaviour, experiments were repeated with different antibodies. First, ESH2 was replaced by fluorescently labeled ESH8, an antibody which binds to a sequence on the C2-domain (in this case the van Willebrand factor binding site) different from that of ESH2. Fig. 7.5(b) shows, that both ESH2 and ESH8 lead to the same remarkable anomaly in binding to PS-membranes. As a negative control, experiments using fluorescently labeled ESH4 were performed. ESH4 is known to bind to the membrane binding site on the C2-domain of FVIII and thus inhibits FVIII binding to membranes (see Fig. 7.3(d)). Indeed, when ESH4 was used as label, no binding to membranes could be detected, neither of inactivated nor of activated FVIII. Based on these negative and positive control experiments one can conclude that the anomalous PS-dependence of FVIIIa binding to membranes is not induced by the antibody labeling. Interestingly, a fourth antibody, named C7F7, which binds to the A3-domain of FVIII, did not obstruct the capability of inactivated FVIII to bind to PS-containing membranes, whereas it inhibited binding of activated FVIII to membranes completely. This inhibition behaviour might be explained by a conformational change or sterical hindrance upon binding of C7F7 to FVIIIa, which does not occur, when it binds to inactivated FVIII. The origin of the anomalous binding behaviour is not yet fully understood. Upon activation by thrombin, the B-domain of FVIII is removed and the protein undergoes conformational changes. Considering the change in inhibition behavior of C7F7 upon activation of FVIII, these conformational changes could be believed to induce the enhanced affinity of FVIIIa to membranes of about 12% PS-content.

It is remarkable that the anomaly of FVIIIa binding to membranes falls into the physiological range of PS-content of platelets. In fact, comparing the molar partition coefficients of inactivated and activated FVIII we find that activated FVIII shows weaker binding than inactivated FVIII over most of the PS-content range, except for the narrow region of the peak between 9 and 13%. The finding, that compared to inactivated FVIII, FVIIIa binds stronger in the physiological range is consistent with results obtained for binding to platelets [29]. The observed anomaly of the PS-dependence of FVIIIa binding to membranes, however, has not been reported before. The enhancement of binding upon the activation of FVIII around physiological conditions and the reduction of binding upon FVIII activation at PS-concentrations lower or higher than those under physiological conditions is important since it allows for selective enhancement of FVIII binding, and thus, cascade amplification in case of injury. Another consequence of this finding is reduced binding and coagulation in the absence of an injury representing a

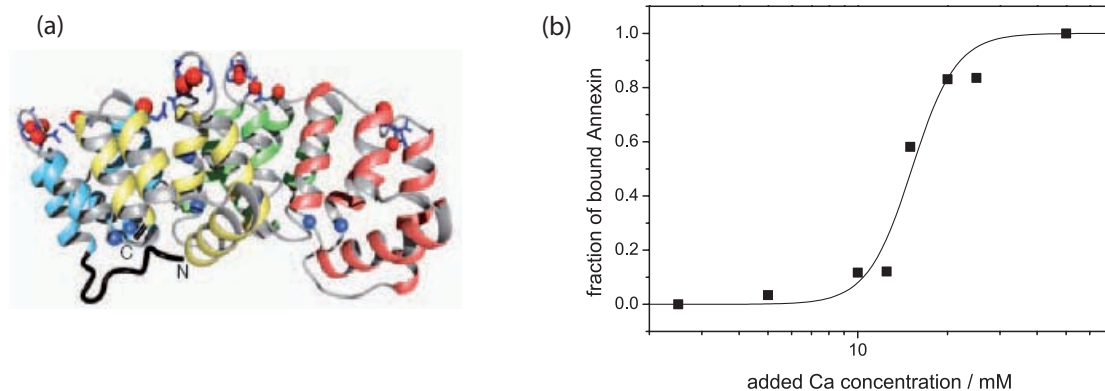


Figure 7.6: (a) Structure of annexin [69]. The top side attaches to the membrane upon binding. (b) Fraction of annexin bound to vesicles containing 10% PS as a function of the calcium concentration at constant lipid concentration of $15\mu\text{M}$.

method of thrombosis prevention, since PS is expressed only in the case of an injury, otherwise the membranes do not contain PS, except for the case of apoptosis, where much more PS is exhibited as compared to the concentration on injured endothel.

The sharply peaked anomaly leads to a tremendous sensitivity of FVIIIa binding to membranes on slight changes of their PS-content in the region of the peak. Since the physiological PS-concentrations can be found on the slope of the peak, variations of the PS-content of platelets have a strong impact on coagulation. This fact provides a basis for very efficient regulation of the coagulation cascade via the membrane charges. The sensitivity of coagulation on the PS-content of the membranes might be very important for diseases and their treatment. On the one hand, a dysfunction in the expression of PS leading to enhanced or reduced PS-concentrations has immediate effects on coagulation. On the other hand, coagulation can be regulated via the membrane charges mediated e.g. by PS-binding cofactors, which might allow for treatment of certain coagulation diseases.

7.3 Regulation of activated FVIII binding to phospholipid membranes by annexin V

7.3.1 Annexin V binding to phospholipid membranes

In the human circulatory system, binding of FVIII to platelets is influenced by many cofactors. One important cofactor is annexin V, a protein that binds to PS-containing membranes in a calcium-dependent manner [36,69,70]. Fig. 7.6(b) shows the strong dependence of annexin binding to membranes on the calcium concentration of the solution, measured in this thesis. The fraction of bound annexin determined in an FCS-experiment

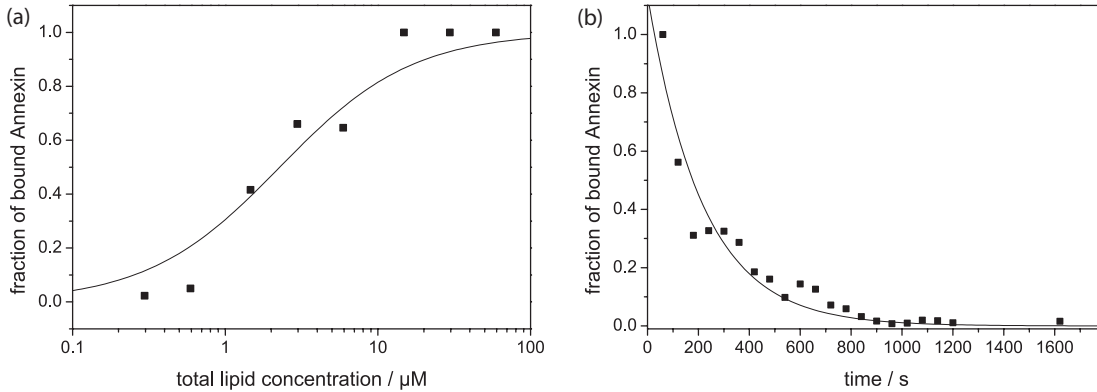


Figure 7.7: (a) Binding isotherm of annexin V binding to vesicles of 10% PS-content. (b) Dissociation of annexin binding to vesicles of 10% PS-content upon addition of unlabeled annexin in excess. The line represents an exponential fit.

with labeled annexin V increases with increasing calcium concentration leading to an S-shaped curve. Tait et al. [71] investigated this behaviour in detail and found cooperative effects. FCS experiments on fluorescently labeled annexin allowed for the measurement of binding isotherms and the determination of molar partition coefficients at various calcium concentrations. An example of such a binding isotherm obtained for 34 nM annexin in 50 mM citrate buffer upon addition of 50 mM calcium is shown in Fig. 7.7 (a). At this calcium concentration the resulting molar partition coefficient was $0.5 \mu\text{M}^{-1}$. Time resolved FCS measurements upon addition of excess unlabeled annexin to labeled annexin binding in equilibrium allowed for the determination of the dissociation rate as described in chapter 5.2. Fig. 7.7(b) shows the resulting curve yielding a dissociation rate of 4.6 ms^{-1} . The association rate is too fast to be resolved by FCS experiments. However, knowing dissociation rate and molar partition coefficient it can be calculated using equation 5.29 to be $2.3 \text{ mM}^{-1}\text{s}^{-1}$. Assuming a diffusion limited association rate and the vesicles to be black binders (i.e. each annexin molecule meeting a vesicle faces only free binding sites; occupied binding sites do not exist), the association rate can be estimated [27]:

$$k_{ass} = \frac{4\pi Da}{N} \quad (7.2)$$

where D is the diffusion coefficient of annexin, a the radius of the vesicles and N the number of binding sites per vesicle. The radius of the vesicles is known to be 45 nm, the diffusion coefficient of annexin was determined in a separate FCS experiment on annexin in buffer to be $70 \mu\text{m}^2\text{s}^{-1}$. Measurements of the number of particles in the focal volume at various fractions of bound annexin yield a rough estimate of the number of binding sites per vesicle N , in this case $N=15$. Based on these values, the association rate in the diffusion limit was calculated with equation 7.2 to be $1.6 \text{ nM}^{-1}\text{s}^{-1}$. Note that this is the association rate in terms of vesicles and to obtain the rate in terms of lipids, it

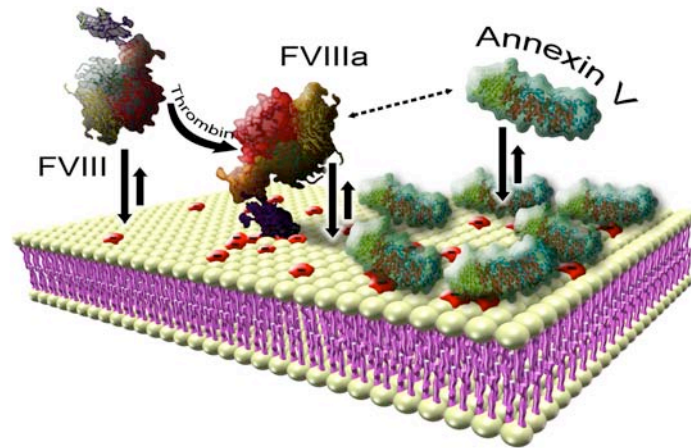


Figure 7.8: Scenario of FVIII, which is activated by thrombin, binding to a phospholipid membrane and the regulatory influence of annexin V on it. This is the part of blood coagulation, which was focus of this study.

has to be divided by the number of lipids per vesicle $n=120000$, yielding a rate of $13 \text{ mM}^{-1}\text{s}^{-1}$. Considering the simplicity of this model, the estimated association rate is in very good agreement with that calculated from the dissociation rate and the molar partition coefficient. Hence, one can assume the association of annexin to be a diffusion limited process as suggested by [72].

Due to its ability to bind to PS-containing membranes, annexin V could act as a regulatory protein for FVIIIa binding to membranes. Indeed, annexin was shown to play a role in coagulation through binding to endothelial cells leading to immediate consequences on thrombin formation [73]. It was reported that antiphospholipid antibodies inhibit annexin V binding to phospholipids, accelerating plasma coagulation [74]. Furthermore, an inhibitory effect of annexin V on FVIII binding to platelets was found, which seems to be specific to activated FVIIIa and not significant for inactivated FVIII [68]. Many additional evidences for the anticoagulant effect of annexin V have been reported [70]. The mechanism of the anticoagulant effect still remains not well understood [70]. It was proposed that formation of a two-dimensional annexin V crystal lattice leads to a reduction of lateral movement of membrane-bound coagulation factors and hence a reduction of the kinetic rates in the membrane-based coagulation pathway [75]. Alternatively, annexin is supposed to compete with coagulation factors for binding sites on the platelet membrane, thereby inhibiting their membrane based interaction as schematically depicted in Fig. 7.8. The following sections present investigations, which contribute to a better understanding of this mechanism of the effect of annexin on coagulation.

7.3.2 Annexin V regulates FVIII binding to phospholipid membranes

To study the effect of annexin V on the binding of FVIII to membranes the vesicles were incubated with annexin V prior to the binding experiments with FVIII. In the case of non-activated FVIII annexin V had a weak but by trend decreasing influence on the binding. In contrast, binding of FVIIIa was strongly influenced even at concentrations as low as $4 \mu M$ of annexin. In fact, the full binding diagram as a function of both PS-content and annexin concentration revealed a complex behaviour as shown in Fig. 7.9(a). It is found that addition of annexin can both reduce as well as increase the binding of FVIIIa depending on the PS-content of the membrane. The binding of FVIIIa to vesicles containing 10% PS is continuously reduced by increasing annexin concentration up to full inhibition (Fig. 7.9(b)). When vesicles of a relative PS-content of 15% were used, the results deviated from these inhibition characteristics. Here, preincubation of the vesicles with annexin enhances binding up to a maximum value. At concentrations higher than this maximum, a reduction of FVIIIa binding to the vesicles is observed again (Fig. 7.9(c)).

Ahmad et al. have shown by binding experiments of FVIII and FVIIIa on activated platelets, that annexin V inhibits binding of FVIIIa but has no significant influence on the binding of FVIII in the absence of other cofactors. This finding is in good agreement with the results presented here for the binding to membranes containing a physiological concentration of 10% PS, where a continuously decreasing binding was measured with increasing annexin V concentration.

To understand the full inhibition behaviour of annexin V, an extended inhibition model was developed, which describes the unusual binding characteristics as found for annexin and FVIIIa binding to phospholipid membranes. The ordinary model of competitive inhibition, which is usually used to describe the interaction of two species, both binding to a third species, assumes a competition for binding sites. This competition for free binding sites is based on mass action and the key parameter is the absolute number of free binding sites. In the scenario of this study, binding of annexin reduces the absolute number of available binding sites for FVIIIa leading to an effectively reduced lipid concentration, $L_{eff}(A) = L - L_A$ with L being the total number of lipids and L_A the number of lipids occupied by annexin. Under the assumption that annexin binds much stronger to membranes than FVIIIa, L_A can be calculated for each annexin concentration with equation 5.17 knowing the binding constant of annexin from a separate experiment. Plugging $L_{eff}(A)$ into equation 5.18 instead of L yields the fraction bound of FVIII for competitive inhibition:

$$f_{bound} = \frac{K \cdot L_{eff}(A)}{1 + K \cdot L_{eff}(A)} \quad (7.3)$$

This model, however, fails to describe the strong inhibition measured for membranes of 10% PS content quantitatively as seen in Fig. 7.9(b), where the blue dashed line represents a fit according to the model of competitive inhibition. Furthermore, it can

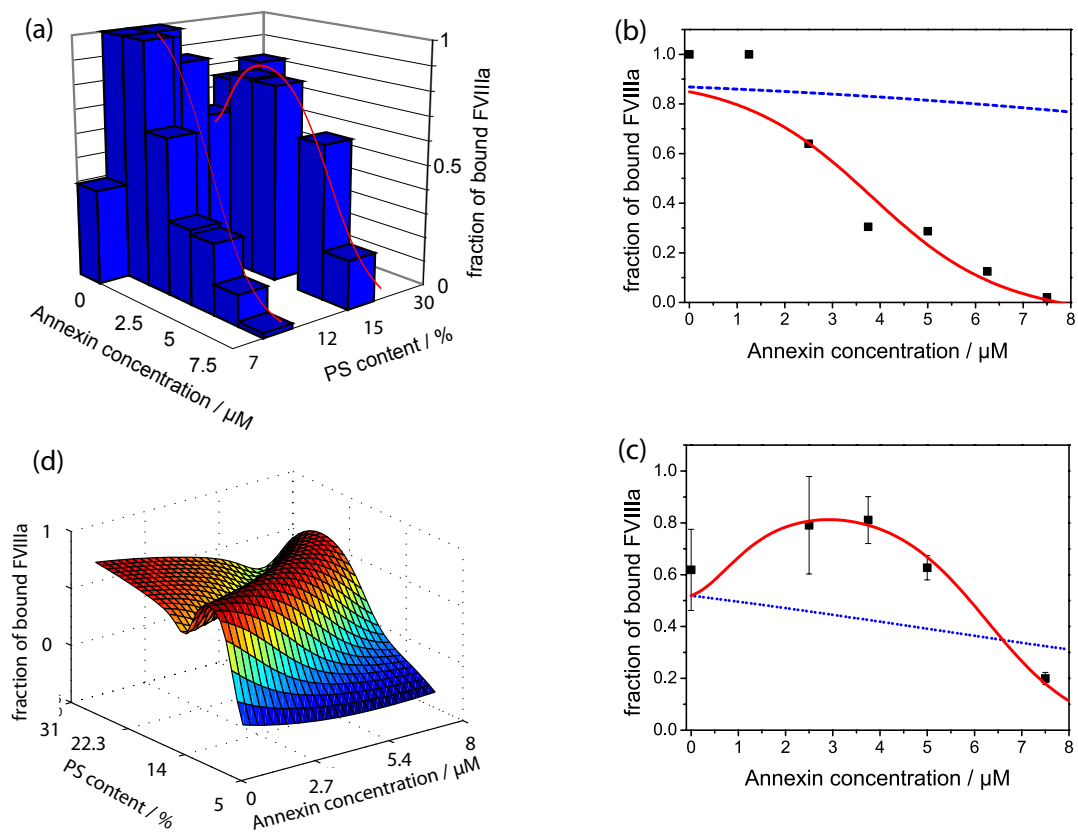


Figure 7.9: (a) 3D-plot of the measured fraction of membrane-bound FVIIIa as a function of PS-content and annexin V concentration. Influence of annexin V on FVIIIa binding to PS membranes at a PS-content of 10% (b) and 15% (c). The blue dashed lines indicate a fit according to competitive inhibition behavior, while the red full lines represent a fit describing the shielding model. (d) Three-dimensional plot showing shielding model simulations of the PS-content and annexin concentration dependence of FVIIIa binding to membranes at a constant lipid concentration. Note the change of axes as compared to (a). The red lines in (a) can be found following the corresponding black lines in (d) parallel to the annexin concentration axis.

only explain the decrease in binding, but not the enhanced binding that was found for membranes with 15% PS content (see Fig. 7.9(c)). Therefore, the competitive inhibition model was extended based on the fact that annexin specifically binds to PS and modifies the relative PS concentration and hence the binding constant $K(\text{PS})$ by effective "shielding" of the PS-content. The resulting effective PS content was assumed to be described by $PS_{eff}(A) = PS_0 \cdot (1 - \alpha A_b)$, where the amount of bound annexin A_b can be derived explicitly with equation 5.17 knowing the binding constant of annexin from a separate experiment. Here, the molar shielding efficiency, α , was introduced to quantify the efficiency of the reduction of the relative PS-content per mole annexin. A shielding efficiency of $\alpha = 0.1 \mu\text{M}^{-1}$ for instance implies that $1 \mu\text{M}$ annexin reduces the relative PS-content by 10%. Due to the unusual sensitivity of FVIIIa binding to the PS-content of membranes, as described above, a reduction of the relative PS-content induces dramatic changes of the binding constant $K(\text{PS})$ causing both enhanced or reduced binding of FVIIIa. A quantitative description of the fraction of bound FVIIIa as a function of annexin concentration is given by:

$$f_{bound}(PS, A) = \frac{K(PS_{eff}(A)) \cdot L_{eff}(A)}{1 + K(PS_{eff}(A)) \cdot L_{eff}(A)} \quad (7.4)$$

Note that equation 7.4 contains only one unknown parameter, since $K(\text{PS})$ can be extracted from the measured data by a phenomenological fit and the amount of annexin can be determined with equation 5.17 using a binding constant obtained in a separate experiment. Hence, the only unknown parameter is the shielding efficiency α . Equation 7.4 describes the measured dependence of the fraction of bound FVIIIa on the annexin concentration with very good agreement as shown by the full lines in Fig. 7.9(b) and (c). Due to the fact that only one adjustable parameter, the shielding efficiency α , entered the model, it is very remarkable, that both data sets, for 10% as well as 15% PS are equally well described. To further elaborate the full phase diagram of the binding behaviour, the theoretical landscape of binding as a function of PS and annexin concentration at a constant lipid concentration is plotted in Fig. 7.9(d). The anomaly of the PS-dependence of FVIIIa binding to membranes allows for inhibition and enhancement of binding, which occurs upon reduction of the effective PS-content through the addition of annexin. The shielding model is thus able to qualitatively and quantitatively explain the mechanism of interaction of annexin and FVIIIa binding to membranes.

A key component of the inhibition model is the assumption that there is no direct interaction between annexin and FVIIIa. All interference of annexin occurs indirectly via shielding PS and hence modulation of the binding affinity of the membrane to FVIIIa. In order to test this hypothesis dual color cross-correlation experiments were performed on supported membranes as schematically depicted in Fig. 7.10(a). In this experiment FVIIIa is labeled with green fluorescent antibody while annexin is labeled with a red fluorescent dye. A proof of principle of such experiments on supported lipid bilayers is presented in chapter 12 on the example of DNA diffusion on lipid membranes. Here, fluorescence cross-correlation spectroscopy was used to distinguish single proteins from

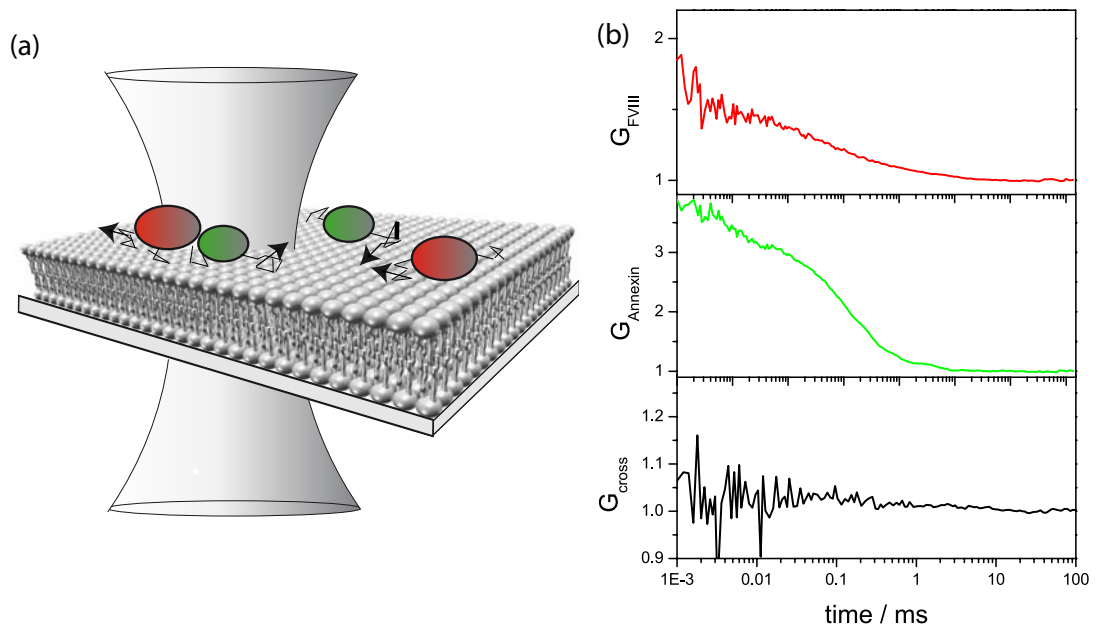


Figure 7.10: (a) Schematic view of FCS measurements of FVIIIa and annexin V diffusion on a supported lipid bilayer (b) Autocorrelation curves of activated FVIII (red) and annexin (green) on a supported lipid bilayer. No cross-correlation (black) between annexin and activated FVIII can be detected, indicating the absence of direct interaction between these. The diffusion coefficient of activated FVIII is not influenced by annexin and is measured to be approximately $10\mu\text{m}^2\text{s}^{-1}$ for both.

correlated protein clusters. Distinct autocorrelation curves are obtained for both, annexin as well as FVIIIa, yielding a diffusion coefficient of about $10\mu\text{m}^2\text{s}^{-1}$ for both proteins, which is approximately equal to the diffusion coefficient of lipids in the membrane (Fig. 7.10(b)). Yet, the cross-correlation shows a flat time dependence indicating that there is no correlated diffusion of annexin and FVIIIa. Comparison with the diffusion coefficients of each protein moving on membranes in the presence and absence of the other indicated that the diffusion of one is not influenced by the other.

The results of the cross-correlation studies verify the assumptions of the shielding model. Hence, all findings presented in this chapter support the suggestion that shielding of charges, which reduces the effective charge of the membrane for FVIIIa is the mechanism how annexin V is involved in blood coagulation. A comparison of the quantitative fits from the shielding model with those from competitive inhibition (full red and dashed blue lines, respectively in Fig. 7.9(b) and (c)) demonstrates the efficiency of the shielding mechanism in annexin-mediated regulation of FVIIIa binding even under conditions where there are excess lipids, as the case was in the experiments presented here. In contrast, competitive inhibition hardly shows any significant effect. The full three-dimensional phase diagram calculated on the basis of the shielding model shows that the shielding mechanism is able to explain the anticoagulant effect of annexin under non-pathological conditions, and indicates a possible procoagulant effect for platelets overexpressing PS to levels exceeding 12%. Based on the strong effect of annexin on coagulation, it has a great potential as a coagulation regulating drug.

7.4 Experiments in blood plasma

To see, if the experimental results of this chapter are valid under in vivo conditions, the experiments were repeated in FVIII deficient blood plasma. Plasma is a strongly scattering, crowded medium, which poses an experimental hurdle to FCS measurements that needs to be considered in the analysis as explained in detail in chapter 6 [38]. Taking these effects into account, allowed for the measurement of FVIII binding to vesicles in plasma. The first satisfying finding is that the molar partition coefficients of FVIII and FVIIIa binding to vesicles in plasma in the absence of annexin are consistent with those obtained in buffer solution. Secondly, preincubation of the membranes with annexin V in plasma leads to the same characteristic enhancement and inhibition behaviour as observed in buffer. Surprisingly, however, the absolute concentrations of annexin necessary to reach the same level of inhibition differ in plasma and buffer by about a factor of 4. This is demonstrated by rescaling the theoretical prediction for the data in buffer (solid line) by a factor of 4 (dashed line) in Fig. 7.11. This enhancement of the effect of annexin on FVIIIa binding in plasma could be explained by the influence of other cofactors, such as Factor IX. Ahmad et al. [68] reported an enhanced effect of annexin on FVIIIa binding to platelets in the presence of EGR-FIXa and FX, which supports the suggestion of an enhancement due to the influence of other cofactors. These findings

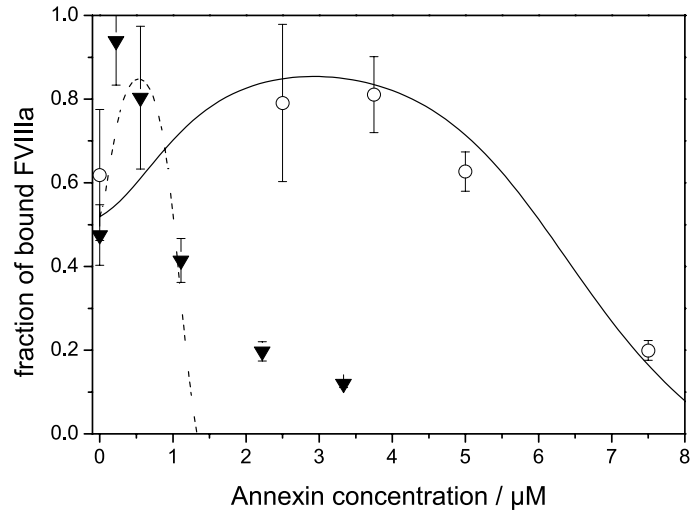


Figure 7.11: Regulation of FVIIIa binding to a membrane of 15% PS-content by annexin in buffer (\circ) and in plasma (\blacktriangledown). The full line represents a fit according to the shielding model, the dashed line is the same curve rescaled by a factor of 4 in the x -axis.

emphasize the importance of measurements under biological conditions for investigating processes as complex as this and encourage to further investigate these effects in both, buffer and plasma. Since FCS allows for binding measurements in both, buffer and plasma, it provides a powerful tool in research and diagnostics.

8 Binding of coagulation proteins to PEGylated vesicles

The previous chapter dealt with specific binding of coagulation proteins, namely FVIII and annexin to membranes. Here, their unspecific binding to PEGylated vesicles is investigated. This chapter introduces PEGylated vesicles as promising drug delivery systems and describes the equilibrium binding constants as well as kinetic aspects of annexin V binding to PEGylated vesicles.

8.1 PEGylated vesicles as drug delivery systems

Liposomes show a vast potential as drug delivery systems. Encapsulation of drugs into liposomes allows them to act as carriers, which efficiently deliver drugs. They are taken up by cells, e.g. by endocytosis or vesicle fusion and hence are able to directly deposit their drug load into the cell [76]. Composed of a lipid bilayer they are biocompatible and do not bear any hazards to the body, since their construction is inspired by nature, particularly, the cell membrane. Their size and the dose of drug load can be tuned and the lipid bilayer can be functionalized. Functionalization with proteins such as EGF, for instance, allows for specific targeting to cells expressing the corresponding receptors. However, one demanding challenge for the use of liposomes as drug delivery systems remains their fairly short circulation time. Once they entered the circulation they are recognized as foreign bodies by the immune system and quickly cleared away. Their recognition and clearance is believed to be the result of fast opsonization of the liposomes by blood proteins [77]. To this end, polymer-coated liposomes provide a solution. Their circulation time has been shown to be tremendously prolonged as compared to uncoated liposomes [78]. Since the polymer-layer seems to greatly reduce the clearance of the liposomes and since they appear invisible to the immune system of the body, they are also called stealth liposomes. Another name given to them is sterically stabilized liposomes due to the attribution of this effect to steric stabilization. Most approaches to explain the mechanism of this prolongation of the circulation time involve a decreased binding of plasma proteins on the surface of the polymer-coated liposomes [77]. A prominent and very promising representative of such polymer-coated liposomes are PEGylated liposomes. In order to study their interaction with the membrane-binding plasma proteins FVIII and annexin V FCS experiments on equilibrium binding as well as kinetics were performed in this thesis. The investigation of the binding of FVIII to PEGylated

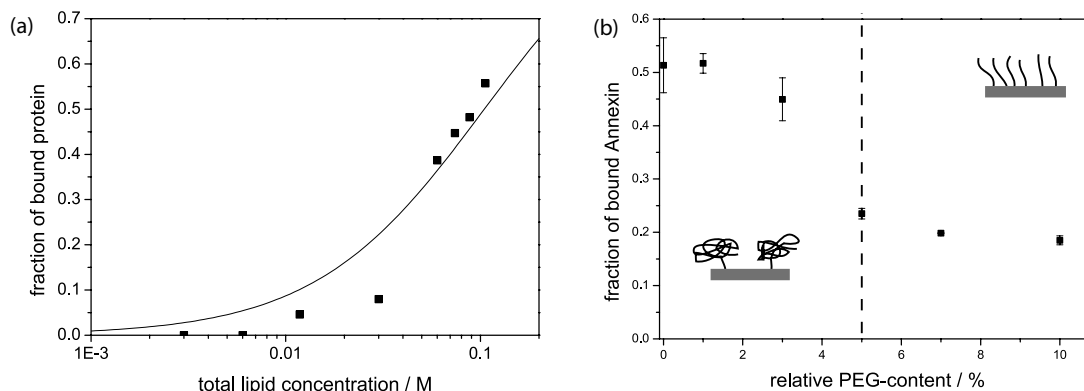


Figure 8.1: *Annexin V binding to PEGylated vesicles. (a) Binding isotherm of annexin upon addition of 50 mM calcium. (b) Fraction of annexin bound to PEGylated vesicles at a lipid concentration of 0.1 M as a function of the PEG-content of the vesicles.*

vesicles is of particular interest to pharmaceutical industry since Baru et al. reported on a prolonged circulation time and haemostatic efficacy of FVIII due to its binding to these vesicles [79]. With this finding in the background the interaction of FVIII with PEGylated vesicles was investigated in this thesis in collaboration with Bayer Health Care and Bayer Technology Services. The results are summarized in an internal report to Bayer.

8.2 Equilibrium binding constants

Titration experiments were carried out for annexin V binding to PEGylated vesicles of 100 nm diameter, which were composed of 97% POPC and 3% DSPE-PEG2000. The resulting binding isotherm is shown in Fig. 8.1(a), revealing weak, unspecific binding. As in the case of specific binding to PS-membranes, annexin V shows no binding without calcium. Upon addition of 50 mM calcium, binding up to a fraction of more than 50% bound annexin V could be measured, which allows for a determination of the binding constant using equation 5.18. The resulting value for the binding constant K is 10 M^{-1} , a factor of 50000 less than binding to vesicles containing 10% PS. Fig. 8.2 illustrates the values of the binding constants compared to those involving PS-membranes of 10% PS content. Binding to PEGylated vesicles is unspecific and orders of magnitude weaker than that to PS-membranes.

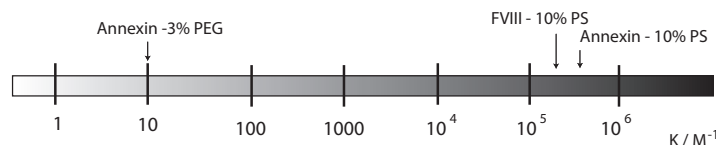


Figure 8.2: Comparison of the molar partition coefficients of annexin and FVIII binding to 10% PS vesicles and of annexin binding to 3% PEG vesicles.

8.3 Effect of PEGylation regime on binding

In order to gain more insight into the influence of the PEG-coating on binding of proteins to stealth liposomes, the fraction of annexin bound to liposomes was recorded for PEG-coatings of varying PEG-concentration. Fig. 8.1(b) shows the fraction of annexin bound to PEGylated liposomes (PEG2000) at a concentration of 0.1 M as a function of their relative PEG-content. The amount of bound annexin shows a fairly flat dependence up to a PEG-content of 5%, where it sharply decreases to a fraction of about 20% bound protein, which again does not change significantly within the range of measured concentrations. The drastic decrease in binding at 5% PEG-content can be explained by the PEG-conformation on the liposome. At PEG-contents below 5%, the polymers are in mushroom conformation, whereas above, they assume brush conformation [80]. In the latter conformation displacement of PEG-molecules by annexin affords more energy than in the mushroom regime, hence, binding of annexin to liposomes coated with PEG-molecules in brush conformation is reduced compared to those with PEG in mushroom conformation. Comparison with a measurement of annexin binding to uncoated POPC-liposomes shows that PEG-coating in the mushroom regime has hardly any effect on annexin binding. From these findings one can conclude, that PEGylation of liposomes at a concentration in the brush-regime prevents the liposomes from opsonization (at least by annexin) and hence could prolong their circulation time.

8.4 Binding kinetics

Experiments on binding kinetics could help to further understand the mechanism of the influence of PEGylation on the binding of proteins to liposomes. Binding of annexin to PEGylated liposomes (3% PEG) was in equilibrium within 10 s. Thus, association rates could not be resolved with FCS. To measure the dissociation rate unlabeled annexin was added in excess to a solution of annexin binding in equilibrium to 0.1 M PEG-liposomes at a fraction of 50%. Interestingly, whereas this method lead to a decrease of binding of annexin to PS-vesicles as shown in Fig. 7.7, in the case of PEGylated vesicles, the fraction of bound annexin did not change at all. Upon addition of EDTA, which chelates calcium and hence inhibits the calcium-mediated binding of annexin [81],

complete inhibition is reached within seconds (i.e. faster than FCS can temporally resolve). These findings might be explained by a reduction of the free energy in addition to the binding energy, which could be due to the displacement of the PEG-molecules. This could lead to a quasi-irreversible binding as observed in the experiments above. Upon disruption of the binding by EDTA, the annexin molecules are trapped only by the polymer-coating and not bound. Thus, they need to cross the energy barrier of the PEG-displacement only, which allows them to detach from the vesicles.

9 Lipid-coated mesoporous nanoparticles as drug delivery system

In chapter 8, the enormous potential of liposomes as drug delivery systems was pointed out. Here, lipid bilayers are used to coat colloidal mesoporous silica nanoparticles (CMS), thereby combining the advantages of liposomal drug delivery, as described in chapter 8 and those of CMS, which allow for various routes of surface functionalization and control over their size at the nanometer length scale. The lipid-coated CMS are characterized using fluorescence cross-correlation spectroscopy which gives evidence of their structure and monodispersity. The lipid bilayer is shown to serve as an intact barrier against the escape of encapsulated molecules with an unsurpassed 100% sealing capacity. As a proof of principle for their ability to deliver and release drugs, the lipid-coated nanoparticles are loaded with the anticancer drug colchicine and efficient uptake by liver cancer cells resulting in cell death by depolymerization of microtubules is observed. Finally, the drug administration assisted by lipid-coated CMS is shown to be specific to intracellular release of colchicine from the nanoparticles and hence enhances the drug efficiency. This enhancement of drug efficiency compared to diluted drugs in solution has immediate consequences on treatments such as chemotherapy, since it allows for delivery of concentrated doses into the cells and a reduction of the overall dosis given to the patient. The project presented in this chapter was done in close collaboration with Valentina Cauda (group of Prof. Dr. T. Bein), who synthesized and characterized the nanoparticles and did most of the in-vitro delivery experiments, Delphine Arcizet (group of Prof. Dr. J. Rädler), who carried out the confocal microscopy experiments on the particles together with myself, and with Anna Sauer (group of Prof. Dr. C. Bräuchle), who performed the in-vivo colchicine delivery experiments.

9.1 Nanoparticles as drug delivery systems

Nanoparticles show a vast potential for medical applications as intelligent drug delivery systems. Furthermore, they can be used as nanoagents for medical imaging and in-situ diagnostics. Mesoporous silica nanoparticles are candidates of particular interest due to their ability to efficiently and specifically encapsulate guest molecules [82]. Their large surface area (between 800 and 1200 m^2/g) and pore volume (about 1 cm^3/g) and their uniform pore diameter (about 4 nm), combined with accessible nanoscale morphologies and high stability in colloidal suspensions [83] all point to their potential

as powerful drug carriers. Moreover, their surface can be functionalized and their size is controllable at the nanometer length scale, hence, they can be perfectly adapted to various conditions of drug delivery. A challenge in the current development, however, is the design of a controlled cap to prevent uncontrolled and premature release of the drug from the mesopores. Efficient molecular pore sealing systems based on large molecules, clusters or molecular assemblies are promising ideas for a solution to that challenge [84–86]. Such a cap system should also fulfill more specific functions, such as a stimuli-responsive delivery, biocompatibility and the option to incorporate specific receptors for cell targeting. One design, which meets these criteria and employs lipid self-assembly, is to coat the mesoporous nanoparticles with supported lipid bilayers, which mimicks a biological cell envelop and offers several advantages [87–89]. First, the membrane manifold prolongs circulation time and enhances accumulation in tumor cells as shown for liposome-based delivery of doxorubicin [90]. Moreover, the high biocompatibility, low toxicity and immunogenicity of the lipid bilayer would allow for future use in cancer therapy. The uptake and specific targeting can be easily improved by attaching specific receptors such as EGF or GE11 to functional groups of the lipids. Finally, compared to liposomes, nanoparticle supported membranes should exhibit more structural stability and a well controlled size distribution [91].

Among the main issues still faced with drug treatment are short circulation times and low target specificity, which both decrease the efficiency of the drug and increase side effects because larger doses are needed. In principle, mesoporous nanoparticles can retain and protect the guest molecules before reaching the target cells, thus minimizing their toxicity and maximizing the drug effectiveness, if an intact lipid bilayer is deposited on the surface. Brinker and coworkers showed that lipid coating of silica can be achieved by fusion with negatively charged liposomes followed by incubation with positively charged liposomes [88]. The protocol yielded 100 nm lipid coated mesoporous nanoparticles capable of retaining 75% of the loaded dye [87]. The encapsulation of even smaller nanoparticles in a lipid bilayer was reported for fluorescent quantum dots of about 50 nm in diameter and silica nanoparticles of 20 nm using reverse-phase evaporation methods [92]. However, in this case, the authors found at least three quantum dots encapsulated inside a single lipid vesicle, due to the difference in size between the quantum dots and the liposomes (300 nm) and the approach used for their incorporation. Hence, the preparation of intact supported bilayers on single mesoporous nanoparticles for long-term encapsulation of a drug load and controlled release after delivery is still a demanding issue.

9.2 Lipid-coating of the nanoparticles

In this project we used a solvent-exchange method to coat single mesoporous silica nanoparticles with a defect-free, intact supported lipid bilayer. The principle of this solvent-exchange method relies on the fact that lipids dissolved in ethanolic solution

prevail as monomers, whereas they self-assemble into solid surface-supported bilayers or liposomes as the water content of the solution is increased toward 100%. Three types of lipid compositions were used for the lipid coatings: 100% DOPC, 100% POPC and a mixture of 30% vol positively charged DOTAP and 70% vol DOPC (Fig. 9.1(d)). Lipids were mixed in chloroform, then desiccated and finally dispersed in a mixture of 60% water and 40% ethanol (Fig. 9.1(a)). Both, the CMS nanoparticles and some of the lipids were labeled with the fluorescent dyes, Atto 647 and Bodipy, respectively, for subsequent characterization and delivery experiments. By suspending the CMS nanoparticles in the lipid solution, a supporting surface is offered for lipid bilayer formation upon water addition to the solvent (up to 95% vol), thus allowing a direct and efficient coverage of the silica surface (Fig. 9.1(c)).

Synthesis of the CMS nanoparticles and their labeling with fluorescent dyes is described in [83,93] and yielded spherically shaped nanoparticles of a size of 50 nm with a worm-like mesoporous structure, as confirmed by Transmission electron microscopy and X-ray diffraction patterns (Fig. 9.2).

9.3 Characterization of the lipid coated nanoparticles

The effective self assembly of the supported lipid bilayers on single CMS nanoparticles was confirmed by several characterization techniques. First, fluorescence cross-correlation spectroscopy is used to prove, that the lipid bilayer is indeed tightly bound to the mesoporous nanoparticle. Fig. 9.3(a) shows the autocorrelation curves of the Atto 647-labeled CMS nanoparticles and the Bodipy-labeled lipid coating. Both curves reveal diffusion characteristics resulting from monodisperse particles of about 60 nm diameter. The results of both channels are in agreement, suggesting colocalization of CMS nanoparticles and lipids. This coupling is further confirmed by analysis of the cross-correlation function, which exhibits a distinct curve. Since contributions of cross-talk are measured to be negligible, this curve is due to correlated movement of the CMS nanoparticles and the lipids. Hence, it demonstrates the successful lipid coating of the CMS nanoparticles.

The colloidal stability of the lipid-coated CMS nanoparticles was confirmed with dynamic light scattering. The results showed that the lipids do not only form a tight bilayer around the nanoparticles but also sterically stabilize the nanoparticles, thereby preventing them from aggregation.

With fluorescence microscopy, Atto 647-labeled nanoparticles (red) and Bodipy-labeled POPC lipids (green) were visualized in separate channels (Fig. 9.3(b)). The optical resolution is of course not high enough to allow for resolution of a single lipid-coated nanoparticle. But it visually shows the colocalization of the two dyes, thus confirming the encapsulation of CMS nanoparticles into the lipid bilayer.

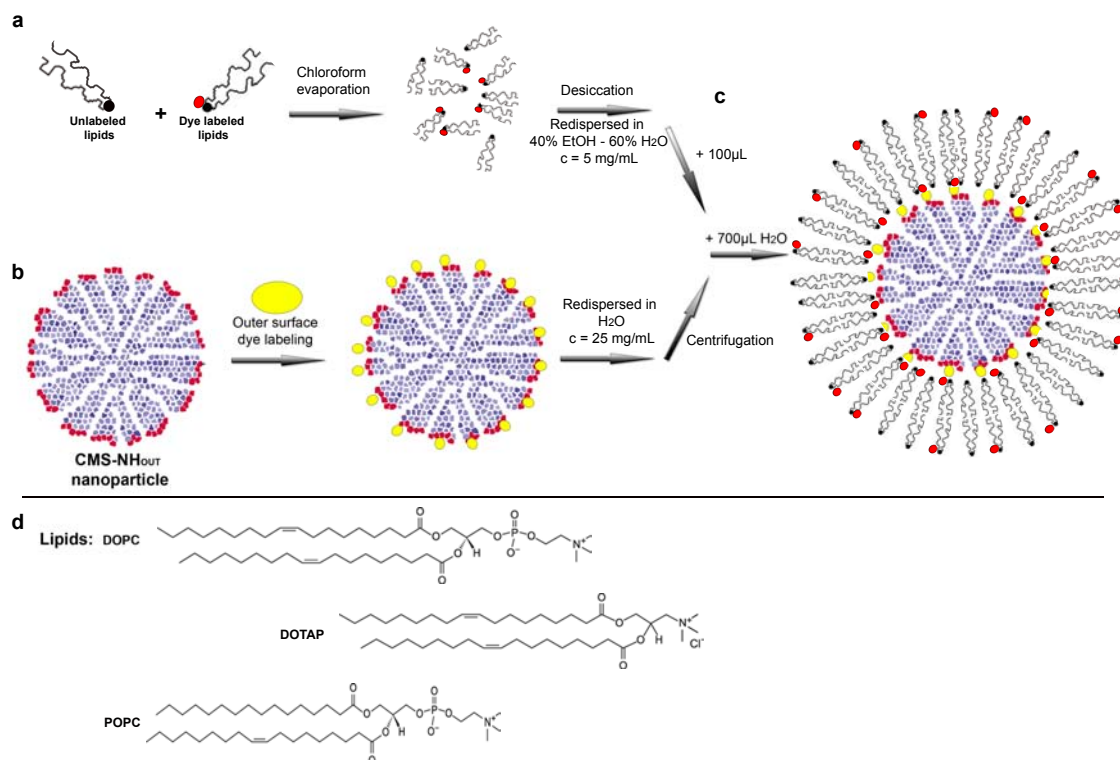


Figure 9.1: Scheme of the synthetic procedure of the formation of supported lipid bilayers on colloidal mesoporous silica nanoparticles (CMS). (a) After the synthesis of outer surface amino-functionalized CMS the amino-propyl groups are fluorescently labeled in water. The labeled particles are then centrifuged. (b) The lipids in chloroform are mixed with dye-labeled lipids. After chloroform evaporation, the mixture of unlabeled and labeled lipids is desiccated and redispersed in a mixture of 40% vol EtOH/60% vol water. (c) The lipid solution is added to the centrifuged dye-labeled CMS nanoparticles. Upon addition of water, the lipid bilayer forms on the surface of the CMS nanoparticles. (d) The three kinds of lipids used: DOPC, POPC and DOTAP (used in a mixture of 30% vol DOTAP and 70% vol DOPC).

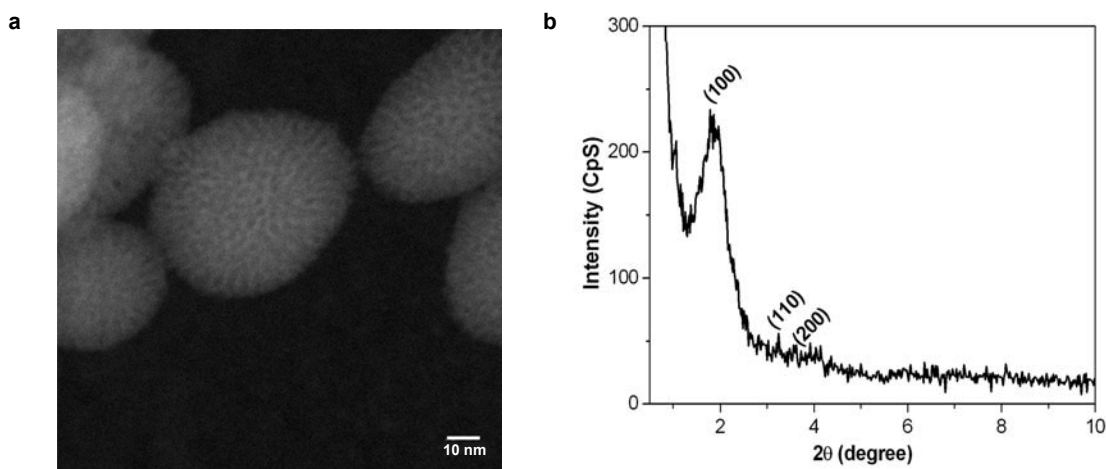


Figure 9.2: Characterization results of the mesoporous silica nanoparticles. Scanning Transmission Electron Microscopy (a) and X-ray diffraction pattern (b) yield the monodispersity and wormlike mesoporous structure of the spherically shaped silica particles as well as their size of 50 nm.

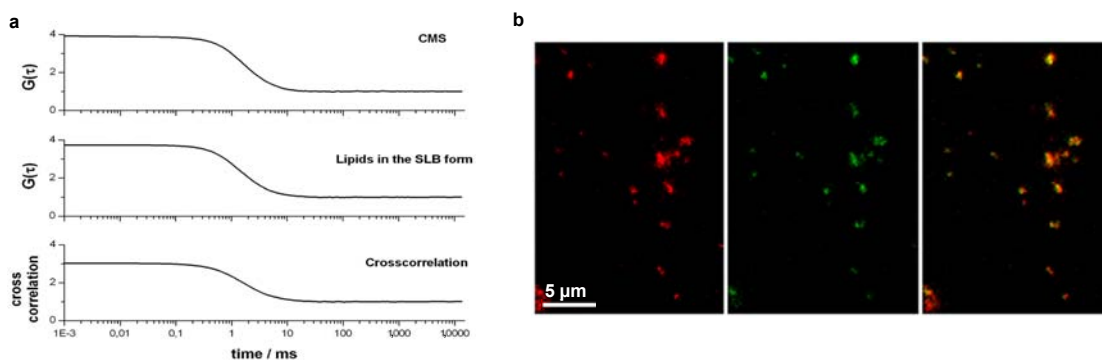


Figure 9.3: Characterization results of the lipid-coated CMS nanoparticles (a) Fluorescence Cross-correlation Spectroscopy of DOTAP/DOPC-coated CMS nanoparticles. The nanoparticles are labeled with Atto 647, the lipids with Bodipy. (b) Fluorescence microscopy image of POPC-coated CMS nanoparticles. Left: Atto 647-labeled CMS (red), middle: Bodipy-labeled POPC lipids (green), right: merged channels (yellow indicates co-localization of CMS and lipids). The results of both, cross-correlation as well as microscopy, confirm the successful assembly of the lipids around the CMS.

9.4 In-vitro release experiments

In-vitro release experiments were performed to demonstrate that the lipid bilayer formed on each CMS nanoparticle is compact and defect-free and that it prevents any premature release of the guest molecules from the mesostructure of the nanoparticles. To this end, fluorescent dyes (fluorescein and calcein, respectively) were encapsulated into the mesopores of the nanoparticles which were then capped with a lipid bilayer. The dye-loaded and membrane-coated nanoparticles were confined in a tube sealed by a dialysis membrane, which is placed on top of a fluorescence cuvette filled with water (Fig. 9.4(b)). The dialysis membrane allows only the dye molecules to enter the cuvette volume. Consequently, the monitored fluorescence emission results only from the released guest molecules. No fluorescence is detected, when successfully coated nanoparticles are measured. For comparison, the release of fluorescein from uncoated CMS nanoparticles is shown in Fig. 9.4(a). While this reference sample exhibits a 100% release of the absorbed guest molecules within 10 minutes, no release can be detected from the lipid-coated nanoparticles. After one hour of monitoring without any increase in the fluorescence emission, a membrane disrupting agent, such as ethanol or the surfactant triton X-100, was added into the tube containing the lipid-coated nanoparticles. The fluorescence intensity shows a rapid increase in intensity due to the prompt release of the dye molecules from the mesoporous particles. The final fluorescence intensity of both, the reference sample and the lysed lipid-coated nanoparticles are similar (Fig. 9.4(b)). The release rate displayed by the lipid-coated nanoparticles after lysis appears slower than that of the uncoated nanoparticles. This effect can be attributed to hindered diffusion due to lysed lipid fragments around the nanoparticles. All three lipid compositions and both guest molecules, fluorescein as well as the larger calcein, yielded similar results. Hence, they all show the unprecedented efficiency in capping the mesopores of the lipid-coating via solvent exchange leading to zero premature release of the absorbed molecules.

9.5 In-vivo delivery and release experiments

The in-vitro experiments prompted the potential use of the lipid-coated CMS nanoparticles as drug delivery system. Here, the in-vivo applicability is tested by visualization of delivery and release of the anti-cancer drug colchicine into HuH7 liver cancer cells [94]. Colchicine binds to tubuline and thus inhibits microtubule polymerization, which leads to cell death. After loading the drug into the CMS mesopores, the nanoparticles were coated with a lipid bilayer consisting of POPC lipids. The supernatant with dissolved colchicine was removed and the drug-loaded coated nanoparticles were redispersed in a cell culture medium. During the incubation of the loaded nanoparticles with cells, delivery of colchicine into the cell interior is expected upon internalization of the lipid-coated nanoparticles or upon contact with the cell membrane. Even though the entry

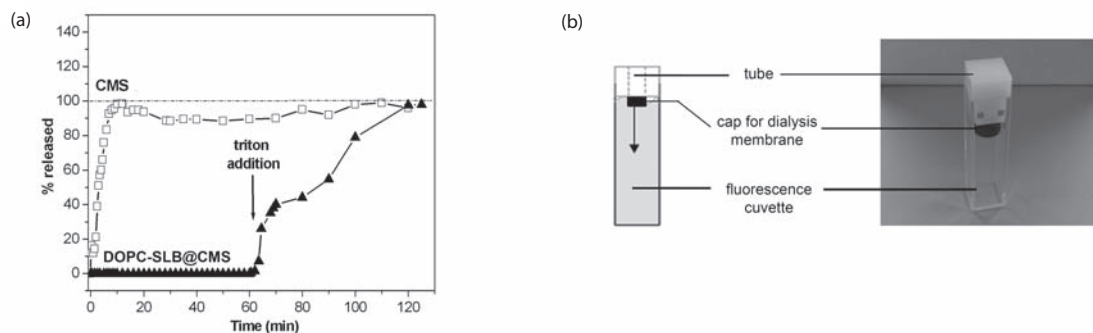


Figure 9.4: *Fluorescein delivery profile from lipid-coated CMS. (a) The uncoated CMS (\square) show a prompt release of fluorescein within 10 min, indicated by the steep increase of released fluorescence. In contrast, no release is detected from the lipid supported nanoparticles (\blacktriangle). Just after Triton addition (at 60 min), a fast release of fluorescein is observed due to lysis of the lipid. (b) Scheme and photo of the fluorescence cuvette used for the release experiments: the sample is confined in the tube and closed by a cap with a dialysis membrane; the volume of the fluorescence cuvette is filled with water.*

mechanism of the coated nanoparticles is not yet clear, one can conclude from the in-vitro experiments, that the colchicine release can take place only upon lysis of the lipid bilayer on the CMS nanoparticle surface.

To see the impact of colchicine-loaded, lipid-coated nanoparticles on cells, high resolution spinning-disk confocal microscopy was performed using two separate detection channels, with the green channel monitoring the GFP-labeled tubulin expressed by the HuH7 cells and the red channel measuring the fluorescence of the Atto 647 labeled CMS nanoparticles.

Fig. 9.5(a) shows untreated HuH7 cells with the GFP-labeled network of microtubules with an insert of colchicine-loaded lipid-coated CMS nanoparticles. HuH7-cells after 25 minutes of incubation of the particles are shown in Fig. 9.5(b). The microtubule network still appears to be intact after this time. In contrast, after 120 min of incubation (Fig. 9.5(c)) the individual microtubule filaments can hardly be recognized. The diffuse green fluorescence arises from the depolymerized microtubules. Fig. 9.5(c) shows the cross section of the same HuH7 cell as displayed in Fig. 9.5(b), where some internalized nanoparticles are visible in the green cell medium. Twentyfour minutes later (at a total time of 144 minutes, Fig. 9.5(d)), the morphology of the same cell has changed considerably: a shrunk and flat cell surface is observed, clearly indicating cell death. This can be attributed to colchicine delivery and release from the lipid-coated nanoparticles, followed by binding of colchicine to tubulin, microtubule depolymerization and cell death.

To prove that the microtubule depolymerization and cell death are caused by the colchicine drug and not by the carrier itself, unloaded lipid-coated CMS nanoparticles were incubated with HuH7 cells. Fig. 9.6(a) shows a living HuH7 cell with an intact

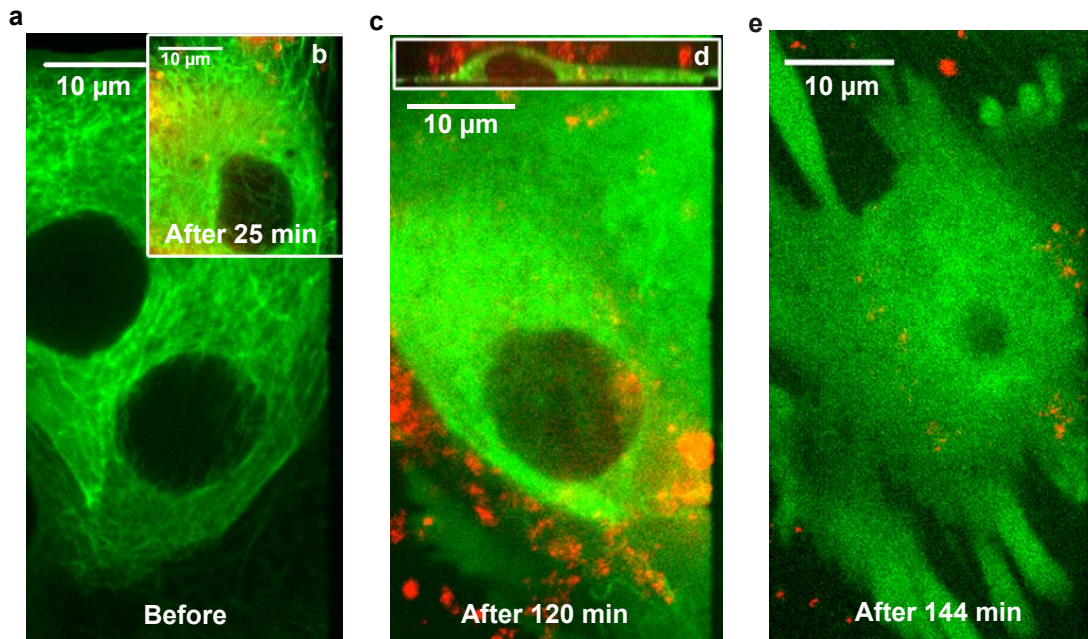


Figure 9.5: Colchicine delivery from the lipid-coated CMS on HuH7 liver cancer cells, stably expressing GFP-labeled tubulin. (a) Untreated HuH7 cells show a GFP-labeled well-structured microtubule network (green). (b) CMS nanoparticles are labeled with Atto 647 (red). Colchicine is adsorbed into the mesopores and then capped with a POPC lipid bilayer. The POPC-coated CMS nanoparticles with colchicine are injected into the culture medium of the liver cancer cells. After 25 min, the nanoparticles have not been internalized. (c) After 120 min the internalized nanoparticles deliver colchicine into the cell. The microtubule network disappears and a diffuse fluorescence due to microtubule depolymerization is observed. (d) Side view of the HuH7 cell represented in Fig. c, where the internalized nanoparticles (in yellow, due to the overlay of green and red colors) are visible. Several other nanoparticles (in red) are on top of the cell. (e) After 144 min the cell morphology is disintegrated, confirming cell death.

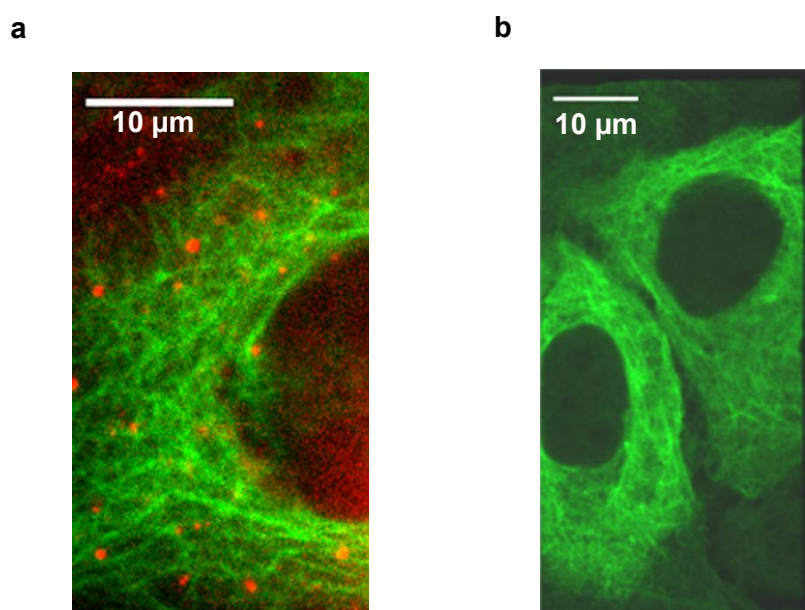


Figure 9.6: Reference experiment - exposure of living HuH7 cells to unloaded CMS and to dissolved colchicine. (a) HuH7 cells (green) after 2 hours of incubation with POPC-coated CMS without colchicine stay alive. (b) Effect of dissolved colchicine from POPC-coated CMS confined into the dialysis-capped tube on HuH7 cells. After 6 hours the microtubule network of the HuH7 cells is still intact, thus the dissolved colchicine in the cell culture medium does not induce the tubulin depolymerization and cell death.

microtubule network after 2 hours incubation with the lipid-coated nanoparticles. Internalization of the particles was confirmed by a z-stack through the cell volume and by the observation of typical intracellular motion of nanoparticle-filled endosomes along the microtubular network of the cells. Hence, cell death is not caused by the lipid-coated carrier, but by the effect of the released colchicine molecules.

It is known that colchicine has a small but finite permeability across cell membranes and thus may also be able to cross the lipid bilayer of the coated nanoparticles. To investigate the effect of free colchicine which potentially crossed the membrane coating of the nanoparticles, the in-vitro dialysis set-up was applied to the live cell imaging experiment. The cells were exposed to the same concentration of colchicine-loaded lipid-coated nanoparticles as used in the in-vivo experiment described above. Even after 6 hours of exposure to free colchicine diffusing out of the drug-loaded lipid-coated nanoparticles, the microtubule network remained intact and no cell death was observed (Fig. 9.6(b)). This finding clearly shows that the amount of colchicine leaking out of the lipid bilayer

into the medium is too low to trigger cell death. Hence, the cell death observed in the first in-vivo experiment is attributed to the nanoparticle-mediated colchicine delivery into the cancer cells.

The in-vivo delivery experiments have shown, that the lipid coated nanoparticles deliver drugs into cells with a strongly enhanced efficiency compared to the direct cellular uptake of drugs, which are diluted in the medium surrounding the cell. This concentrated delivery of drugs into cells mediated by the lipid coated nanoparticles could be important to pharmaceutical treatment, particularly chemotherapy. Highly concentrated doses of drugs could be efficiently transported into cells, whereas the overall dosis given to the patient could be reduced.

9.6 Future investigations and further applications of the lipid-coated nanoparticles

The fluorescence cross-correlation spectroscopy experiments confirmed that the lipids assemble to a bilayer around the nanoparticles thereby forming a monodisperse, stable colloidal suspension in aqueous solution. Hence, they show, that solvent exchange provides an efficient and reproducible method to encapsulate individual CMS nanoparticles of 50 nm diameter by an intact lipid bilayer. The in-vitro release experiments showed, that they form a defect-free lipid bilayer which acts as a cap-system, preventing the diffusion of guest molecules out of the mesoporous structure of CMS nanoparticles. Thus, the lipid coated nanoparticles build a tunable release-on-demand system. Their ability to efficiently deliver and release drugs into cells was shown by in-vivo experiments. The release mechanism is not yet understood. To elucidate the release mechanism into more detail, super-resolution microscopy or single particle tracking studies could provide valuable insight. Better knowledge of the release mechanism would in its turn allow for improvement of drug design.

The lipid bilayer facilitates polymer-coating, for instance PEGylation is easily done by addition of DSPE-PEG to the lipid solution. As shown in chapter 8, this could prolong the circulation time of the nanoparticle drug delivery system and hence, drastically enhance its efficiency.

Integration of receptor proteins into the lipid bilayer could target cells specifically and improve the uptake mechanism as well as enhance the efficiency of the nanoparticle drug delivery system. This could, for instance, be done by attaching EGF, GE11 or other receptor proteins via PEG-bridges to the lipids. The PEG molecules would prevent the proteins from inserting deeply into the bilayer where they might not be detected by the cell. EGF and GE11 are known to stimulate vesicle fusion as uptake mechanism, which is much more efficient than endocytosis. Consequently, drug delivery could be improved by attaching these molecules to the lipid bilayer.

Moreover, the efficient delivery of the lipid-coated nanoparticles could also be used

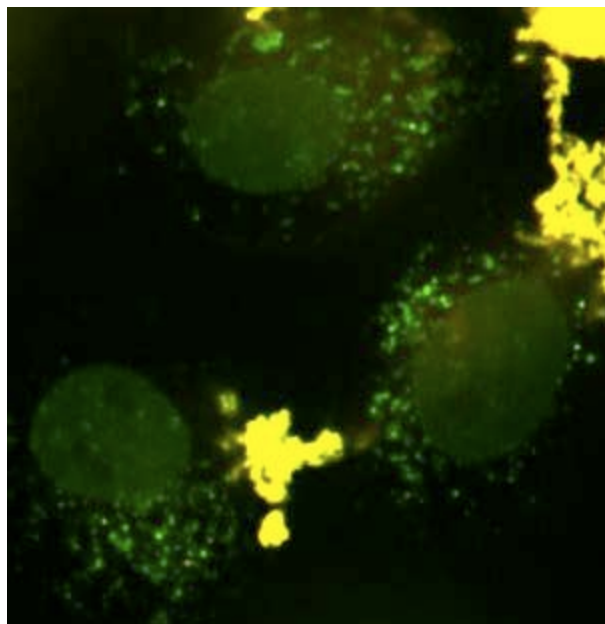


Figure 9.7: *Nanobodies delivered into a HeLa (GFP-PCNA) cell via POPC-coated CMS nanoparticles. The small, green particles are the Atto 488-labeled nanobodies diffusing in the cell. Large aggregates of the nanoparticles (yellow) are not taken up by the cells.*

to transport molecules and nanometer-sized particles, other than drugs, into cells. One example would be a living cell staining method. So far, there is no method to stain cells while they are alive, unless they express fluorescently labeled proteins. Fluorescently labeled nanobodies ([95]) made from alpaca antibodies, provide an option for live cell staining. However, they are taken up by cells in a very inefficient way, which does not allow for accumulation of a sufficient amount of nanobodies needed in the cells for fluorescence microscopy. The nanobodies are small enough (about 2 nm) to fit into the pores of the CMS nanoparticles. Hence, the lipid-coated nanoparticles could serve as an efficient carrier system for staining of living cells by nanobodies. A proof of principle is given by first fluorescence microscopy experiments showing a big amount of green, GFP-labeled nanobodies internalized into living cells (Fig. 9.7).

10 Probing the viscosity in *Dictyostelium discoideum* cells

Chapter 6 provided the basic concepts and understanding to perform FCS experiments in living cells. The findings showed, that changes of the viscosity due to crowding strongly influence the results of FCS measurements. Hence, FCS can be used to probe the viscosity in living cells. Here, FCS is employed to study the viscosity in *dictyostelium discoideum* cells. With different mutants the local effective viscosity is probed in the cytoplasm as well as in the actin cortex. The effect of drug treatment on the polymerization of the cell is studied using latrunculin and jasplakinolide. Since FCS measures viscosity at very small volumes and short timescales compared to fluorescence microscopy, the experiments allowed for the detection of actin waves and for investigation of their viscosity.

10.1 Probing the viscosity in living cells with Fluorescence Correlation Spectroscopy

Viscosity in cells varies a lot depending on the outer conditions, the cell type and the region of the cell. Both, polymerization of the actin network and crowding by a variety of heterogeneous, polydisperse macromolecules, have a strong influence on the cell's viscosity [43]. Since diffusion depends on viscosity, this has immediate consequences on the mobility and thus on reaction rates and transport properties within the cell. To gain a better understanding of cellular processes, many theoretical as well as experimental studies are performed on diffusion in confined, crowded systems and the impact on reactions within these systems [96–100]. All theoretical models and computer simulations, which address this topic, need to rely on experimentally determined viscosities to describe the diffusion characteristics of a cell in a most realistic way [101]. Hence, it is desirable to measure viscosity in cells as accurate as possible.

Many experiments have been performed to measure effective viscosities in cells using micrometer-beads [98,99]. Values resulting from these experiments are valid for objects of micrometer size only, since diffusion in crowded systems depends on the tracer size. Another method to probe effective viscosities in vivo is fluorescence microscopy [102]. This technique explores diffusion on rather long time scales and in quite large volumes. The confocal setup allows FCS to probe the local viscosity in a very small, well-defined

volume. Furthermore, FCS uses small fluorescently labeled tracer proteins such as GFP and measures diffusion on much shorter time scales compared to conventional fluorescence microscopy. Viscosity enhancement due to binding to the tracer molecule can be discriminated from an increase caused by changes of the local environment by comparing the diffusion characteristics in the cell with the results obtained from cell lysate. With these properties, FCS complements conventional techniques perfectly.

Challenges for viscosity measurements are time dependent viscosity changes and strong local variations, where regions of equal viscosity are confined to very small volumes, such as the actin cortex which is only a few nm thick. Both challenges can be addressed fairly well with FCS. The comparatively small confocal volume can be even further reduced by a confinement of the probe volume. In the case of cell experiments, different mutants with fluorescently labeled proteins, which appear only in the region of interest, can be used to reduce the probe volume. To probe, for instance, the actin cortex, a mutant with GFP labeled proteins, which exist only in the cortex, is used. Time-dependent viscosity changes can be measured with FCS as long as they vary on time scales longer than the measurement time (i.e. 10-20 s). One such time dependent phenomenon of very strong current research interest are actin waves. They occur e.g. in *dictyostelium* cells, when they sense a barrier or food [103]. They consist of polymerization fronts which move within the cell and hence change the local viscosity with time. Since they appear on a time scale equal to a typical FCS measurement time, they can be detected.

Laser Scanning Microscopy was used to image the cells and to position the focus at regions of interest (Fig. 10.1). Autocorrelation curves obtained from in-vivo or lysate FCS experiments were fitted with the modified autocorrelation function for three-dimensional Brownian diffusion, which takes the influence of the polymer network into account [104]:

$$G(\tau) = 1 + \frac{1}{N} \cdot \frac{1}{1 + (\frac{t}{\tau_D})^\beta} \frac{1}{\sqrt{1 + S^{-2}(\frac{t}{\tau_D})^\beta}} \quad (10.1)$$

The fitting parameters yield the number of particles in the focal volume, N , and the diffusion time, τ_D . The additional parameter β reveals the influence of the polymer network and represents the scaling exponent indicating the deviation from normal diffusion:

$$\langle r^2 \rangle = Dt^\beta \quad (10.2)$$

The diffusion coefficient D was determined with equation 4.5 and equation 4.7 was used to deduce the viscosity η relative to the viscosity in aqueous solution η_0 :

$$\frac{\eta}{\eta_0} = \frac{D_0}{D} \quad (10.3)$$

where D_0 denotes the diffusion coefficient in aqueous solution.

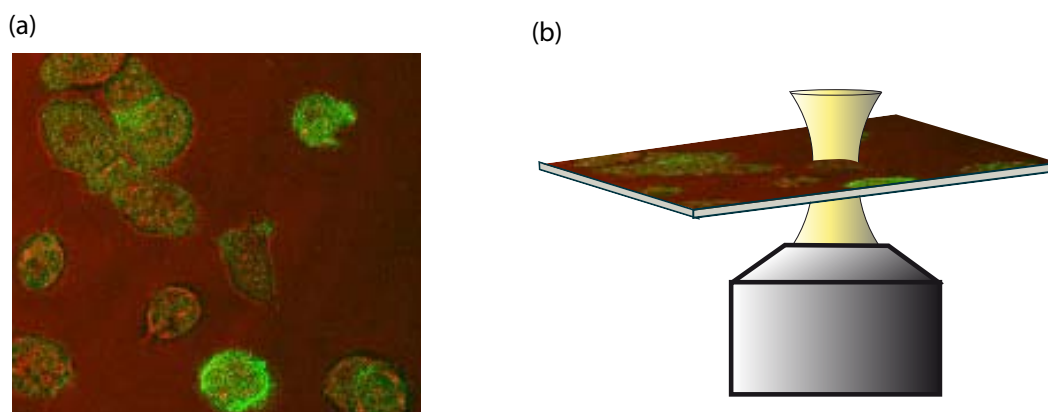


Figure 10.1: *Laser Scanning Microscopy images the cells on the cover slide (a) and allows one to position the focus at regions of interest (b).*

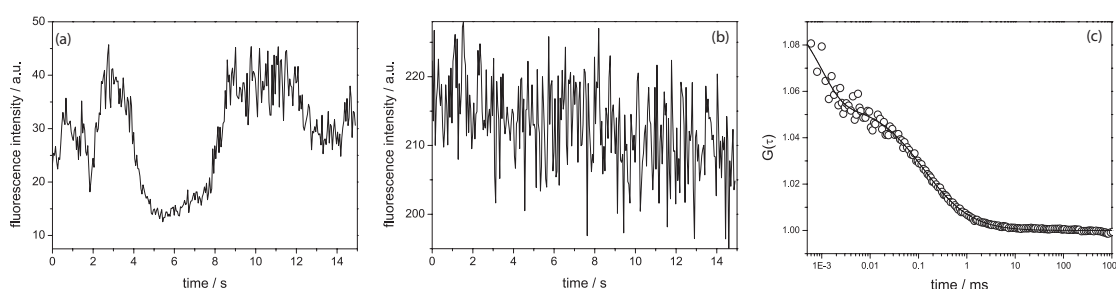


Figure 10.2: *(a) Intensity trace exhibiting strong irregular fluctuations on large time scales. (b) Intensity trace with uniform fluctuations. (c) Autocorrelation curve obtained from an experiment in the mutant expressing free GFP.*

10.2 Viscosity in the cytoplasm of dictyostelium cells

In order to determine the effective local viscosity in *dictyostelium* cells, FCS measurements were performed on different mutants. For all mutants, the intensity time traces obtained from these experiments could be distinguished into two groups: some showed strong, irregular fluctuations on large time scales (in the range of seconds), whereas others showed only small uniform fluctuations on a μs time scale. Examples of intensity traces of both groups are given in Fig. 10.2. Intensity traces which exhibit strong, irregular fluctuations were already observed by Ruchira and coworkers [105] and can be attributed to movements in the cytoplasm, e.g. by the nucleus or diffusing vesicles passing the confocal volume. For further evaluation only intensity traces with uniform fluctuations were chosen. They were analysed as described above and yielded autocorrelation curves similar to the one depicted in Fig. 10.2(c).

Evaluation of experiments on a mutant with free GFP diffusing within the cytoplasm showed a mean scaling exponent β of 0.84 indicating slightly subdiffusive motion. The mean diffusion time was determined to be 168 μs yielding a diffusion coefficient of 59 $\mu m^2 s^{-1}$. This is 2.5 times slower than the values obtained from lysed cells, which showed a diffusion coefficient of 148 $\mu m^2 s^{-1}$ and normal diffusion ($\beta = 0.97$). Control measurements on purified eGFP (diffusion coefficient: 157 $\mu m^2 s^{-1}$, $\beta = 1.01$) compare fairly well with the values from the lysed cells. Hence, additional slowdown of the GFP diffusion due to binding of cellular components can be excluded and the slowdown of the diffusion coefficient can be fully attributed to an enhanced viscosity of 2.47 mPas in the cell.

This increase of the viscosity is slightly less than reported for other eucaryotic cells [40]. Potma et al. [106] measured for *dictyostelium* cells under various conditions an increase of the viscosity by a factor of 2-4. Compared to these data, the increase of the viscosity of 2.5, that was determined here for the cytoplasm is at the lower end, indicating a low level of polymerization. This might be due to the immobilization of the cells with aminosilvanized surfaces. Indeed, Ruchira et al. [105] found a reduced viscosity in immobilized cells. However, the enhancement is still larger as to be explained by macromolecular crowding of monodisperse solutions. Experiments on model systems of monodisperse vesicle solutions yield a factor of 2 for the viscosity increase and do not show any signs of subdiffusion [38]. The enhancement of the viscosity beyond macromolecular crowding effects and the subdiffusivity of the motion indicated by the scaling exponent of 0.84 might be explained by effects due to polymerization of the actin network. Dauty et al. [61] report a drastically increased reduction of DNA diffusion in polymerized in-vitro actin networks compared to solutions crowded by spheres. To see whether this is the the reason of the measured viscosity enhancement, experiments were performed on a mutant expressing GFP-labeled actin. As the mutant with free GFP, this one shows the same slowdown of diffusion by a factor of 2.5 compared to the lysate. The diffusion coefficient of the actin in the cell was determined to be 41 $\mu m^2 s^{-1}$ and in the lysate it was 105 $\mu m^2 s^{-1}$. Also the scaling exponents were very similar compared to the free GFP mutant: 0.82 for the actin in the cell and 0.97 for the lysate. After this verification that the same effect is measured with both mutants, the hydrodynamic radius of actin is calculated to find out about its polymerization. Using equation 4.7, the hydrodynamic radius of actin was calculated to be 2 nm, compared to a radius of 1.5 nm for GFP. The value for actin is consistent with its size reported in literature [107]. From that one can conclude, that under the experimental conditions actin is present as a monomer and not polymerized in the cytoplasm of the cells. Hence, the changes in diffusion (i.e. the strong enhancement of the viscosity and the subdiffusive motion) cannot be explained by effects due to the polymerized network. An explanation might be that the polydispersity of macromolecules in the cells (cf. Fig. 10.4) leads to anomalous diffusion and a stronger increase of the effective viscosity compared to monodisperse model solutions.

10.3 Viscosity in the actin cortex of dictyostelium cells

Compared to the thickness of the actin cortex of a few nm, the focus size of $0.5 \mu\text{m}$ is too large to probe the actin cortex only. A viscosity measurement of the actin cortex would therefore always be determined by the surrounding regions, in this case by the viscosity of the cytoplasm. This restriction can be circumvented with the help of a mutant expressing GFP-labeled LIM protein, which is present only in the actin cortex under normal conditions. This allows one to measure the viscosity in the actin cortex. Experiments with this mutant yield a diffusion coefficient of $38 \mu\text{m}^2\text{s}^{-1}$ in the cells and $150 \mu\text{m}^2\text{s}^{-1}$ for the lysed cells. The hydrodynamic radius of LIM proteins calculated from the diffusion coefficient in lysed cells is 1.5 nm. Since this is a size typically found for unbound, freely diffusing proteins, again, an additional slowdown due to binding of other proteins to the tracer molecule can be excluded.

Comparison of the diffusion constant in the cell and in the lysate shows an increase of the effective viscosity in the actin cortex by a factor of 3.9 compared to aqueous solution and by a factor of 1.55 compared to the non-polymerized cytoplasm. Since the actin cortex is known to consist of a highly polymerized actin network and the LIM protein is expressed only during polymerization of actin, this additional increase of the effective viscosity can be explained by the influence of the actin network. In vitro experiments on actin diffusion confirmed a scaling law, which was predicted by the reptation model for flexible chains and relates the diffusion coefficient D with the actin concentration c_a and the mesh size ξ of the actin network [108]:

$$D \propto c_a^{-1} \propto \xi^2 \quad (10.4)$$

This scaling law yields an increase of the actin concentration in the actin cortex by a factor of 1.55 compared to the cytoplasm and a corresponding decrease in the mesh size of the actin network by a factor of 0.4.

The scaling exponent reveals the polymerization of the actin cortex, as well. In the LIM mutant it could be determined to be 0.79 in the cells and 0.99 for the lysed cells, indicating normal diffusion for the lysate and subdiffusive motion in the cortex. The value in the cells agrees very well with the value of 0.75 reported for example for the actin cortex of amoebae [109] and for in-vitro actin networks [104]. Furthermore, it is consistent with the value of 0.75 predicted for actin filament chains by theoretical calculations.

10.4 Influence of jasplakinolide

Cells of the actin mutant were treated with $5 \mu\text{M}$ jasplakinolide, which leads to polymerization of the actin in the cytoplasm. As expected, the results in this case are very similar to those in the actin cortex: $\beta = 0.74$ and the diffusion coefficient $29 \mu\text{m}^2\text{s}^{-1}$, yielding a viscosity, which is enhanced by a factor of 3.7 compared to aqueous solutions.

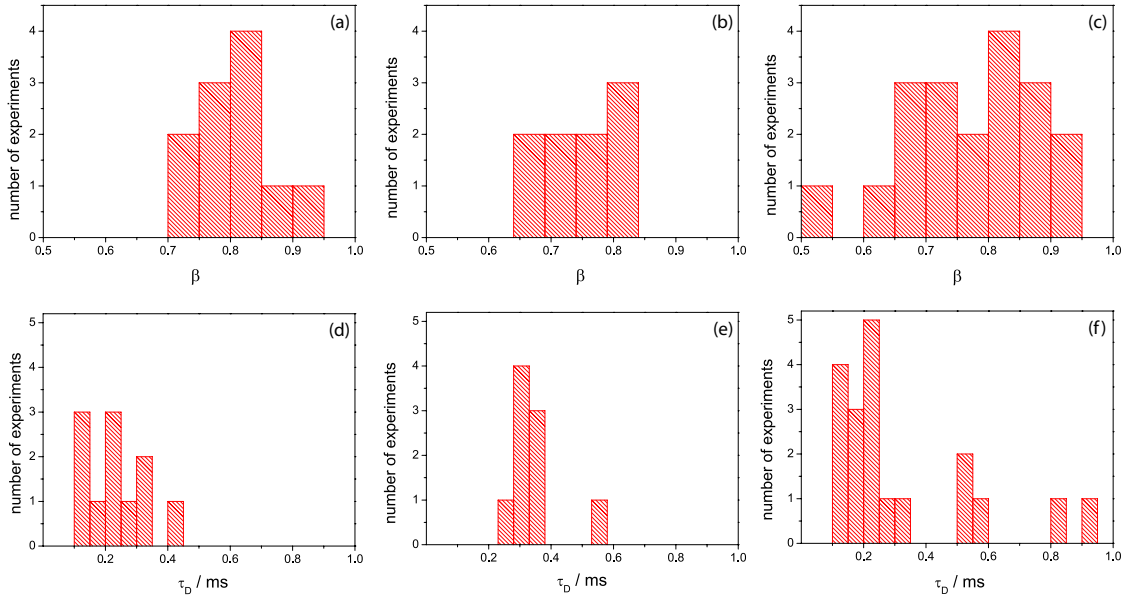


Figure 10.3: Histograms of the scaling exponents in the actin mutant without drugs (a) and upon jasplakinolide (b) and latrunculin (c) treatment and histograms of the diffusion times measured in the actin mutant without drugs (d), and upon jasplakinolide (e) and latrunculin (f) treatment. While the distributions of the parameters of untreated and jasplakinolide treated cells are fairly narrow, the parameters of cells treated with latrunculin exhibit a broad distribution.

Hence, jasplakinolide at the concentration used polymerizes the cells up to an extent as in the actin cortex, leading to the same diffusion conditions. Based on these findings, cells treated with jasplakinolide can serve as an easy to access model system to probe viscosity and diffusion characteristics of the actin cortex. Furthermore, variation of the concentration of jasplakinolide will allow for regulation of the degree of polymerization and thus for experiments on the influence of polymerization on the effective viscosity.

10.5 Latrunculin induced actin waves

Latrunculin A was added to the actin mutant at a concentration of $5 \mu\text{M}$. The results of the experiments are shown in Fig. 10.3. While the scaling exponents and diffusion coefficients of untreated cells and cells treated with jasplakinolide are well centered around a mean value, both scatter a lot in cells treated with latrunculin. Scaling exponents range from 0.5 to 0.9 and diffusion coefficients from about $10\text{-}70 \mu\text{m}^2\text{s}^{-1}$. Thus, some experiments show diffusion as in unpolymerized, untreated cells, some reveal diffusion characteristics as under conditions of complete polymerization like in the actin cortex or after jasplakinolide treatment and some are located somewhere in between the two cases. Since all other experiments without latrunculin show much more homogeneous results,

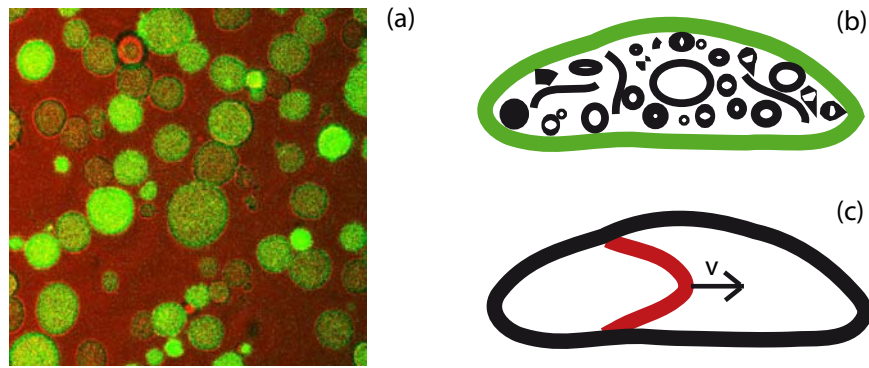


Figure 10.4: (a) Laser Scanning Microscopy image of *dictyostelium* cells expressing GFP labeled actin after treatment with latrunculin A. (b) Schematic drawing of a cell surrounded by the actin cortex (green) and with the cytoplasm crowded by polydisperse macromolecules. (c) Schematic drawing of a cell with a polymerization front of an actin wave (red line) moving with velocity v .

the strong scattering of the results can be attributed to the influence of latrunculin and is not caused by data uncertainties due to instrumentation and analysis.

Latrunculin A at a concentration of $5 \mu\text{M}$ is reported to induce actin waves in *dictyostelium* cells [110]. These waves move with a velocity of a few $\mu\text{m}/\text{min}$ [110,111] and sometimes they stop and change direction. Since the actin front of the waves is of a size of roughly $2 \mu\text{m}$, the confocal volume is filled by an actin front for about 10-15 s (cf. Fig. 10.4). Thus, an actin front entering the confocal volume just before the measurement starts fills the confocal volume for the whole time of a 15 s measurement, especially, when it stops there and changes direction. Hence, the low scaling exponents and the high viscosities indicating a highly polymerized actin network as measured in some of the experiments on latrunculin treated cells can be attributed to such polymerization fronts of actin waves and reveal their local effective viscosity. Scaling exponents and viscosities similar to those of untreated cells result from regions in the cytoplasm, which are not influenced by actin waves. Experiments showing values of scaling exponents and viscosities in between unpolymerized and completely polymerized conditions could result from regions of actin waves that are less polymerized or from actin waves that passed the focal volume during the experiment which then lead to a measurement of the time averaged effective viscosity. Finally, the heterogeneity of the data can be well explained by the actin waves. Since only the polymerization moves with the wave, but no molecules at all (all molecules involved are constantly destroyed and renewed), actin waves cannot be detected by direct observation of molecular movements. So far, the only method was to use mutants expressing GFP labeled proteins that are present in such waves only. Here it was shown, that FCS viscosity measurements allow for the detection of actin waves independent of these proteins and at the same time, they reveal for the first time the viscosity in actin waves. This determination of the effective viscosity in

actin waves could be of great interest for computer simulations of these waves.

In general, the experiments of this chapter have shown that FCS is a powerful tool to determine effective viscosities in cells. Particularly, it allows for very accurate determination of changes of the local effective viscosity by comparing viscosities in cells relative to the value in lysate.

11 Two-photon Fluorescence Correlation Spectroscopy

Chapter 6 provided evidence, that it would be desirable for measurements in complex media to use a technique with reduced scattering, such as two-photon fluorescence correlation spectroscopy. In-vivo experiments in cells, as shown in the previous chapter would also profit from two-photon excitation. To this end, a home-built two-photon microscope which can be used for laser scanning microscopy as well as for fluorescence correlation spectroscopy was set up. This chapter first compares one- and two-photon microscopy, then the set-up is described and first results of auto- and cross-correlation measurements are shown.

11.1 Comparison of conventional one-photon- and two-photon microscopy

Two-photon excitation is performed at wavelengths of about double the size compared to one-photon excitation. Hence, for most dyes, wavelengths in the infrared are used for two-photon excitation. Since scattering increases with the frequency ω^4 , it is drastically reduced in the infrared compared to the visible regime, which is usually used for one-photon excitation. This very much improves the performance of experiments in living cells which exhibit a strong background signal due to scattering in the case of one-photon excitation [112]. Furthermore, this decrease in scattering enhances the signal to noise ratio in strongly scattering media, such as plasma or tissue and reduces artifacts due to focus distortion in FCS experiments, which are performed in complex soft matter systems, as shown in chapter 6.

Another favourable characteristics of two-photon microscopy is its inherently confined excitation volume [17, 112]. Absorption of light is limited to the focus where photon densities are high enough to allow for two-photon processes. This has great potential for medical applications, such as photodynamic therapy, which can exploit this confinement to precisely address treatment without affecting healthy tissue [112]. In research, this restriction of the excitation volume was used for instance, for activation of photoactivable proteins at well-defined positions. Since cells are damaged by intense light, in two photon microscopy, damage is reduced to a very small volume, thus making two-photon microscopy a powerful tool for cellular applications [9, 113, 114]. However, for such

applications, the high photon densities in the focus, which exceed those used for one-photon excitation by far, have to be considered, particularly their effect on the cell at the focal volume [60, 115].

Due to the sharply defined and very small focal volume, two-photon excitation is very well suited for fluorescence correlation spectroscopy. Here, the intrinsically confined focus allows for a very simple optical setup, without the need for confocal optics which employs two pinholes to confine the focal volume of a one-photon setup. Another advantage of two-photon excitation for fluorescence correlation spectroscopy is the broadening of excitation spectra of commonly used dyes due to the modified selection rules of a two-photon process as compared to one-photon excitation [116, 117]. Consequently, many dyes with well separable emission spectra can be excited at the same wavelength. This allows for dual-colour cross-correlation experiments with only one excitation wavelength, thus the challenge to match the foci of the two excitation colours as in one-photon cross-correlation experiments is inherently solved.

11.2 Setup of the two-photon microscope

In order to benefit from the advantages of two-photon excitation concerning experiments in complex, scattering media and particularly in cells [113], a two-photon microscope was built. One future application should be to measure GFP-expression in bacteria, since bacteria scatter a lot and are not accessible for FCS experiments with our commercial one-photon microscope. *E. coli* bacteria have a typical size of $1\mu\text{m} \times 1\mu\text{m} \times 3\mu\text{m}$, therefore the setup had to be very stable and the piezo-scanners very precise. The components of the microscope should be easily accessible to allow for realignment and customized extensions, thus the whole setup was home-built. Fig. 11.1 schematically shows the setup including the beam path and all optical components. The excitation source is a femtosecond-pulsed tunable IR-laser (Chameleon, Coherent). The beam passes several OD-filters, which allow for regulation of the excitation intensity, and is directed by two mirrors into the objective, which focusses the beam into the sample. The fluorescent light of the sample is collected by the objective and directed into the detection path via a dichroic mirror, which separates the fluorescence from the excitation light. The detection path consists of several high quality bandpass filters, which further discriminate the fluorescence from excitation- and scattered light and allow for separation of two different fluorescence colours for cross-correlation experiments. An optional beamsplitter divides the beam into two, which each hit an avalanche photodiode (EG&G) for detection. The detected signals are correlated by a hardware correlator (ALV, Langen) and displayed on the computer. The sample chamber is fixed on two piezo-stages (Physik Instrumente) which allow for precise scanning.

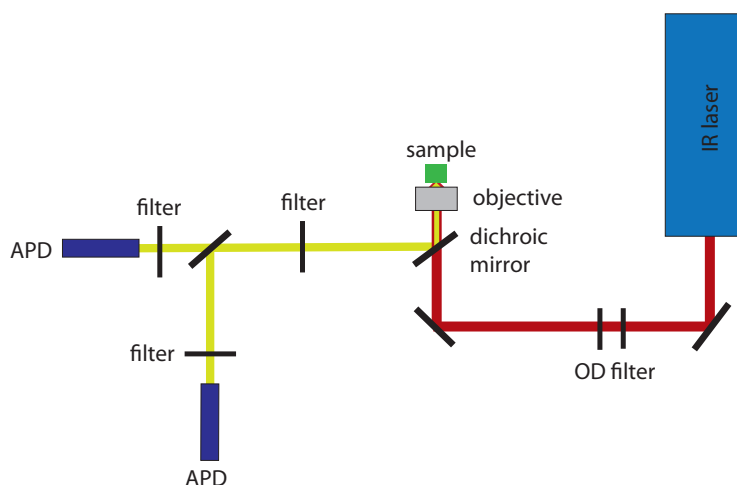


Figure 11.1: Schematic drawing of the two-photon setup. The beam is emitted from the IR-laser and via several mirrors it is directed into the objective, which focusses the light into the sample. The fluorescence light collected from the objective is separated from the emission light by a dichroic mirror and several bandpass filters. Finally, it is directed into the APDs, which detect the emitted photons.

11.3 First results of auto- and cross-correlation experiments

Fluorescently labeled vesicles were chosen as sample for the very first test measurements. One vesicle carries several dye-molecules and hence exhibits a bright fluorescence signal which should be easily detectable. Fig. 11.2(a) shows an autocorrelation curve from Bodipy labeled vesicles of 100 nm diameter. This diameter can be used to calculate the diffusion coefficient of the vesicles with equation 4.7 and hence the focal volume can be determined with equation 4.5 and the fit parameters yielding a focal volume of 14 fl for this setup. This value is fairly large compared to the value obtained from theoretical calculations for two-photon excitation, according to [112]:

$$\omega_x = 0.61 \frac{\lambda}{NA} \quad \omega_z = \frac{\pi \lambda}{NA^2} \quad (11.1)$$

which lead to a value of 0.8 fl for the focal volume with the optical settings used here (i.e. a numerical aperture $NA = 1.2$ and an excitation wavelength of 900 nm). The discrepancy of the values obtained for the focal volume might be due to distortion of the focus in the experiment and could be improved by further optimization of the alignment and the excitation intensity.

As a second test sample quantum dots were used, which lead to a strong fluorescence signal as well. Fig. 11.2(b) shows the distinct autocorrelation curve obtained from the quantum dots. As a next step, dye solutions such as Alexa 488 should be tested. So

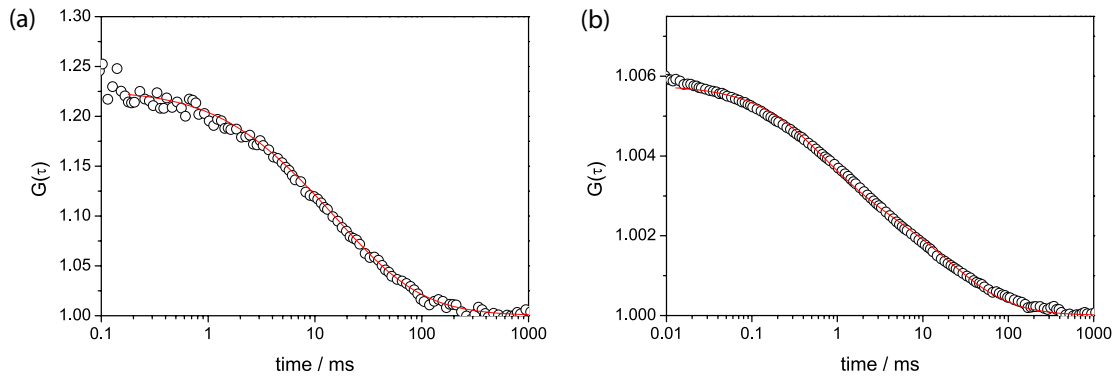


Figure 11.2: Autocorrelation functions of fluorescently labeled vesicles (a) and quantum dots (b) obtained from the two-photon setup.

far, a clear intensity signal was obtained from dye solutions; successful measurements of autocorrelation curves, however, are still a challenge. To this end, the signal-noise ratio has to be improved by optimization of the alignment of the detection path and maybe addition of further high-quality bandpass filters. Furthermore, the excitation intensity and pulse width has to be optimized, since there is only a small regime of intensities which lead to efficient two-photon excitation of the sample.

Two-photon FCS bears great potential for cross-correlation applications due to the fact that two dyes with spectrally separable emission spectra can be excited simultaneously with the same wavelength. Therefore, detection filters were chosen to have the option of performing cross-correlation spectroscopy. As a proof of principle, cross-correlation experiments on vesicles labeled with both, Texas Red and Bodipy, were performed. Fig. 11.3(a) shows the obtained curves of the autocorrelation of each single channel and their cross-correlation. The effect of addition of vesicles labeled only with Texas Red on the cross-correlation curve is shown in Fig. 11.3(b). The amplitude of the cross-correlation function decreases, since the relative amount of vesicles carrying both dyes and thus leading to the cross-correlation signal decreases with increasing amount of single colour labeled vesicles. Hence, the experiments give evidence of successful cross-correlation performance of the home-built two-photon setup and promise future applications for instance for binding experiments.

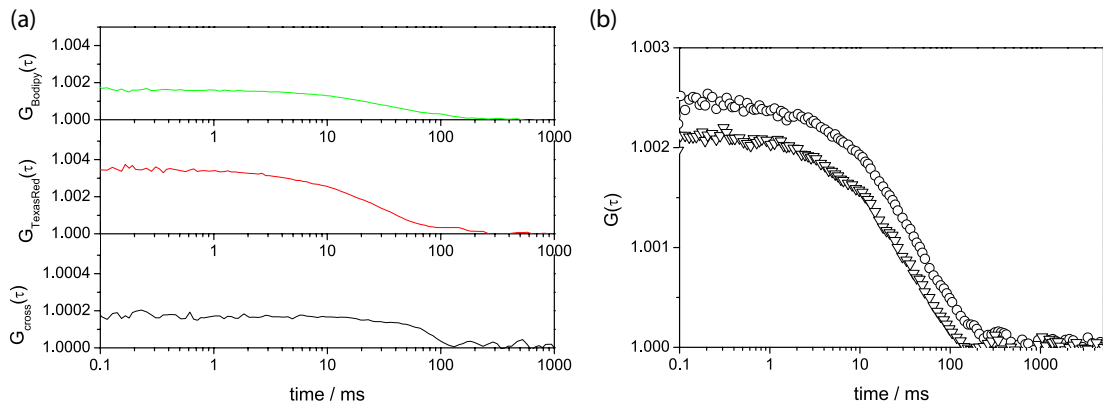


Figure 11.3: Two-photon cross-correlation of vesicles labeled with Bodipy and Texas Red. (a) Autocorrelation of the Bodipy-signal (green line) and the Texas Red-signal (red line). The black line represents the cross-correlation of Bodipy and Texas Red signal. (b) Cross-correlation of vesicles labeled with both, Bodipy and Texas Red (\circ). Upon addition of vesicles labeled with Texas Red only, the amplitude of the cross-correlation decreases (∇).

12 Electrostatically coupled diffusion of short ds-oligonucleotides on cationic lipid membranes

Chapter 7 described experiments on diffusion of proteins, namely FVIIIa and annexin, on a supported lipid membrane, which were performed to test whether they move independently or in a correlated manner. In future research similar measurements on supported lipid bilayers could help unravel complex protein-membrane interactions involving mechanisms as explained in chapter 5.3, since they allow for the investigation of influences of the membrane composition or lipid rearrangements and of correlations of proteins and lipids. To this end, DNA diffusing on a supported membrane serves as excellent model system, which is sufficiently well understood. As a proof of principle for such FCS experiments on supported lipid bilayers, measurements on diffusion of short ds-oligonucleotides on supported cationic lipid membranes were performed. This chapter describes these test experiments, including autocorrelation measurements on fluorescently labeled lipids and on DNA diffusing on the membrane under various conditions (i.e. different salt concentrations of the buffer, different DNA lengths, an applied electric field) and discusses cross-correlation studies on the diffusion of DNA and lipids.

12.1 Fluorescence Correlation Spectroscopy in two dimensions

Proteins as well as DNA bound to a supported lipid membrane experimentally realizes a 2D-confinement of polymers (Fig. 12.1). Several groups have reported on FCS experiments on two dimensional samples [118,119]. They all studied lipid diffusion within membranes. These measurements face one major challenge: membranes are only a few nm thin and therefore, the setup has to be very stable to guarantee for the focus to stay within the membrane and illuminate it at a constant spot size. Once, a very stable focus position is achieved, the experiments can be carried out as in three dimensional samples. Fig. 12.2(a) shows a typical intensity time trace obtained from lipids diffusing within a membrane and Fig. 12.2(b) displays the corresponding autocorrelation curve. Such autocorrelation curves can be described with equation 4.4 modified for the case of

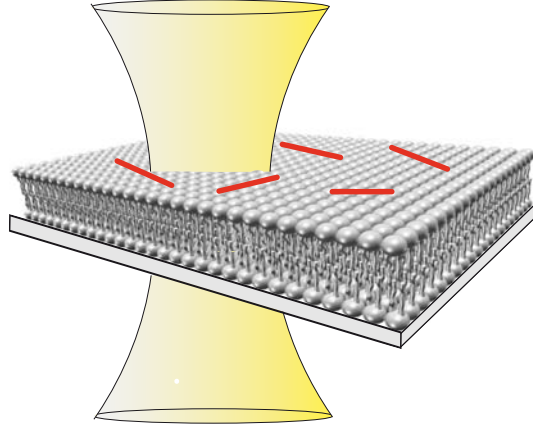


Figure 12.1: *DNA diffusing on a supported lipid bilayer, representing a confinement of polymers into two-dimensions. For FCS experiments on membranes the focus position needs to be very stable since small variations in the height lead to an immediate change of the size of the illumination spot and hence strongly influence the measurement.*

two dimensions [118]:

$$G(\tau) = \frac{1}{N} \cdot \frac{1}{1 + \frac{\tau}{\tau_D}} \quad (12.1)$$

The red line in Fig. 12.2(b) represents a fit according to this equation. Since the membrane is thinner than the focal height and due to the Gaussian shape of the focus, the size of the focal spot on the membrane varies with its position in the focus (Fig. 12.1). Thereby, the position of maximum intensity, does not necessarily coincide with the centre position of the focus. Hence, the focal width can not be taken from a calibration measurement in solution, it rather has to be determined by a z-stack of measurements. Both, the particle number and the diffusion time resulting from these measurements exhibit a parabolic dependence on the z-position of the focus. Fitting these parabolae according to [118]:

$$N = N_0 \left(1 + \frac{\lambda_0^2 \Delta z^2}{\pi^2 n^2 \omega_0^4} \right) \quad (12.2)$$

and

$$\tau_D = \frac{\omega_0^2}{4D} \left(1 + \frac{\lambda_0^2 \Delta z^2}{\pi^2 n^2 \omega_0^4} \right) \quad (12.3)$$

yields the particle density, their diffusion coefficient, D , and the focal width, ω_0 .

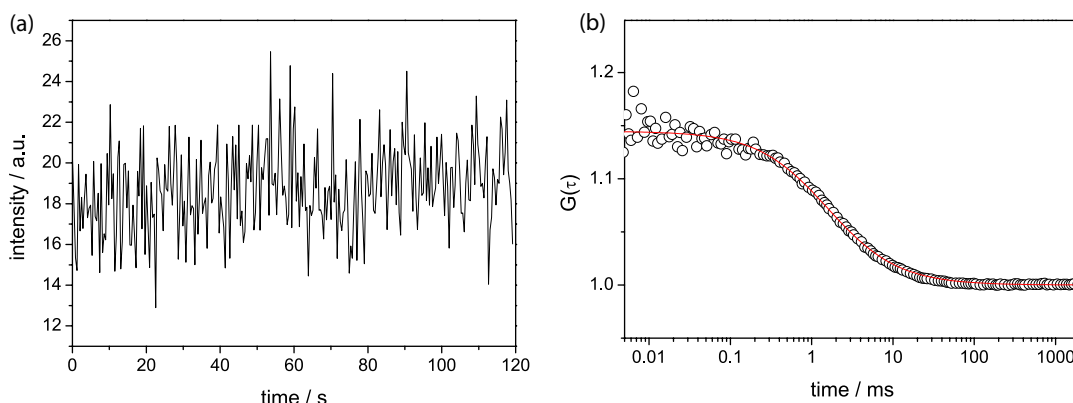


Figure 12.2: (a) Typical intensity trace and (b) autocorrelation curve of DNA diffusing on a supported lipid membrane. The red line represents a fit according to equation 12.1.

If the illumination and fluorescence distributions are Gaussian, the autocorrelation function can be written in terms of the mean square displacement $\langle r^2 \rangle$:

$$G(\tau) = \frac{1}{N} \cdot \frac{1}{1 + \frac{\langle r^2 \rangle}{\omega^2}} \quad (12.4)$$

where ω is the beam waist. The mean square displacement of typical lipid diffusion within the supported membrane is shown in Fig. 12.3(a) in a logarithmic plot. It coincides very well with a line of slope 1, which indicates normal diffusion behaviour. The diffusion coefficient obtained from these measurements is $5 \mu\text{m}^2\text{s}^{-1}$. These findings are in exact agreement with data from literature, which report the same value for the diffusion coefficient and normal diffusion for lipids in membranes [118]. Hence, they serve as a very good proof of principle for the performance of FCS measurements on two-dimensional systems.

12.2 DNA diffusion on supported lipid bilayers

In this thesis, for the first time FCS measurements were performed on molecules which diffuse on a supported lipid membrane and thus are confined to two-dimensional diffusion. The rectangular data points in Fig. 12.3(b) represent the mean square displacement obtained from an FCS experiment on 20 basepair oligonucleotides diffusing on a DOPC-membrane containing 20% positively charged DOTAP lipids. For comparison, the mean square displacement of lipids is shown in the same graph (triangles). The data sets can be described by parallel lines with slope 1, indicating normal diffusion. Compared to the mean square displacement of the lipids, that of the DNA is shifted towards slower diffusion. Quantitative evaluation yielded a diffusion coefficient of $2 \mu\text{m}^2\text{s}^{-1}$. The lipid

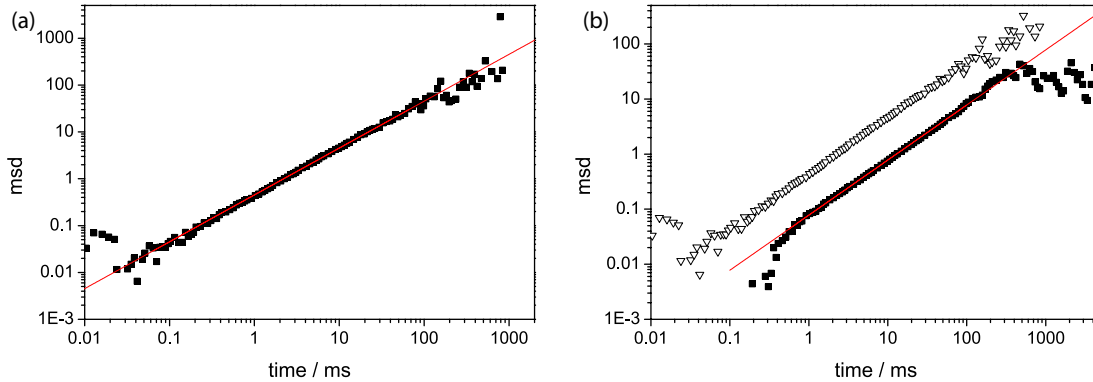


Figure 12.3: (a) Mean square displacement of lipid diffusion within a supported lipid bilayer. (b) Mean square displacement of 20 bp DNA diffusing on a supported lipid membrane (■). For comparison the mean square displacement of lipid diffusion (△) is shown as well. The red lines represent linear fits according to normal diffusion.

diffusion within the membrane does not change upon binding of the DNA and revealed again a diffusion coefficient of $5 \mu\text{m}^2\text{s}^{-1}$.

To study the influence of the membrane composition on the diffusion of the DNA, the concentration of charged lipids was varied. Fig. 12.4(a) shows first results on the dependence of the diffusion coefficient of 20 basepair oligonucleotides on the concentration of positively charged DOTAP lipids. Except for the value at 30% charged lipid, the diffusion coefficients decrease with increasing charge concentration, indicating a slow down of the movement. However, the data need to be confirmed before the exhibited behaviour can be discussed and explained, since data of two-dimensional FCS experiments scatter a lot and a good statistics is necessary for reliable data.

Schlagberger et al. [120] found an interesting dependence of the DNA diffusion in solution on the salt concentration, consisting in a shallow minimum of the diffusion coefficient at a screening length comparable to the polymer length. In order to investigate the salt-dependence of DNA diffusion on membranes, the diffusion of 40 basepair oligonucleotides on a membrane with 20% charged lipid was measured as a function of the NaCl concentration of the buffer. First results are shown in Fig. 12.4(b). Also in this case, statistics needs to be improved to allow for interpretation of the data. Despite the low statistics, all experiments on DNA diffusing on lipid membranes show the ability of FCS to measure diffusion confined to two dimensions and promise a great potential to gain further insight into molecules interacting with and diffusing on surfaces such as lipid membranes.

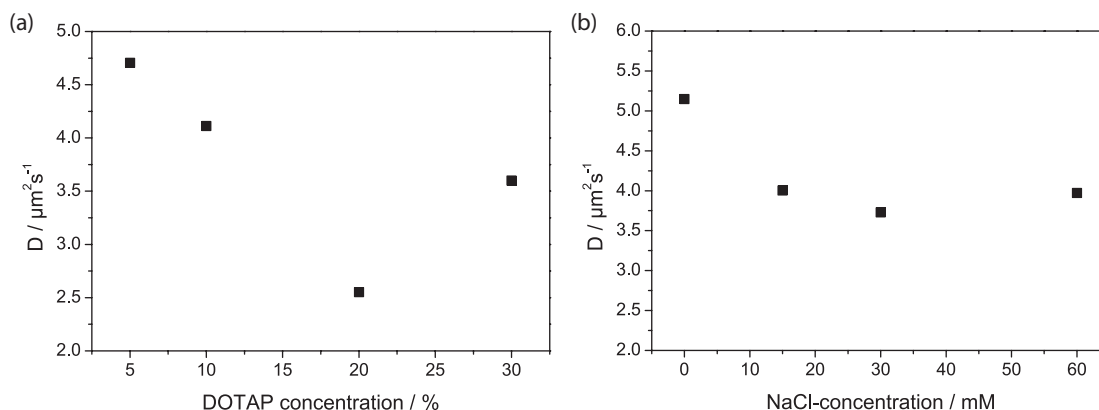


Figure 12.4: Dependence of the diffusion coefficient of DNA diffusing on supported lipid bilayers (a) on the charge content (i.e. DOTAP concentration) of the membrane and (b) on the salt concentration of the buffer solution.

12.3 Cross-correlation-experiments on DNA diffusion on supported lipid membranes

Kahl et al. [121] proposed a biased reptation model for the interaction of DNA with cationic lipid membranes in which the cationic lipids of the membrane assemble underneath the anionic DNA strands. Hence, the diffusive motion of the cationic lipids should be correlated to the DNA movement. Cross-correlation experiments on DNA diffusing on supported lipid membranes, which contain fluorescently labeled cationic lipids could give evidence of such a correlated movement. While cross-correlation of DNA with the uncharged lipids of the membrane should constantly equal 1, indicating the absence of correlated movement, the cross-correlation of DNA with the cationic lipids should reveal a distinct curve.

Cross-correlation experiments were performed with Cy5-labeled DNA and Bodipy-labeled uncharged lipids. Fig. 12.5(a) shows the distinct autocorrelation curves of DNA and uncharged lipids (red and green curves, respectively). No cross-correlation could be detected (black line in Fig. 12.5(a)), indicating the independent movement of DNA and uncharged lipids, as expected. The results of cross-correlation measurements on Cy5-labeled DNA and NBD-labeled cationic lipids (DOTAP) are shown in Fig. 12.5(b). The autocorrelation curves are similar to those obtained from the measurement with uncharged lipids. The cross-correlation curve exhibits a distinct curve, which might indicate correlation of the movement of DNA and charged lipids and hence might confirm the model of Kahl et al. [121]. However, further evaluation showed, that this cross-correlation is mainly caused by crosstalk of NBD into the red channel and the large contribution of crosstalk does not allow for a discrimination of cross-correlation due to correlated movement of DNA and lipids. To obtain reliable results from cross-correlation

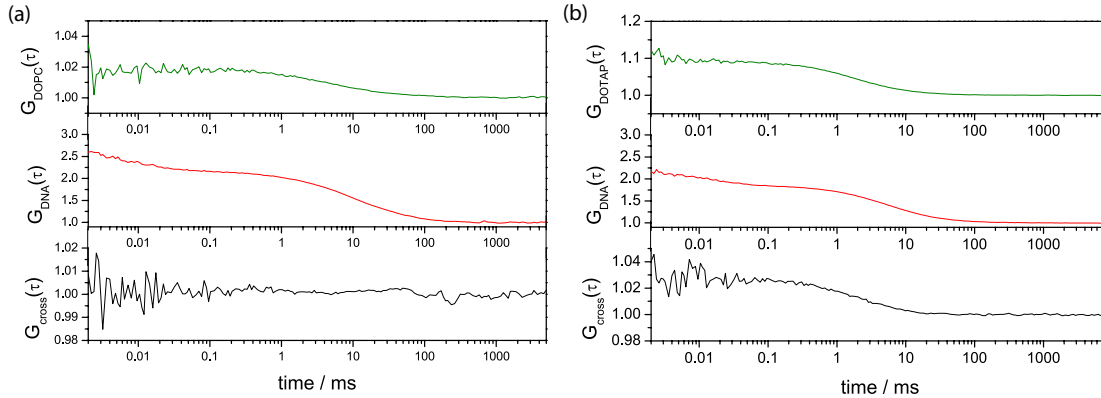


Figure 12.5: Cross-correlation experiments of DNA and lipids. (a) Cross-correlation of DNA and uncharged DOPC lipids. Whereas the autocorrelation of DNA and lipids reveal distinct curves, the cross-correlation of DNA and uncharged lipids is constant. (b) Cross-correlation of DNA and cationic DOTAP lipids. The autocorrelation as well as the cross-correlation exhibit distinct curves.

experiments, charged lipids labeled with a better dye than NBD, showing less crosstalk, such as Alexa 488 are necessary. Then, cross-correlation can contribute to gain an insight into DNA interaction with cationic lipid membranes. Once this is achieved, cross-correlation experiments on supported lipid bilayers could allow for the investigation of protein-membrane interactions and correlations between bound proteins and lipids and thereby contribute to the explanation of complex binding mechanisms.

12.4 Electrophoresis

Gel-free electrophoresis for separation of macromolecules in microfluidic devices, capillaries or at surfaces is very desirable, since gel-electrophoresis is a very long procedure. Many solutions have been proposed to that issue [122, 123]. Applying an electric field to DNA bound to lipid membranes is one possible realization of gel-free electrophoresis [121]. In this section, FCS was employed to investigate the change of movement of DNA diffusing on a membrane upon application of an electric field.

Fig. 12.6(a) shows the autocorrelation curve of the DNA diffusing on the lipid membrane before the electric field was applied. It shows normal diffusion with a diffusion time of 3.8 ms. After this measurement an ac-electrical field of 0.1 Hz, which is slow enough to avoid demixing of the membrane, was applied. The resulting autocorrelation curve (Fig. 12.6(b)) is shifted towards shorter times and hence reveals a faster movement. Analysis with equation 12.1 for normal two-dimensional diffusion reveals a fitting curve (red curve), which does not fully describe the measured data (see also the residuals). Introduction of anomalous diffusion via the parameter β as done for three-dimensional

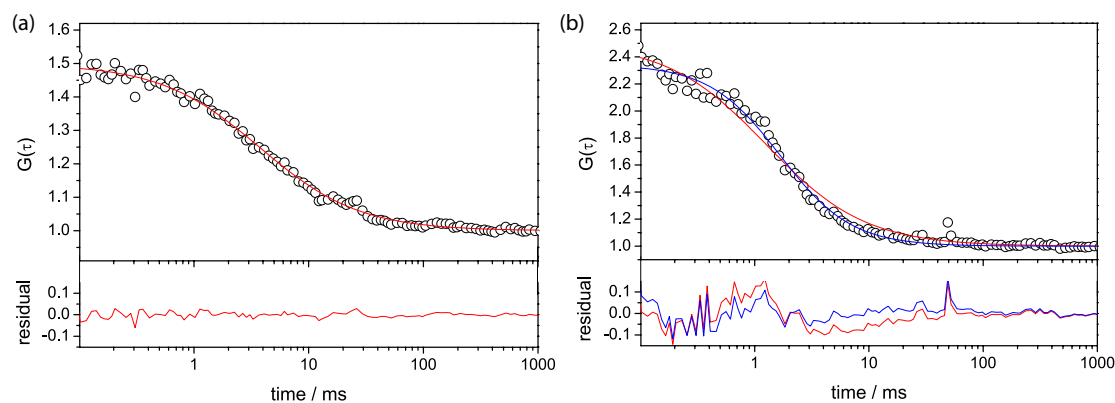


Figure 12.6: *Electrophoresis of DNA on lipid membranes. (a) Autocorrelation of DNA diffusing on a lipid membrane without electric field. The red line represents a fit according to normal two-dimensional diffusion with the residuals shown below, indicating a very good fit quality. (b) Autocorrelation of DNA diffusing on a lipid membrane with an applied electric field. The shorter decay time reveals the acceleration of the DNA by the electric field. The red line representing a fit according to normal two-dimensional diffusion does not fully describe the data, as seen also by the strong deviations of the red residuals. Introduction of a scaling exponent which accounts for directed movement allows for a better fit (blue line and blue residuals).*

diffusion in chapter 10, allows for a full description of the autocorrelation curve (blue line), yielding a diffusion time of 1.7 ms, which is approximately twice as fast as the diffusion without electric field. The exponent β obtained from the fit is 1.4, indicating a directed movement, whereas a fit to the measurement without electric field yields normal diffusion with an exponent β of 1. Thus, the FCS experiments show a faster, directed movement of the DNA on lipid membranes upon application of an electric field, as one would expect in this case. Further experiments have to confirm these findings. A combination with cross-correlation analysis could provide information on the lipid diffusion and its interaction with the DNA movement and hence contribute to a better understanding of two-dimensional electrophoresis on membranes, which then could help to design and improve applications.

In general, the results of this chapter prove that FCS can be performed to measure two-dimensional diffusion on surfaces such as membranes. In particular, cross-correlation experiments on particles diffusing on membranes show great potential for analysis of correlations in the movement of particles and the membrane or of dependencies and independencies of the diffusion of two different species of particles bound to a membrane, as was done in the case of activated FVIII and annexin. In future research such experiments could contribute substantially to the understanding of complex protein-membrane interaction mechanisms.

13 Outlook

The results of this work have demonstrated that binding of FVIII to membranes within coagulation is a highly regulated and complex process. The experiments on its regulation by annexin in plasma have shown that it is subject to even more regulatory interactions, which are not yet understood. Investigations on the interaction of FVIII with further coagulation proteins such as FIX and FX and their influence on FVIII binding to membranes could contribute to a better understanding of this part of the coagulation cascade. This extended knowledge of the underlying biochemical and biophysical processes could provide a basis for systems biology to model and simulate the coagulation cascade, since simple rate equations with constant rates, which are used so far, are not sufficient for a reliable description. This becomes evident for instance by the strong dependence of FVIIIa binding to membranes on their PS-content.

A plasma protein which is very important for hemostasis, since it inhibits FVIII binding to membranes and is involved in the construction of the trombocyte-network, is van Willebrand factor (VWF). Recently it was shown that shear stress induced conformational changes affect the hemostatic activity of VWF [124]. Thus, VWF plays a key role in the detection of blood vessel injury and the succeeding start of hemostasis. The exact effect of shear forces on hemostasis via VWF however is unknown. Various methods to fluorescently label VWF exist, which allow for its observation. Hence, shear induced conformational changes and the interplay of conformation and binding properties could be investigated e.g. by FCS. Fig. 13.1(a) shows an autocorrelation curve of VWF labeled via antibodies. Upon application of shear forces, this curve should change revealing the influence of the conformational change on the dynamics of the protein. Binding experiments to endothelial cells or membranes as model systems either in form of vesicles or of supported lipid bilayers, as performed on FVIII in this work, combined with a flow chamber could help unravel the influence of shear on VWF binding to endothel and hence on its role in the establishment of the trombocyte network. Furthermore, FCS allows for the measurement of the binding of FVIII to VWF as well as to phospholipid membranes. A first binding isotherm of FVIII binding to VWF is shown in Fig. 13.1(b). A combination of microfluidics and binding experiments with FCS will reveal the influence of shear flow on the interaction of FVIII, VWF and phospholipid membranes. The results could then be used to reconstitute and study the kinetics of a small network consisting of VWF, FVIII, annexin and membrane surfaces. Knowledge about the influence of shear forces on the interaction of FVIII, VWF and membranes could also help to understand part of the initiation process of the coagulation cascade, since in this case activation of FVIII without thrombin is necessary, but so far, the only

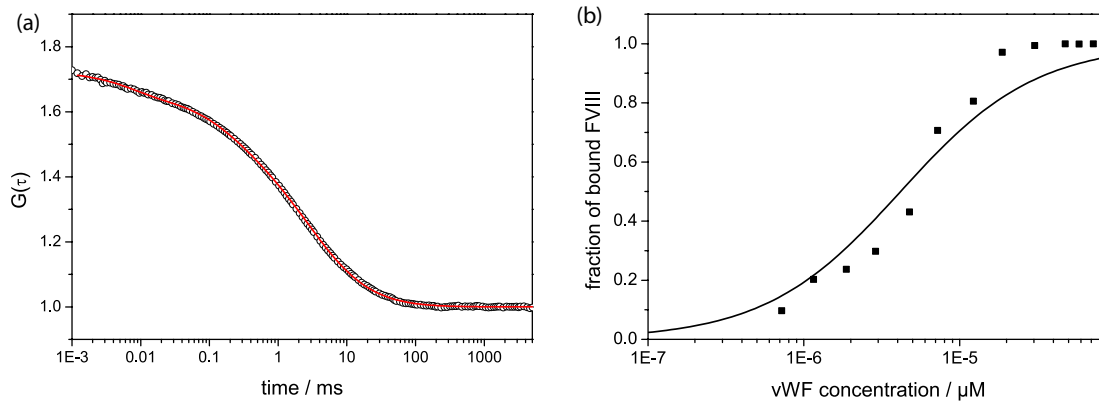


Figure 13.1: FCS experiments on VWF. (a) Autocorrelation curve (\circ) of VWF labeled via fluorescent antibodies and the corresponding fit (red line). (b) Titration curve of antibody labeled FVIII binding to unlabeled VWF. The full line represents a first approximation of a fit to the binding isotherm according to equation 5.18.

known activation mechanism of FVIII is thrombin-mediated. To conclude, FCS could help to address the specific questions how shear flow affects the shape of VWF and alters the biochemical rates of its interactions and thus contribute to a better understanding of hemostasis.

Bibliography

- [1] A W Burgess, H Cho, C Eigenbrot, K M Ferguson, T P J Garrett, D J Leahy, M A Lemmon, M X Sliwkowski, C W Ward, and S Yokoyama. An open-and-shut case? recent insights into the activation of egf/erbB receptors. *Mol Cell*, 12(3): 541–52, 2003.
- [2] CPM Reutelingsperger and WL Van Heerde. Annexin v, the regulator of phosphatidylserine-catalyzed inflammation and coagulation during apoptosis. *Cellular and Molecular Life Sciences (CMLS)*, 53(6):527–532, 1997.
- [3] E L Saenko, N M Ananyeva, E G D Tuddenham, and G Kemball-Cook. Factor viii - novel insights into form and function. *British journal of haematology*, 119(2):323–31, 2002.
- [4] S Mclaughlin and D Murray. Plasma membrane phosphoinositide organization by protein electrostatics. *Nature*, 438(7068):605–11, 2005.
- [5] U Golebiewska, A Gambhir, G Hangyás-Mihályné, I Zaitseva, J Rädler, and S Mclaughlin. Membrane-bound basic peptides sequester multivalent (pip₂), but not monovalent (ps), acidic lipids. *Biophys J*, 91(2):588–99, 2006.
- [6] G E Gilbert, B C Furie, and B Furie. Binding of human factor viii to phospholipid vesicles. *J Biol Chem*, 265(2):815–22, 1990.
- [7] L Rusu, A Gambhir, S McLaughlin, and J Rädler. Fluorescence correlation spectroscopy studies of peptide and protein binding to phospholipid vesicles. *Biophysical Journal*, 87(2):1044–1053, 2004.
- [8] P Schwille, J Bieschke, and F Oehlenschläger. Kinetic investigations by fluorescence correlation spectroscopy: the analytical and diagnostic potential of diffusion studies. *Biophysical chemistry*, 66(2-3):211–28, 1997.
- [9] P Schwille. Fluorescence correlation spectroscopy and its potential for intracellular applications. *Cell Biochem Biophys*, 34(3):383–408, 2001.
- [10] J Widengren and P Schwille. Characterization of photoinduced isomerization and back-isomerization of the cyanine dye cy5 by fluorescence correlation spectroscopy. *J. Phys. Chem. A*, 104(27):6416–6428, 2000.

- [11] J P Clamme, J Azoulay, and Y Mély. Monitoring of the formation and dissociation of polyethylenimine/dna complexes by two photon fluorescence correlation spectroscopy. *Biophys J*, 84(3):1960–8, 2003.
- [12] S T Hess, S Huang, A A Heikal, and W W Webb. Biological and chemical applications of fluorescence correlation spectroscopy: a review. *Biochemistry*, 41(3):697–705, 2002.
- [13] IT Dorn, KR Neumaier, and R Tampe. Molecular recognition of histidine-tagged molecules by metal-chelating lipids monitored by fluorescence energy transfer and correlation spectroscopys. *J. Am. Chem. Soc.*, 120(12):2753–2763, 1998.
- [14] E Rhoades, T F Ramlall, W W Webb, and D Eliezer. Quantification of alpha-synuclein binding to lipid vesicles using fluorescence correlation spectroscopy. *Biophysical Journal*, 90(12):4692–700, 2006.
- [15] D Grünwald, M C Cardoso, H Leonhardt, and V Buschmann. Diffusion and binding properties investigated by fluorescence correlation spectroscopy (fcs). *Curr Pharm Biotechnol*, 6(5):381–6, 2005.
- [16] E Van Craenenbroeck, G Matthys, J Beirlant, and Y Engelborghs. A statistical analysis of fluorescence correlation data. *Journal of Fluorescence*, 9(4):325–331, 1999.
- [17] ST Hess and W W Webb. Focal volume optics and experimental artifacts in confocal fluorescence correlation spectroscopy. *Biophys J*, 83(4):2300–17, 2002.
- [18] D Magde, E L Elson, and W W Webb. Fluorescence correlation spectroscopy. ii. an experimental realization. *Biopolymers*, 13:29–61, Oct 1974.
- [19] CT Culbertson, S C Jacobson, and J M Ramsey. Diffusion coefficient measurements in microfluidic devices. *Talanta*, 56(2):365–73, 2002.
- [20] Z Petrášek and P Schwillle. Precise measurement of diffusion coefficients using scanning fluorescence correlation spectroscopy. *Biophysical Journal*, 94(4):1437–1448, 2008.
- [21] C B Müller, A Loman, W Richtering, and J Enderlein. Dual-focus fluorescence correlation spectroscopy of colloidal solutions: influence of particle size. *J. Phys. Chem. B*, 112(28):8236–40, 2008.
- [22] J Enderlein, I Gregor, D Patra, and J Fitter. Art and artefacts of fluorescence correlation spectroscopy. *Curr Pharm Biotechnol*, 5(2):155–61, 2004.

-
- [23] J Enderlein, I Gregor, D Patra, T Dertinger, and U B Kaupp. Performance of fluorescence correlation spectroscopy for measuring diffusion and concentration. *ChemPhysChem*, 6(11):2324–36, 2005.
- [24] E Haustein and P Schwille. Single-molecule spectroscopic methods. *Current Opinion in Structural Biology*, 14(5):531–40, 2004.
- [25] K Bacia, S A Kim, and P Schwille. Fluorescence cross-correlation spectroscopy in living cells. *Nature methods*, 3(2):83–9, 2006.
- [26] K Bacia, SA Kim, and P Schwille. Fluorescence cross-correlation spectroscopy in living cells. *Nature methods*, 3(2):83, 2006.
- [27] R Philips, J Kondev, and J Theriot. *Physical biology of the cell*. Garland Science, 2009.
- [28] N Ben-Tal, B Honig, R M Peitzsch, G Denisov, and S McLaughlin. Binding of small basic peptides to membranes containing acidic lipids: theoretical models and experimental results. *Biophys J*, 71(2):561–75, 1996.
- [29] EL Saenko, D Scandella, AV Yakhyaev, and NJ Greco. Activation of factor viii by thrombin increases its affinity for binding to synthetic phospholipid membranes and activated platelets. *Journal of Biological Chemistry*, 273(43):27918, 1998.
- [30] J G Bieth. In vivo significance of kinetic constants of protein proteinase inhibitors. *Biochem Med*, 32(3):387–97, 1984.
- [31] S Stoilova-McPhie, B O Villoutreix, K Mertens, G Kembball-Cook, and A Holzenburg. 3-dimensional structure of membrane-bound coagulation factor viii: modeling of the factor viii heterodimer within a 3-dimensional density map derived by electron crystallography. *Blood*, 99(4):1215–23, 2002.
- [32] C Bardelle, B Furie, B C Furie, and G E Gilbert. Membrane binding kinetics of factor viii indicate a complex binding process. *J Biol Chem*, 268(12):8815–24, 1993.
- [33] J Israelachvili. *Intermolecular and Surface Forces*. Academic Press, 1991.
- [34] A D Douglass and R D Vale. Single-molecule microscopy reveals plasma membrane microdomains created by protein-protein networks that exclude or trap signaling molecules in t cells. *Cell*, 121:937–950, 2005.
- [35] K Hristova and D Needham. *in: Stealth Liosomes*. CRC Press, 1995.
- [36] Y O Posokhov, M V Rodnin, L Lu, and A S Ladokhin. Membrane insertion pathway of annexin b12: thermodynamic and kinetic characterization by fluorescence correlation spectroscopy and fluorescence quenching. *Biochemistry*.

- [37] P Wong, J Schauerte, K Wisser, H Ding, E Lee, D Steel, and A Gafni. Amyloid-beta membrane binding and permeabilization are distinct processes influenced separately by membrane charge and fluidity. *J. Mol. Biol.*, 386:81–96, 2009.
- [38] H Engelke, I Dorn, and JO Rädler. Diffusion and molecular binding in crowded vesicle solutions measured by fluorescence correlation spectroscopy. *Soft Matter*, 5(21):4283–4289, 2009.
- [39] RJ Ellis and AP Minton. Join the crowd. *Nature*, 425(6953):27–28, 2003.
- [40] RJ Ellis. Macromolecular crowding: an important but neglected aspect of the intracellular environment. *Current opinion in structural biology*, 11(1):114–119, 2001.
- [41] RJ Ellis. Macromolecular crowding: obvious but underappreciated. *Trends in Biochemical Sciences*, 26(10):597–604, 2001.
- [42] P Bernadóly, JG de la Torre, and M Pons. Macromolecular crowding in biological systems: hydrodynamics and nmr methods z. *J. Mol. Recognit*, 17:397–407, 2004.
- [43] JA Dix and AS Verkman. Crowding effects on diffusion in solutions and cells. *Annu. Rev. Biophys.*, 2008.
- [44] PM Haggie and AS Verkman. Diffusion of tricarboxylic acid cycle enzymes in the mitochondrial matrix in vivo. evidence for restricted mobility of a multienzyme complex. *Journal of Biological Chemistry*, 277(43):40782–40788, 2002.
- [45] H Zhou, G Rivas, and A P Minton. Macromolecular crowding and confinement: biochemical, biophysical, and potential physiological consequences. *Annual review of biophysics*, 37:375–97, 2008.
- [46] R Lenke and G Maret. *in: Scattering in Polymeric and Colloidal Systems*. Gordon and Breach Science Publishers, 2000.
- [47] G Maret. *in: Mesoscopic Quantum Physics*. Elsevier, 1995.
- [48] A Meller, R Bar-Ziv, T Tlusty, E Moses, J Stavans, and SA Safran. Localized dynamic light scattering: a new approach to dynamic measurements in optical microscopy. *Biophysical Journal*, 74(3):1541–1548, 1998.
- [49] A Einstein. Eine neue bestimmung der molekueldimensionen. *Annalen der Physik*, 19:289–306, 1906.
- [50] J Han and J Herzfeld. Macromolecular diffusion in crowded solutions. *Biophysical Journal*, 65(3):1155–1161, 1993.

-
- [51] N Muramatsu and AP Minton. Tracer diffusion of globular proteins in concentrated protein solutions. *Proceedings of the National Academy of Sciences*, 85(9):2984, 1988.
- [52] JD Dwyer and VA Bloomfield. Brownian dynamics simulations of probe and self-diffusion in concentrated protein and dna solutions. *Biophysical Journal*, 65(5):1810–1816, 1993.
- [53] E Dauty and AS Verkman. Molecular crowding reduces to a similar extent the diffusion of small solutes and macromolecules: measurement by fluorescence correlation spectroscopy. *Journal of Molecular Recognition*, 17(5):441–447, 2004.
- [54] J Szymański, A Patkowski, A Wilk, P Garstecki, and R Holyst. Diffusion and viscosity in a crowded environment: from nano- to macroscale. *J. Phys. Chem. B*, 110(51):25593–7, 2006.
- [55] W Doster and S Longeville. Microscopic diffusion and hydrodynamic interactions of hemoglobin in red blood cells. *Biophysical Journal*, 93(4):1360–1368, 2007.
- [56] CB Müller, T Eckert, A Loman, J Enderlein, and W Richtering. Dual-focus fluorescence correlation spectroscopy: a robust tool for studying molecular crowding. *Soft Matter*, 5(7):1358–1366, 2009.
- [57] A Celli, S Beretta, and E Gratton. Phase fluctuations on the micron-submicron scale in guvs composed of a binary lipid mixture. *Biophys J*, 94(1):104–16, 2008.
- [58] Z Petrásek and P Schwille. Precise measurement of diffusion coefficients using scanning fluorescence correlation spectroscopy. *Biophys J*, 94(4):1437–48, 2008.
- [59] C M Brown, R B Dalal, B Hebert, M A Digman, A R Horwitz, and E Gratton. Raster image correlation spectroscopy (rics) for measuring fast protein dynamics and concentrations with a commercial laser scanning confocal microscope. *Journal of Microscopy*, 229(Pt 1):78–91, 2008.
- [60] A Diaspro, G Chirico, and M Collini. Two-photon fluorescence excitation and related techniques in biological microscopy. *Quarterly Reviews of Biophysics*, 38(02):97–166, 2006.
- [61] E Dauty and AS Verkman. Actin cytoskeleton as the principal determinant of size-dependent dna mobility in cytoplasm: a new barrier for non-viral gene delivery. *Journal of Biological Chemistry*, 280(9):7823–7828, 2005.
- [62] B Dahlbäck. Blood coagulation. *Lancet*, 355(9215):1627–32, 2000.
- [63] P M Mannucci and E G Tuddenham. The hemophilias—from royal genes to gene therapy. *N Engl J Med*, 344(23):1773–9, 2001.

- [64] EL Saenko, NM Ananyeva, EG Tuddenham, and G Kemball-Cook. Factor viii-novel insights into form and function. *British journal of haematology*, 119(2):323, 2002.
- [65] EL Saenko, M Shima, and AG Sarafanov. Role of activation of the coagulation factor viii in interaction with vwf, phospholipid, and functioning within the factor xase complex. *Trends in cardiovascular medicine*, 9(7):185–192, 1999.
- [66] B D Griffin, L R Micklem, M C McCann, K James, and D S Pepper. The production and characterisation of a panel of ten murine monoclonal antibodies to human procoagulant factor viii. *Thromb Haemost*, 55(1):40–6, 1986.
- [67] D Murray, A Arbuzova, G Hangyás-Mihályné, A Gambhir, N Ben-Tal, B Honig, and S McLaughlin. Electrostatic properties of membranes containing acidic lipids and adsorbed basic peptides: theory and experiment. *Biophys J*, 77(6):3176–88, 1999.
- [68] S S Ahmad, J M Scandura, and P N Walsh. Structural and functional characterization of platelet receptor-mediated factor viii binding. *J Biol Chem*, 275(17):13071–81, 2000.
- [69] V Gerke, CE Creutz, and SE Moss. Annexins: linking ca²⁺ signalling to membrane dynamics. *Nature Reviews Molecular Cell Biology*, 6(6):449–461, 2005.
- [70] H O van Genderen, H Kenis, L Hofstra, J Narula, and CP M Reutelingsperger. Extracellular annexin a5: functions of phosphatidylserine-binding and two-dimensional crystallization. *Biochim Biophys Acta*, 1783(6):953–63, 2008.
- [71] JF Tait, DF Gibson, and C Smith. Measurement of the affinity and cooperativity of annexin v–membrane binding under conditions of low membrane occupancy. *Analytical biochemistry*, 329(1):112–119, 2004.
- [72] H A Andree, C P Reutelingsperger, R Hauptmann, H C Hemker, W T Hermens, and G M Willems. Binding of vascular anticoagulant alpha (vac alpha) to planar phospholipid bilayers. *J Biol Chem*, 265(9):4923–8, 1990.
- [73] WL Van Heerde and S Poort. Binding of recombinant annexin v to endothelial cells: effect of annexin v binding on endothelial-cell-mediated thrombin formation. *Biochemical Journal*, 302(Pt 1):305, 1994.
- [74] JH Rand, XX Wu, HAM Andree, JB Ross, E Rusinova, MG Gascon-Lema, C Calandri, and PC Harpel. Antiphospholipid antibodies accelerate plasma coagulation by inhibiting annexin-v binding to phospholipids: a” lupus procoagulant” phenomenon. *Blood*, 92(5):1652, 1998.

-
- [75] H A Andree, M C Stuart, W T Hermens, C P Reutelingsperger, H C Hemker, P M Frederik, and G M Willems. Clustering of lipid-bound annexin v may explain its anticoagulant effect. *J Biol Chem*, 267(25):17907–12, 1992.
- [76] A Jeskorka and O Orwar. Liposomes: Technologies and analytical applications. *Annu. Rev. Anal. Chem*, 1:801–832, 2008.
- [77] VP Torchilin, MI Papisov, AA Bogdanov, V S Trubetskoy, and VG Omelyanenko. *in: Stealth Liosomes*. CRC Press, 1995.
- [78] D Lasic and F Martin. *in: Stealth Liosomes*. CRC Press, 1995.
- [79] M Baru, L Carmel-Goren, Y Barenholz, I Dayan, S Ostropolets, I Slepoy, N Gvirtzer, V Fukson, and J Spira. Factor viii efficient and specific non-covalent binding to pegylated liposomes enables prolongation of its circulation time and haemostatic efficacy. *Thromb Haemost*, 93(6):1061–8, 2005.
- [80] C Allen, N Dos Santos, R Gallagher, G N C Chiu, Y Shu, W M Li, S A Johnstone, A S Janoff, L D Mayer, M S Webb, and M B Bally. Controlling the physical behavior and biological performance of liposome formulations through use of surface grafted poly(ethylene glycol). *Biosci Rep*, 22(2):225–50, 2002.
- [81] R P Richter, J L K Him, B Tessier, C Tessier, and A R Brisson. On the kinetics of adsorption and two-dimensional self-assembly of annexin a5 on supported lipid bilayers. *Biophys J*, 89(5):3372–85, 2005.
- [82] B G Trewyn, S Giri, I I Slowing, and V S-Y Lin. Mesoporous silica nanoparticle based controlled release, drug delivery, and biosensor systems. *Chem Commun (Camb)*, (31):3236–45, 2007.
- [83] V Cauda, A Schlossbauer, J Kecht, A Zürner, and T Bein. Multiple core-shell functionalized colloidal mesoporous silica nanoparticles. *J Am Chem Soc*, 131(32):11361–70, 2009.
- [84] A Schlossbauer, J Kecht, and T Bein. Biotin-avidin as a protease-responsive cap system for controlled guest release from colloidal mesoporous silica. *Angew Chem Int Ed Engl*, 48(17):3092–5, 2009.
- [85] C Lai, B G Trewyn, D M Jeftinija, K Jeftinija, S Xu, S Jeftinija, and V S-Y Lin. A mesoporous silica nanosphere-based carrier system with chemically removable cds nanoparticle caps for stimuli-responsive controlled release of neurotransmitters and drug molecules. *J Am Chem Soc*, 125(15):4451–9, 2003.
- [86] N K Mal, M Fujiwara, and Y Tanaka. Photocontrolled reversible release of guest molecules from coumarin-modified mesoporous silica. *Nature*, 421(6921):350–3, 2003.

- [87] J Liu, X Jiang, C Ashley, and C J Brinker. Electrostatically mediated liposome fusion and lipid exchange with a nanoparticle-supported bilayer for control of surface charge, drug containment, and delivery. *J Am Chem Soc*, 131(22):7567–9, 2009.
- [88] J Liu, A Stace-Naughton, X Jiang, and C J Brinker. Porous nanoparticle supported lipid bilayers (protocells) as delivery vehicles. *J Am Chem Soc*, 131(4):1354–5, 2009.
- [89] G Nordlund, J B S Ng, L Bergström, and P Brzezinski. A membrane-reconstituted multisubunit functional proton pump on mesoporous silica particles. *ACS nano*, 3(9):2639–46, 2009.
- [90] A Gabizon. Prolonged circulation time and enhanced accumulation in malignant exudates of doxorubicin encapsulated in polyethylene-glycol coated liposomes. *Cancer Res.*, 54:987–992, 1994.
- [91] T M Bayerl and M Bloom. Physical properties of single phospholipid bilayers adsorbed to micro glass beads. a new vesicular model system studied by 2h-nuclear magnetic resonance. *Biophys J*, 58(2):357–62, 1990.
- [92] C-S Chen, J Yao, and R A Durst. Liposome encapsulation of fluorescent nanoparticles: Quantum dots and silica nanoparticles. *Journal of Nanoparticle Research*, 2006(8):1033–1038, 2006.
- [93] J Kecht, A Schlossbauer, and T Bein. Selective functionalization of the outer and inner surfaces in mesoporous silica nanoparticles. *Chem. Mater.*, 20:7207–7214, 2008.
- [94] I Gradus-Pizlo, R L Wilensky, K L March, N Fineberg, M Michaels, G E Sandusky, and D R Hathaway. Local delivery of biodegradable microparticles containing colchicine or a colchicine analogue: effects on restenosis and implications for catheter-based drug delivery. *J Am Coll Cardiol*, 26(6):1549–57, 1995.
- [95] U Rothbauer, K Zolghadr, S Tillib, D Nowak, L Schermelleh, A Gahle, N Backmann, K Conrath, S Muyldermans, M C Cardoso, and H Leonhardt. Targeting and tracing antigens in live cells with fluorescent nanobodies. *Nature Methods*, 3: 887–889, 2006.
- [96] F Höfling, T Munk, E Frey, and T Franosch. Critical dynamics of ballistic and brownian particles in a heterogeneous environment. *The Journal of Chemical Physics*, 128(16):164517, 2008.
- [97] F Höfling, T Franosch, and E Frey. Localization transition of the three-dimensional lorentz model and continuum percolation. *Physical review letters*, 96(16):165901, 2006.

-
- [98] Y Tseng, T P Kole, and D Wirtz. Micromechanical mapping of live cells by multiple-particle-tracking microrheology. *Biophys J*, 83(6):3162–76, 2002.
- [99] W Feneberg, M Westphal, and E Sackmann. Dictyostelium cells’ cytoplasm as an active viscoplastic body. *Eur Biophys J*, 30(4):284–94, 2001.
- [100] P Sekhar Burada, P Hänggi, F Marchesoni, G Schmid, and P Talkner. Diffusion in confined geometries. *ChemPhysChem*, 10(1):45–54, 2009.
- [101] H Karcher, J Lammerding, H Huang, R T Lee, R D Kamm, and M R Kaazempur-Mofrad. A three-dimensional viscoelastic model for cell deformation with experimental verification. *Biophysical Journal*, 85:3336–3349, 2003.
- [102] D Arcizet, B Meier, E Sackmann, J O Rädler, and D Heinrich. Temporal analysis of active and passive transport in living cells. *Physical review letters*, 101(24):248103, 2008.
- [103] O D Weiner, W A Marganski, L F Wu, S J Altschuler, and M W Kirschner. An actin-based wave generator organizes cell motility. *PLoS Biol*, 5(9):e221, 2007.
- [104] R G Winkler, S Keller, and J O Rädler. Intramolecular dynamics of linear macromolecules by fluorescence correlation spectroscopy. *Phys Rev E Stat Nonlin Soft Matter Phys*, 73(4 Pt 1):041919, 2006.
- [105] Ruchira, M A Hink, L Bosgraaf, P J M van Haastert, and ntonie J W G Visser. Pleckstrin homology domain diffusion in dictyostelium cytoplasm studied using fluorescence correlation spectroscopy. *J Biol Chem*, 279(11):10013–9, 2004.
- [106] E O Potma, W P de Boeij, L Bosgraaf, J Roelofs, P J van Haastert, and D A Wiersma. Reduced protein diffusion rate by cytoskeleton in vegetative and polarized dictyostelium cells. *Biophys J*, 81(4):2010–9, 2001.
- [107] F Lanni and B R Ware. Detection and characterization of actin monomers, oligomers, and filaments in solution by measurement of fluorescence photobleaching recovery. *Biophys J*, 46(1):97–110, 1984.
- [108] C F Schmidt, M Bärmann, G Isenberg, and E Sackmann. Chain dynamics, mesh size, and diffusive transport in networks of polymerized actin. a quasielastic light scattering and microfluorescence study. *Macromolecules*, 22(9):3638–3649, 2001.
- [109] S S Rogers, T A Waigh, and J R Lu. Intracellular microrheology of motile amoeba proteus. *Biophys J*, 94(8):3313–22, 2008.
- [110] G Gerisch, T Bretschneider, A Müller-Taubenberger, E Simmeth, M Ecke, S Diez, and K Anderson. Mobile actin clusters and traveling waves in cells recovering from actin depolymerization. *Biophys J*, 87(5):3493–503, 2004.

- [111] T Bretschneider, K Anderson, M Ecke, A Müller-Taubenberger, B Schroth-Diez, H C Ishikawa-Ankerhold, and G Gerisch. The three-dimensional dynamics of actin waves, a model of cytoskeletal self-organization. *Biophys J*, 96(7):2888–900, 2009.
- [112] A Diaspro, G Chirico, and M Collini. Two-photon fluorescence excitation and related techniques in biological microscopy. *Quarterly Reviews of Biophysics*, 38(2):97–166, 2005.
- [113] P Schwille, U Haupts, S Maiti, and W W Webb. Molecular dynamics in living cells observed by fluorescence correlation spectroscopy with one- and two-photon excitation. *Biophys J*, 77(4):2251–65, 1999.
- [114] J Clamme, G Krishnamoorthy, and Y Mély. Intracellular dynamics of the gene delivery vehicle polyethylenimine during transfection: investigation by two-photon fluorescence correlation spectroscopy. *Biochim Biophys Acta*, 1617(1-2):52–61, 2003.
- [115] J Mütze, Z Petrášek, and P Schwille. Independence of maximum single molecule fluorescence count rate on the temporal and spectral laser pulse width in two-photon fcs. *Journal of Fluorescence*, 17(6):805–10, 2007.
- [116] E Spiess, F Bestvater, A Heckel-Pompey, K Toth, M Hacker, G Stobrawa, T Feurer, C Wotzlaw, U Berchner-Pfannschmidt, T Porwol, and H Acker. Two-photon excitation and emission spectra of the green fluorescent protein variants ecfp, egfp and eyfp. *Journal of Microscopy*, 217(Pt 3):200–4, 2005.
- [117] A A Rehms and P R Callis. Two-photon fluorescence excitation spectra of aromatic amino acids. *Chemical Physics Letters*, 208:276–282, 1993.
- [118] J Humpolicková, E Gielen, A Benda, V Fagulova, J Vercammen, M Vandeven, M Hof, M Ameloot, and Y Engelborghs. Probing diffusion laws within cellular membranes by z-scan fluorescence correlation spectroscopy. *Biophys J*, 91(3):L23–5, 2006.
- [119] P Schwille, J Korlach, and W W Webb. Fluorescence correlation spectroscopy with single-molecule sensitivity on cell and model membranes. *Cytometry*, 36(3):176–82, 1999.
- [120] X Schlagberger, J Bayer, JO Rädler, and RR Netz. Diffusion of a single semiflexible charged polymer. *EPL (Europhysics Letters)*, 76:346–352, 2006.
- [121] V Kahl, M Hennig, B Maier, and J O Rädler. Conformational dynamics of dna-electrophoresis on cationic membranes. *Electrophoresis*, 30(8):1276–81, 2009.
- [122] J Han and H G Craighead. Separation of long dna molecules in a microfabricated entropic trap array. *Science*, 288(5468):1026–9, 2000.

- [123] W Volkmuth, T Duke, M Wu, R Austin, and A Szabo. Dna electrodiffusion in a 2d array of posts. *Physical review letters*, 72(13):2117–2120, 1994.
- [124] S W Schneider, S Nuschele, A Wixforth, C Gorzelanny, A Alexander-Katz, R R Netz, and M F Schneider. Shear-induced unfolding triggers adhesion of von willebrand factor fibers. *Proc Natl Acad Sci USA*, 104(19):7899–903, 2007.

14 Danksagung

An dieser Stelle möchte ich mich bei allen, die mich während der Entstehung dieser Arbeit und darüberhinaus unterstützt haben, ganz herzlich bedanken.

Zuerst danke ich ganz besonders meinem Doktorvater, Prof. Dr. Joachim Rädler. Er hat mir diese spannende Arbeit ermöglicht und mich dabei auf seine sehr herzliche Art und Weise unterstützt und gefördert. Auch für die sehr guten Arbeitsbedingungen, die unvergleichlich angenehme Atmosphäre und die Freiheit, selbständig zu arbeiten bedanke ich mich ganz herzlich.

Prof. Dr. Roland Netz, meinem IDK-Mentor, danke ich für seine Unterstützung und interessante Diskussionen und Anregungen zu den verschiedensten Projekten.

Dr. Ingmar Dorn, der uns auf den Faktor VIII gebracht hat und somit mein Interesse an Blutgerinnung geweckt und zum Hauptprojekt dieser Arbeit angeregt hat, gilt mein Dank.

Bei Valentina Cauda, Delphine Arcizet und Anna Sauer bedanke ich mich sehr für die einzigartige Zusammenarbeit bei unserem Liposomen-Nanopartikel-Projekt und für alle damit einhergehenden und darüberhinausgehenden Diskussionen, sei es beim Wandern, gemeinsamen Abendessen oder anderen Gelegenheiten. Mille grazie! Merci beaucoup! Vielen Dank!

Allen Rädlers danke ich für die äusserst angenehme Atmosphäre, die Vielzahl an gemeinsamen Aktivitäten, von Grillabenden bis hin zur Winterschule, und die unvergleichlich schöne Zeit. Susanne Kempter, Gerlinde Schwake und Susanne Rappl gilt mein Dank für ihre Hilfe im Labor. Margarete Meixner möchte ich für ihr Engagement beim Organisieren und Koordinieren danken. Danke an meine Bürokollegen für eine jahrelange gute Zimmergemeinschaft und an Martin Hennig für die Zusammenarbeit beim DNA-Projekt. Danke auch besonders an Judith Megerle und Madeleine Leisner, die mich hier eingeführt und die ganze Zeit in freundschaftlicher Verbundenheit begleitet haben.

Bei allen Korrekturlesern bedanke ich mich für unermüdliches Lesen und hilfreiche Anregungen und Tipps.

Allen Mitarbeitern von IDK und CeNS möchte ich danken für die vielseitigen, interdisziplinären Angebote; insbesondere auch der Band "unCeNSiert" für die vielen lustigen Proben und Auftritte. Keep Swinging!

Danke an alle meine Freunde, die für die nötige Abwechslung und guten Ausgleich gesorgt haben.

Schliesslich möchte ich mich noch ganz herzlich bei Elias, meinen Eltern und meiner Schwester bedanken, die mich immer und in jeder Hinsicht sehr unterstützt haben.

Vielen Dank!

15 Lebenslauf

Persönliche Daten

Hanna Christina Engelke

Spixstr. 18

81539 München

Geboren am 24.03.1981 in Würzburg

Familienstand: ledig

Ausbildung

1991 - 2000	Riemenschneider Gymnasium Würzburg, Abschluss mit dem Abitur
2000 - 2005	Studium der Physik an der Universität Bayreuth, Abschluss mit dem Diplom
2002 - 2003	Studium der Physik an der Exeter University, UK, im Rahmen eines Erasmusstipendiums
2004 - 2005	Diplomarbeit zum Thema "Optische Spektroskopie an einzelnen Perylenbisimiden" bei Prof. Dr. J. Köhler an der Universität Bayreuth
2006	wissenschaftlicher Mitarbeiter in der Gruppe von Prof. Dr. J. Köhler, Universität Bayreuth
seit 2006	wissenschaftlicher Mitarbeiter in der Gruppe von Prof. Dr. J. O. Rädler, LMU München
seit 2008	Mitglied des Internationalen Doktoranden Kollegs Nano-Bio-Technology

Publikationen

- E. Lang, R. Hildner, H. Engelke, P. Osswald, F. Würthner und J. Köhler, (2007), "Comparison of the Photophysical Parameters for Three Perylene Bisimide Derivatives by Single-Molecule Spectroscopy", *ChemPhysChem*, 8, 1487 - 1496
- H. Engelke, I. Dorn und J. O. Rädler, (2009), "Diffusion and molecular binding in crowded vesicle solutions measured by fluorescence correlation spectroscopy", *Soft Matter*, 5, 4283 - 4289
- V. Cauda, H. Engelke, A. Sauer, D. Arzicet, C. Bräuchle, J. Rädler und T. Bein, "Colchicine-loaded lipid bilayer-coated 50 nm mesoporous nanoparticles efficiently induce microtubule depolymerization upon cell uptake" submitted to *Nature Nanotechnology*
- H. Engelke, I. Dorn und J. O. Rädler, "Anomalous charge sensitivity of activated FVIII binding to PS-membranes enhances regulation efficiency by Annexin V", submitted to *PNAS*